論文 / 著書情報
Article / Book Information

題目(和文)	
Title(English)	The formation and late accretion of Mars
著者(和文)	WOOMan Yin
Author(English)	Man Yin Woo
出典(和文)	学位:博士(理学), 学位授与機関:東京工業大学, 報告番号:甲第11247号, 授与年月日:2019年9月20日, 学位の種別:課程博士, 審査員:井田 茂,中本 泰史,玄田 英典,奥住 聡,HERNLUND JOHN WILLIA
Citation(English)	Degree:Doctor (Science), Conferring organization: Tokyo Institute of Technology, Report number:甲第11247号, Conferred date:2019/9/20, Degree Type:Course doctor, Examiner:,,,,
学位種別(和文)	博士論文
Type(English)	Doctoral Thesis

THE FORMATION AND LATE ACCRETION OF MARS

A THESIS

SUBMITTED TO THE DEPARTMENT OF EARTH AND PLANETARY SCIENCES

OF TOKYO INSTITUTE OF TECHNOLOGY

By

Woo Man Yin

August 2019

Abstract of thesis entitled

THE FORMATION AND LATE ACCRETION OF MARS

submitted by

Woo Man Yin

at Tokyo Institute of Technology

in August 2019

Mars is one of the most well studied objects in the Solar System. Yet, its formation and early evolution is still unclear. In our studies, we explore the early history of our red neighbour by numerical simulations and combining it with cosmochemical data.

Recent isotopic studies of the martian meteorites suggests that the bulk composition of Mars is significantly different from Earth, with Mars being composed of a higher fraction of ordinary chondrite-like material. Here, we evaluate this compositional difference in more detail by comparing output from two N-body planet formation models: the "Classical" case wherein Jupiter and Saturn are kept in their current orbits, and the "Grand Tack" case in which Jupiter and Saturn migrate through the primordial asteroid belt. Our results show that

both models tend to yield Earth and Mars analogues whose accretion zones overlap. Assuming a disc with a composition change (break) at 1.3 AU reproduces the isotopic differences between Earth and Mars in both models. At this break location, the Classical case fares better in forming Mars with its documented composition (29% to 68% enstatite chondrite plus 32% to 67% ordinary chondrite) though the Mars analogues are generally too massive. However, if a restriction of mass on the Mars analogues is included such as requiring that its mass only differ from its current value by at most 50%, the Classical model does not work better. Both models are unlikely to work with a completely mixed disk since the probability of forming Earth with $> 70\%$ of enstatite chondrite is lower than 5%. We further calculate the isotopic composition of ^{17}O, ^{50}Ti, ^{54}Cr, ^{142}Nd, ^{64}Ni, and ^{92}Mo in the martian mantle from the Grand Tack simulations. We find that it is possible to match the calculated isotopic composition of all the above elements in Mars' mantle with their measured values, but the resulting uncertainties are too large to place good restrictions on the early dynamical evolution and birth place of Mars. These large uncertainties are caused by both the chaotic evolution of the forming planets and the large uncertainties in the measured isotopic deviations of some elements in martian samples.

The final stage of Mars' accretion is crucial to its early surface evolution. The abundance of highly siderophile elements in the martian mantle obtained from the martian meteorites implies a chondritic mass addition of $\sim$0.8 wt% after the core formation of Mars (dubbed "Late Veneer" (LV)) . Late accretion to Mars by a differentiated Ceres-sized ($\sim$1000 km diameter) object at 4480 Ma can account for part of the requisite LV mass. We analyse the outcome of the hypothetical LV giant impact to Mars with smoothed particle hydrodynamics simulations together with analytical theory. Results show that, in general, about 50% of

the impactor's metallic core shatters into ∼10 m fragments that subsequently fragment into sub-mm metallic hail at re-accretion. This returns a promising delivery of HSEs into the martian mantle compared to either a head-on and hit-and-run collision; in both cases, less than 10% of the impactor's core materials are fragmented and finally embedded in the martian mantle. The millimetre-sized metal hail could thus react with a postulated martian hydrosphere to generate ∼3 bar of H_2, which is adequate to act as a greenhouse and keep early Mars warm, in addition to providing a reducing environment for pre-biotic chemistry. Yet, this H_2 envelope typically survives less than 3 Myr due to the expected extreme ultraviolet (EUV) flux of the early Sun. If the Sun was a slow rotator an accordingly weaker EUV flux could extend this lifetime to more than 10 Myr, but is difficult to reach 20 Myr. This is much shorter than the one formed after the LV giant impact on Earth (> 100 Myr), which suggests that Mars probably did not have a long-living post-impact biosphere after the giant impact. This early escape of the impact-generated H_2 envelope could possibly explain the early mass fractionation of xenon on Mars. A dense pre-Noachian CO_2 atmosphere should lower the escape efficiency of hydrogen by IR emission. A more detailed hydrodynamic atmospheric model of this early H_2 atmosphere is warranted to examine its effect on pre-Noachian Mars.

Our studies demonstrate a new and revolutionary approach to studying the formation and evolution of the early Solar System: combining dynamics and cosmochemical data. Interdisciplinary study is the key to solving the mysteries of the early evolution of the Solar System and hence the origin of life.

Acknowledgements

I would like to take this chance to thank all the people that supported me in my PhD study.

The first person I would like to thank is Prof. Ramon Brasser from ELSI. He is my main collaborator, who guided me most during my PhD. It is my pleasure to work with him in these three years. I learn a lot from him, including planetary dynamical and cosmochemical knowledge, how to write computer scripts to effectively analyse data, the method of starting a new project and collaborating with people from another research fields, etc. Every time when I get into trouble, he gives me useful advice on solving problems, including those which are not related to my PhD research. Also, he often actively shares what he learned from other researcher and asks whether I need help. He is one of the kindest people that I have met. Without him, I could not finish writing this thesis and to continue my research career. Once again, I appreciate all his help.

I would also like to thank my academic supervisor Prof. Shigeru Ida from ELSI and Tokyo Tech. He admitted me into the Graduate School of Tokyo Tech. He and Prof. Brasser both strived for financial support of my PhD study in Japan. Prof. Ida also solved my administrative problem when I first entered Tokyo Tech. Besides, he always answers my questions related to planet formation and provides feed back during my presentation. He is a gentlemen

which makes me feel relax when chatting with him. It is my pleasure to be his student.

I would like to thank my other collaborators for assisting my PhD research. Prof. Hidenori Genda from ELSI provides me SPH simulation data and assisted my second project. He is a funny person whom I enjoy talking with. Prof. Stephen Mojzsis from UC Boulder assisted both of my projects by giving opinion on cosmochemical related topics. He also taught me how to prepare an job interview, which is crucial for me to continue my research career. Dr. Soko Matsumura from U Dundee provided me simulation data for my first study. All collaborators help proofreading my published papers. I am glad that I have the chance to work with all these excellent researchers and hope that we can continue our collaboration in the future.

Finally, I thank the Earth-Life Science Institute and the Japan Society for the Promotion of Science (Research Fellowship for Young Scientists DC2) for supporting my PhD study.

Contents

Chapter 1

Introduction

Mars, one of our closest neighbour in the universe, has had our attention since the beginning of human civilization. Our understanding of this red planet has deepened during the second half of the 20^{th} century, when orbiters and landers were frequently launched to study the atmosphere and surface of Mars. Apart from data gathered from space missions, meteorites from Mars that occasionally fall on Earth (e.g. Fig. 1.1) provide additional clues about the early history and evolution of not only the planet itself, but also the entire inner Solar System. Cosmochemical analysis (e.g. isotopic anomalies and radiometric dating) of the martian meteorites and other meteorites are being made with more powerful analytical tools that yield data with unprecedented precision and accuracy. These measurements help to constrain both the absolute and relative chronology of planet formation that is subsequently fed into modern dynamical models of accretion via increasingly sophisticated numerical simulations (e.g Morbidelli et al. 2012).

Geochemical and isotopic analysis of the martian meteorites allows us to narrow the uncertainties of the timing of Mars' formation. For example, Dauphas

Figure 1.1: Example of a martian meteorite, EETA 79001, which is classified as shergottite and is igneous rock of volcanic or plutonic origin. Martian meteorites that originated from the surface or interior of Mars provide clues about the formation and evolution of the planet and hence the early Solar System. Image credit: NASA.

& Pourmand (2011) analysed a suite of martian meteorites to argue that Mars reached about half of its current size in approximately 1.8 Myr. Mars likely finished its accretion within ∼10 Myr of the start of the Solar System. It is straight forward to think that Earth requires more time to form because of its much larger mass. Indeed, derivation of timescales for terrestrial accretion from the Hf-W chronometer supports this idea by showing that Earth finished its core formation at least 30 Myr after the Calcium-aluminium-rich inclusion (CAI) formation (e.g. Kleine et al. (2009) and references therein). These observations can be summarised as a general time line for the formation of the terrestrial planets, and combining such cosmochemical constraints with dynamical models helps efforts to unravel the mystery of the formation of the sampled terrestrial planets and, by extension, that of the whole inner Solar System.

1.1 Dynamical models of terrestrial planet formation

According to traditional dynamical models of the late stage of planet formation, coagulation of planetesimals (km-sized objects) into planetary embryos (thousands km-sized bodies) and subsequent giant impacts between embryos gave rise to the terrestrial planets. Several different models have been proposed for this scenario. This thesis focuses on two of them – the Classical and the Grand Tack model.

1.1.1 The Classical model

This is the fundamental model of planet formation, in which all the terrestrial planets formed near their current locations. Chambers (2001) performed simulations with different masses of planetesimals and embryos with the surface density profile of a "minimum mass" solar nebula (Weidenschilling 1977) to study the growth of terrestrial planets. Jupiter and Saturn are placed on their current orbits (EJS model). Simulations showed that it is typical to produce three to five terrestrial planets with orbital seperation and mass concentration to the largest body similar to the current system. A recurring problem with the simulations, however, is that the masses of computed planets which form close to 1.5 AU are consistently greater than the current mass of Mars (the "Massive Mars problem"). This was recapitulated in simulations by Raymond et al. (2009), especially when both Jupiter and Saturn were placed on circular orbits (CJS model). To avoid forming a massive Mars, an alternative solution was proposed by Agnor et al. (1999) and expanded upon by Hansen (2009): this work initially confined all solid material to the area in between the current

locations of Venus and Earth at 0.7 AU and 1 AU in an annulus model. With this setting, Hansen (2009) successfully reproduced the mass-distance relation of the terrestrial planets, with two massive planets and in the centre and two smaller ones at the inner and outer edge. If all the material making up the terrestrial planets was confined within a small annulus, what is the underlying mechanism that leads to this configuration? The *Grand Tack* model proposed by Walsh et al. (2011) provides a reasonable explanation.

1.1.2 The Grand Tack model

In this model, Jupiter first formed near its current location and opened a gap in the gas disc. Owing to the unbalanced tidal torque acting on the planet, Jupiter migrated inwards through type-II migration (e.g Lin & Papaloizou 1986). At the time Jupiter was migrating, Saturn formed further away and slowly accreted its gaseous envelope. Saturn then began migrating inwards, caught up with Jupiter, and the two gas giants were trapped in the 2:3 mean motion resonance (Masset & Snellgrove 2001). With this specific orbital spacing and mass ratio between the two gas giants, the total torque on both planets reversed and therefore the migration direction also reversed, being outward from the Sun. The tack location, where Jupiter reversed its direction of migration, is set to be 1.5 AU in order to confine the growth of Mars (Walsh et al. 2011). This mechanism provides a plausible explaination on how the migration of Jupiter reshaped the structure of the inner solid disc. Two possible scenarios emerge from this model: either Jupiter scattered away the planetesimals and embryos in its path, or pushed them into the inner region by trapping them in mean motion resonance. In either case, when Jupiter reversed its migration, the region in between 1 and 1.5 AU was cleared. On the other hand, solid material piled up within 1 AU,

thus duplicating the outer edge configuration suggested by the annulus model. Therefore, the mass-distance relation of the terrestrial planets and the low mass of Mars are explicable by the Grand Tack model.

Another possible mechanism creating an annulus near the current orbits of the terrestrial planets is proposed by Drażkowska et al. (2016). In this model, pebbles pile up in a radial distribution due to a combination of growth and radial drift of dust, and therefore a narrow annulus of planetesimals close to 1 AU can be formed through the streaming instability (Johansen et al. 2007; Ida & Guillot 2016). This model implies that all the terrestrial planets form from the similar building blocks and therefore that their bulk and isotopic compositions are likely to be similar to each other. However, the isotopic compositions of the planets suggest that this may not be the case (see Sect. 1.3).

1.2 Other constraints on N-body planet formation models

1.2.1 Elemental abundances

In the past decade, other planet formation models have been developed to explain the current dynamical features of the inner solar system (e.g. Izidoro et al. 2014; Clement et al. 2018). These features include a small Mars ($\sim$0.1 $M_{\oplus}$), a low-mass asteroid belt ($\sim 5 \times 10^{-4}$ $M_{\oplus}$) and the distribution of S-type and C-type asteroids in the asteroid belt, etc. Therefore, considering only the dynamical properties cannot solve the problem of planet formation. We need more evidences to measure the degree of success of a planet formation model.

One way of further constraining planet formation models is to study the bulk

composition of planets through tracing the original locations of the planetesimals that accreted into each planet. Chambers (2001) first applied this method to compute the bulk composition of each planet in the Classical model and found that smaller planets (Mercury and Mars analogues) compose materials mostly originated close to their final locations, whereas larger planets (Venus and Earth analogues) contain material throughout different regions of the disc. Later, Raymond et al. (2004) assumed a heliocentric gradient of water content in the initial solid disc to compute the bulk water content in each planet formed in the Classical model. Their results show that the final bulk water content of the terrestrial planets increases when the assumed planetesimal masses are higher or Jupiter is in a circular orbit. O'Brien et al. (2006) extended this type of volatile delivery study by putting in a higher number of planetesimals than Raymond et al. (2004). They found that the Classical CJS model deliver a higher amount of volatiles from the outer asteroid belt region than the Classical EJS model, which agrees with the results of Raymond et al. (2004).

In the past decade, other studies were conducted to examine whether the current dynamical model could reproduce the *elemental abundances* of both refractory and volatile elements of the terrestrial planets. Instead of assuming a radial composition gradient, Bond et al. (2010) computed the bulk elemental abundances of the terrestrial planets by combining the HSC chemical models (White et al. 1958) with N-body simulations of the Classical model performed by O'Brien et al. (2006). The HSC chemical model can estimate the initial composition of the building blocks of planets according to the elements' condensation sequence. Their results show good agreement between the measured values and calculated values, except for volatiles such as nitrogen (N) and carbon (C). This study is then further extended by Elser et al. (2012), in which

they computed the elemental abundances of the planets with three different disc models and more sets of the Classical N-body simulations from Morishima et al. (2010). By picking a more realistic time of transition from the gas disc model to the N-body model, their results fail to explain the volatile composition (e.g. sodium (Na), sulphur (S)) of all planets and the refractory composition of Mercury. Considering that planetesimals condense out sequentially from the gas disc, this does not help to solve the volatile excess problem (Moriarty et al. 2014). Matsumura et al. (2016) performed a similar study, also including the Grand Tack model. They found that the Grand Tack model works similarly to the Classical model in explaining the refractory and moderately volatile elements (e.g chromium (Cr)), but the former is more efficient in delivering volatile elements to the terrestrial planets because of the stronger scattering and radial mixing caused by the migrating giant planets.

The utilisation of water content and elemental abundances in constraining a planet formation model and planets' building blocks, however, imposes uncertainties because the elemental abundances of a planet traced from its crustal or mantle samples could be altered by planet formation processes; for example, an impact causing lost of volatiles in the atmosphere (Genda & Abe 2005) and core formation and differentiation leading to siderophile and chalcophile elements' partition into the core (Badro et al. 2015). Even though there are studies combining N-body simulations with the core-mantle differentiation model (Rubie et al. 2015), their computed planets' composition would be highly dependent on the adopted differentiation model, which is a function of pressure, temperature and oxygen fugacity. Besides, the HSC chemical model adopted by the above studies are based on the assumption of equilibrium condensation of the

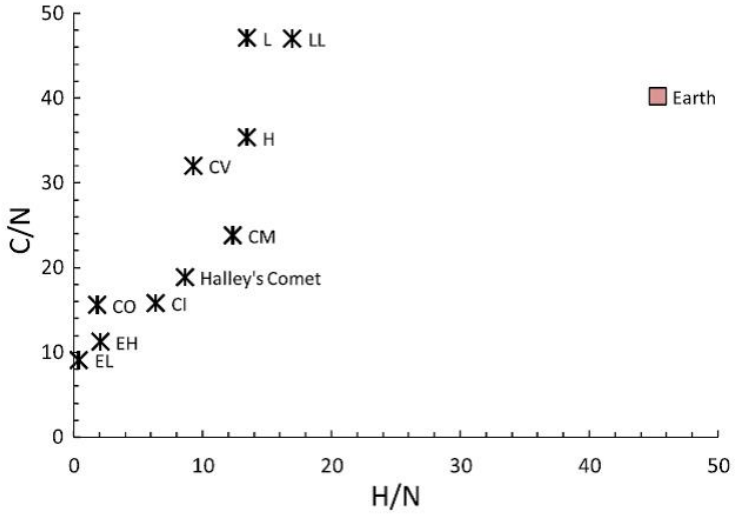

Figure 1.2: Weight ratios of H, C and N in different classes of chondrites compared with the composition of the bulk silicate Earth. EL and EH are enstatite chondrites; LL, L and H are ordinary chondrites and CO, CI, CM and CV are carbonaceous chonrite. No combination of different chondrites or comets yields the composition of Earth's major volatiles. Taken from Halliday (2013).

gas. Elser et al. (2012) pointed out that this assumption is crucial in determining the final bulk composition of planets. In this HSC chemical model, the composition of the building blocks of terrestrial planets are only determined by the condensation sequence of elements. In fact, the composition of the initial gas disc would also be altered by transient heating, transport of chemical species and the grains inherited from the molecular cloud core (Matsumura et al. 2016). All of these effects could possibly change the results of the above studies, and therefore cause difficulties in adopting the elemental abundance data as constraints on planet formation models and the building blocks of planets. The current data of C/N and H/N ratios of different chondrites (Fig. 1.2) shows that the Earth's elemental abundances could not be reproduced by mixing different chondritic reservoirs (Halliday 2013). This is proof that the elemental abundances of volatiles on Earth cannot be utilised to trace its building blocks, whose identities could be preserved in the current meteoritic data.

1.2.2 Isotopic composition

Because of the complexity of utilising elemental abundances, the cosmochemical community switched to another type of data when tracing the building blocks of planets – the *isotopic* data. The isotopic composition of a sample is measured as the deviation of a less abundant isotope to the most abundant isotope of an element. For instance, the deviations from Earth in the abundance of the 54 isotope of chromium (^{54}Cr) is expressed as

$$\varepsilon^{54}\mathrm{Cr} = \left\{ \frac{(^{54}\mathrm{Cr}/^{52}\mathrm{Cr})_{\mathrm{sample}}}{(^{54}\mathrm{Cr}/^{52}\mathrm{Cr})_{\mathrm{Earth}}} - 1 \right\} \times 10000 \tag{1.1}$$

where ε represents parts per ten thousands and ^{54}Cr/^{52}Cr is the ratio of ^{54}Cr to the most abundant isotope of chromium ^{52}Cr in the meteorite sample or the terrestrial sample, respectively.

The major advantage to adopt (nucleosynthetic) isotopic data for constraining planet formation models and building blocks is that the isotopic compositions of elements with non mass-dependent nucleosynthetic variations are not affected by planetary internal physical-chemical processes such as core-mantle partition and differentiation (Carlson et al. 2018). Different isotopes of an element react similarly to these processes. For instance, all isotopes of Ruthenium (Ru, a highly siderophile element) would sink to the core in a similar extent during core formation and therefore the ratio between the light and heavy Ru isotopes in the mantle remains more or less constant throughout the whole core formation process, whereas the ratio between Ru and other elements, such as Molybdenum, (Mo), would change because Ru and Mo have different siderophile natures (Mo is moderately siderophile, but Ru is highly siderophile). We would like to emphasise that both *element abundances* and the *isotopic* composition of

a planet are important in understanding planet formation processes. Only when we consider constraining N-body planetary models and planets' building blocks, isotopic data have a major advantage with its high resistance to planet's internal processes. Therefore, we focus on discussing isotopic composition of planets and bulk meteorites in this thesis. The incoporation of elemental abundances is reserved for future work.

The difficulty in obtaining the isotopic composition of planetary objects, however, is that it has to be measured directly from the samples. It cannot be predicted or computed from the chemical condensation model that the above studies adopted or from any other protoplanetary disc model. Hence, we have to currently make use of meteorites that fall to Earth to study the initial composition of the solid disc. Among all the meteorites, the most abundant type are *chondrites*. They are primitive remnant solids of planet formation that did not experienced high-pressure melting and parent body differentiation. Because of their large number of samples and primitiveness, the isotopic composition of chondrite has been well studied. These isotopes include, for example, the most abundant element oxygen (O), and less abundant element calcium (Ca), titanium (Ti), chromium (Cr), nickel (Ni), molybdenum (Mo) and ruthenium (Ru) (Carlson et al. 2018 and references therein). Chondrites are classified mainly into three classes based on their water content, oxidation state and isotopic composition – enstatite chondrite, ordinary chondrite and carbonaceous chondrite. Fig. 1.3 shows a possible initial heliocentric distribution of these three chondritic classes, with the most reduced and driest enstatite chondrite in the inner most region, moderately oxidised and volatile-rich ordinary chondrite located further than 1.5 AU, and the most oxidised and volatile-richest carbonaceous chondrite originating from the giant planet region. Other studies (Morbidelli

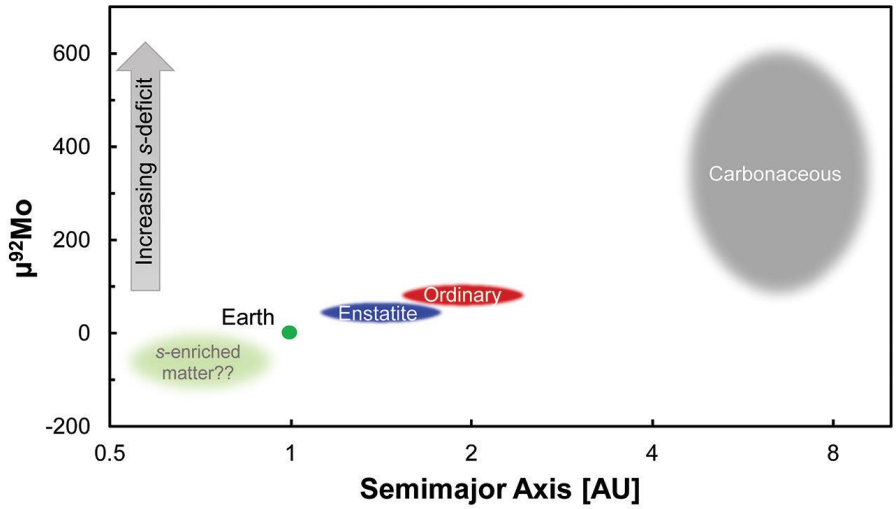

Figure 1.3: Proposed radial distribution of different types of chondrites based on the ^{92}Mo isotopic difference. The most reduced and volatile depleted enstatite chondrites originated from the innermost region (< 2 AU), moderately volatile rich and oxidised ordinary chondrites located further than enstatite chondrites and the most oxidised and volatile-rich carbonaceous chondrite formed in the giant planet region. Taken from Render et al. (2017).

et al. 2012; Fischer-Gödde & Kleine 2017) also proposed a heliocentric distribution of chondrites similar to Render et al. (2017). It has been suggested that Earth is isotopically closest to enstatite chondrite and thus mostly accreted it throughout its whole history (Dauphas 2017) (See also Sect. 1.3).

Currently, Mars is the only planet other than Earth that we have samples from (not counting the moon as a planet) and about a hundred kilograms of martian meteorites have been found on Earth. These samples that originated from the martian crust (Treiman et al. 2000) and mantle (Day et al. 2018) can be examined to measure its bulk composition. Thanks to the increase in the number of martian meteorites discovered and higher precision of isotopic measurements in the past 20 years, we now have the isotopic composition of Mars not only for O (e.g. Franchi et al. 1999), but also for Ca, Ti, Cr, Nd, Ni and Mo (Dauphas 2017 and references therein; Kruijer et al. 2017). Isotopic data for

highly siderophile elements, however, are still lacking due to their extremely low abundance in the martian meteorites (Righter et al. 2015). Nonetheless, comparing the isotopic composition of Mars with Earth's provides new constraints on planet formation models and planets' building blocks.

1.3 Building Mars with chondritic material

1.3.1 Isotopic differences between Earth and Mars

Indeed, the isotopic compositions of Earth and Mars are different. The strongest evidence for this comes from the three oxygen isotope system (expressed as $\Delta^{17}O = \delta^{17}O - 0.52\delta^{18}O$, where the δ-notation denotes deviations in parts-per-thousand where isotopic ratios are normalised to the standard and Δ expresses the deviation of these coupled ratios from the terrestrial mass-fractionation line of slope $m = 0.52$). Fig. 1.4 shows that data measured from martian meteorites in Franchi et al. (1999) plot on a mass-dependent fractionation line separated from Earth but with a same slope as Earth's. All the martian data points plotted above the terrestrial fractionation line indicates that bulk Mars is enriched in the minor oxygen isotope (with positive $\Delta^{17}O$) with respect to the terrestrial value (e.g. Franchi et al. 1999; Rubin et al. 2000; Mittlefehldt et al. 2008; Agee et al. 2013; Wittmann et al. 2015). Other isotopic systems, such as Titanium ($\varepsilon^{50}Ti$), Chromium ($\varepsilon^{54}Cr$) and Nickel ($\varepsilon^{64}Ni$), that trace nucleosynthetic processes in stars other than the Sun likewise show clear differences between average terrestrial and martian values (Trinquier et al. 2007, 2009; Regelous et al. 2008).

Isotopic differences are not unique to the terrestrial and martian samples. Different degree of isotope variability is also observed between various kind of

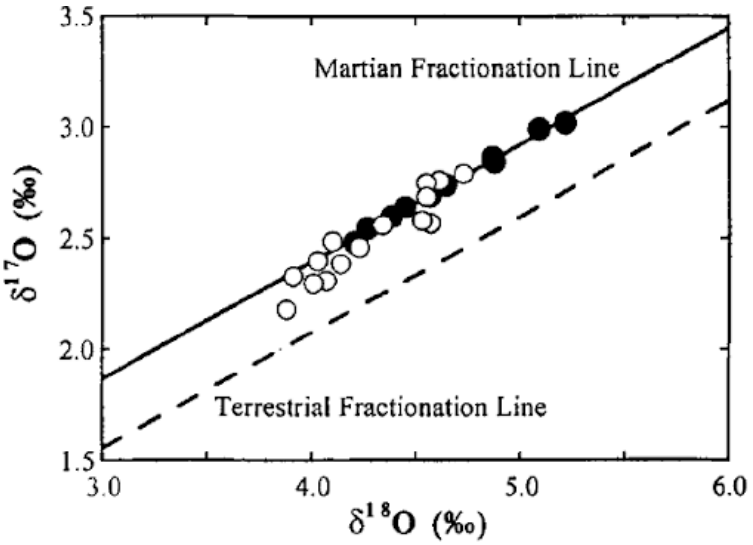

Figure 1.4: Oxygen three isotope plot of martian meteorites. The fact that data from martian meteorites (circles) plot on a separate but parallel fractionation line indicates the isotopic differences between Earth and Mars. Taken from Franchi et al. (1999).

meteorites (Warren 2011) (See also Fig 1.3). The cause of these isotopic anomalies at the planetary and bulk meteorite scale is still unknown. One possible scenario is that the injection of supernova material into the solar protoplanetary disk occured shortly before planetesimal formation began (Clayton 1977; Ouellette et al. 2007). This nucleosynthetic contamination is widely assumed to have been more influential in the composition of the outer regions of the disc (Qin et al. 2011; Brennecka et al. 2013). An alternative explanation of the isotopic anomalies is thermal processing and selective destruction of presolar carrier mineral during the collapse of the solar nebular (e.g. Trinquier et al. 2009; Burkhardt et al. 2012). This thermal processing, however, have difficulty in explaining the Cr isotopic anomaly in bulk-meteorite scale because the carrier of ^{54}Cr has high resistance to thermal destruction (Qin & Carlson 2016).

Although under debate, a number of studies have proposed that the heliocentric composition gradient of the solid disc can be mapped by the isotopic

differences of nucleosynthetic tracers that were implanted in different locations within the planet-forming disk (e.g. Fischer-Gödde & Kleine 2017; Render et al. 2017) (Fig. 1.3). Taken together, it has been proposed that isotopic compositional differences between Earth and Mars hint that they were formed with different mixtures of source components (Wänke & Dreibus 1988, 1994; Lodders 2000; Warren 2011; Brasser et al. 2017), with the further implication that source locations for the two worlds were different (cf. Fitoussi et al. 2016).

1.3.2 Bulk composition inferred from isotopic system

The difference between the source location(s) for components that gave rise to Earth and Mars is lent further credence by several recent isotope studies in terrestrial samples and martian meteorites. Assuming that the feed-stock for accretion of both Earth and Mars was dominated by chondritic material (meteorites that did not experience high pressure melting and differentiation of their parent bodies), analysis suggests that Earth should accrete about 70% enstatite chondrite, about 25% ordinary chondrite and less than 5% carbonaceous chondrite in order to reproduce the well-documented isotopic compositions of ^{17}O, ^{48}C, ^{50}Ti, ^{62}Ni or ^{64}Ni , ^{92}Mo and ^{100}Ru (Dauphas et al. 2014; Dauphas 2017; Fischer-Gödde & Kleine 2017). Mars, on the other hand, has a larger uncertainty in its bulk composition, which is suggested to be 45% enstatite chondrite and 55% ordinary chondrite to account for the planet's documented ^{17}O, ^{50}Ti, ^{54}Cr, ^{62}Ni and ^{92}Mo isotopic values as determined from the martian meteorites (Sanloup et al. 1999; Tang & Dauphas 2014). The earlier composition of Lodders & Fegley Jr (1997) of 85% ordinary chondrite based solely on oxygen isotopes is incompatible with the other systems. With a more rigorous analysis of uncertainties, Brasser et al. (2018) recorded 29% to 68% entatite chondrite and 32%

to 67% ordinary chondrite in their analysis, which is in agreement with previous studies within uncertainties. The generally higher portion of ordinary chondrite in Mars as compared to Earth underscores the differences in bulk composition between the two planets. Combining with the suggested heliocentric gradient of the initial solid disk (Morbidelli et al. 2012; Rubie et al. 2015; Render et al. 2017; Fischer-Gödde & Kleine 2017) (Fig 1.3), Brasser et al. (2017) argued that the formation region of Mars is likely to be further from the Sun than Earth, at least owning to the fact that its composition has a much higher computed fraction of ordinary chondrite.

1.4 Final stage of Mars' accretion - Late Veneer giant impact?

1.4.1 Highly siderophile element abundances in the martian mantle

Analysing martian meteorites not only provides information about the overall bulk composition of Mars, but also the very late portion of a planet's accretion. Some of the platinum group transition metals, such as Os, Ir, Ru, Rh, Pt, Pd are classified as "highly siderophile elements" (HSEs): they are depleted in the martian mantle (Day et al. 2016; Tait & Day 2018) relative to chondritic meteorites. A similar phenomenon has also been observed in the terrestrial and lunar mantles (Becker et al. 2006; Day et al. 2007). HSEs are "iron loving", which means that they rapidly dissolve in iron and are expected to be effectively stripped from silicate mantles into the growing metallic cores during planet formation (Chou 1978). Yet, the observed abundances of HSEs are

greatly enhanced relative to their predicted quantities in the silicate mantles of Earth and Mars. Experiments for HSE partition between liquid metal and silicate predict their abundance should be orders of magnitude lower than what is observed (e.g Kimura et al. 1974; Mann et al. 2012; Rubie et al. 2015). One theory invoked to explain this discrepancy is that the HSEs were delivered after silicate-metal differentiation (i.e. core formation) in the form of a Late Veneer (LV) impactor(s) of broadly chondritic composition (Chou 1978; Frank et al. 2016; Walker 2009). An alternative mechanism to explain this anomalous enrichment involves inefficient metal-silicate partitioning at high pressures and temperatures (e.g. Murthy 1991; Righter et al. 2015). A shortcoming of this mechanism, however, is that it cannot currently explain the chondritic relative abundance of the HSEs for both Earth and Mars (Walker 2009; Bottke et al. 2010; Day et al. 2016; Tait & Day 2018). Fig 1.5 shows the comparison of HSEs abundance in bulk silicate Mars (red points), bulk silicate Earth (green points) and lunar mantle (black points), normailised to CI-chondrite. The HSEs abundances obtained from the high pressure and high temperature experiments of Righter et al. (2015) are "non-chondritic" with high Ir/Os, Ir/Ru and low Re/Os (Day et al. 2016). Hence, a Late Veneer delivery of chondritic material is currently most favourable explanation of the HSEs abundances in the martian, terrestrial and lunar mantles.

Rubie et al. (2016) notes that the partition coefficients of some HSEs at high pressure (Mann et al. 2012) are too low to deplete the HSE abundances enough for the late veneer to overprint them. If core formation were the only HSE depletion mechanism, then we should expect that the HSE abundance pattern would be non-chondritic. This is, however, not the case: it is chondritic, and therefore consistent with a late veneer and not core formation at high pressure.

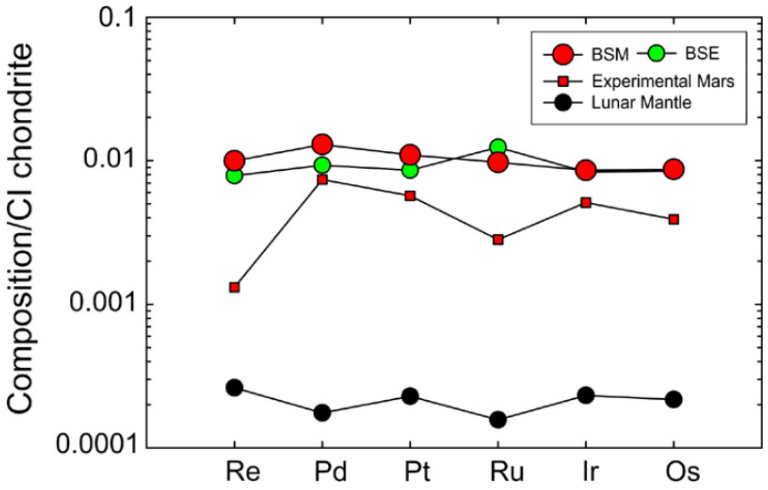

Figure 1.5: Comparison of highly siderophile elements' (HSEs) abundance in bulk silicate Mars (BSM, red points) measured from the martian meteorites, bulk silicate Earth (BSE, green points) and lunar mantle (Black points), normalised to CI-chondrite. The HSEs abundances obtained from high pressure and high temperature partitioning experiments (Righter et al. 2015), which are indicated by red squares, are "non-chondritic" with high Ir/Os, Ir/Ru and low Re/Os (Day et al. 2016). A Late Veneer of chondritic material delivery currently remains the most favourable explanation to the HSE abundances in the mantle of Mars, Earth and the Moon. Taken from Tait & Day (2018).

Consequently, there exist two options to interpret these data: either, 1) core formation occurred at low pressure, which is inconsistent with the patterns documented for moderately siderophile elements in mantle samples, or 2) the *Hadean Matte* hypothesis proposed by O'Neill (1991). The Hadean Matte is an event in which iron sulfide liquid exsoluted during magma ocean cooling and crystallisation, then it segregated into the core and further stripped away the HSEs in magma ocean (Rubie et al. 2016). This hypothesis still calls for a late veneer to deliver the HSEs observed in Earth's mantle today.

According to HSE abundances inferred from martian meteorites for Mars' mantle composition, the planet accreted at least 0.5 wt% of material of chondritic composition during the LV stage of late accretion (Walker 2009; Brandon

et al. 2012; Day & Walker 2015; Tait & Day 2018). The most likely contribution is computed to be ∼0.8 wt% (Day et al. 2016), a value comparable to that estimated for Earth's mass augmentation (∼0.7 wt%) from a similar event (Day et al. 2016). In contrast, the estimated LV to the Moon is only 0.02 – 0.035 wt% (Day et al. 2007; Day & Walker 2015; Kruijer et al. 2015; Touboul et al. 2015). This means that the ratio of accreted mass between Earth and the Moon is 1950 ± 650, which is more than two orders of magnitude higher than the ratio of their gravitational cross sections (∼20).

1.4.2 Evidences of a Late Veneer giant impact on Mars

Bottke et al. (2010) proposed that the majority of the mass delivered to Earth after primary accretion could come from a few massive objects the size of Ceres (950 km in diameter) or larger, which lingered behind as left-overs from terrestrial planet formation. The small number of such massive objects in the inner Solar System at that time statistically favours collision with Earth over the Moon (Sleep et al. 1989; Bottke et al. 2010). This hypothesis was further developed by Brasser et al. (2016b), who combined the results of N-body and Monte-Carlo impact simulations to conclude that most of the Earth's LV came from a single lunar-sized impactor in the first 100 Myr of the history of the Solar System. By adopting the same method for Mars, Brasser & Mojzsis (2017) suggested that a similar but smaller impact affected the red planet. With the size-frequency distribution of the leftover planetesimals assumed to be identical to the current asteroid belt, Mars is expected to have merged with a Ceres-sized object if it accreted 0.7 to 0.8 wt% during the LV (Brasser & Mojzsis 2017).

If such a colossal impact did occur on Mars, topographical evidence may be imprinted on the crustal surface of Mars. Some studies propose that the martian

hemispheric dichotomy exemplified by the northern lowlands region (dubbed the Borealis Basin) was formed by a single giant impact from an object with a diameter ranging from 1000 – 2700 km (Wilhelms & Squyres 1984; Andrews-Hanna et al. 2008; Nimmo et al. 2008; Marinova et al. 2008; Hyodo & Genda 2018). Although the size of the impactor estimated by Brasser & Mojzsis (2017) is at the lower end of this range, assuming the accretion efficiency to be only 10% to 50% would increase the impactor's diameter to 1400 – 2300 km (Bottke & Andrews-Hanna 2017), which matches the above estimation for the Borealis-Basin-forming impactor. The martian moons Phobos and Deimos may provide further evidence for such a hypothetical colossal impact because the event would likely eject a vast amount of debris into a circum-martian disc to eventually form the martian satellites (Craddock 2011; Rosenblatt & Charnoz 2012; Citron et al. 2015; Rosenblatt et al. 2016). The highly circular and co-planar orbits of Phobos and Deimos argue for the giant impact hypothesis. Hence, the composition of Phobos and Deimos is predicted to be a mixture of the martian mantle and the impactor (Rosenblatt et al. 2016; Hyodo et al. 2017).

1.4.3 The timing of Mars' Late Veneer event

The minimum timing for this postulated LV impact on Mars can be potentially constrained from ancient igneous zircons in martian meteorites. Zircon U-Pb geochronology performed on martian meteorite NWA7533 yields 4428 Ma ages (Humayun et al. 2013). Recent results reveal even older ages, ranging from 4430 – 4480 Ma in the meteorite NWA7034 (Bouvier et al. 2018), which is a paired meteorite with NWA7533 (Agee et al. 2013). Zircons in these meteorites are present in matrix material as fragments as well as in evolved igneous clasts perhaps formed by re-melting of the primary martian crust either at depth in the

presence of volatiles (Stolper et al. 2013), or by differentiation of large impact melt sheets (Humayun et al. 2013). Indications are that a crust has existed on Mars since 4547 Ma, which implies that magma ocean crystallisation of Mars occurred rapidly after Solar System formation: the primordial martian crust formed within 20 Myr (Bouvier et al. 2018). Although this rapid magma ocean crystallisation is fully consistent with theoretical models (e.g. Elkins-Tanton 2008; Lebrun et al. 2013; Hamano et al. 2013), it appears to be at odds with the Sm-Nd systematics of the martian SNC meteorites, which require at least a shallow long-lived magma ocean for ∼60 – 100 Myr (Debaille et al. 2007; Borg et al. 2016). Yet, the latter conclusion is based on the abundance of short-lived radionuclides in young martian meteorites and therefore may insinuate a younger fractionation event in the regional mantle scale rather than the actual martian crust solidification timescale (Bouvier et al. 2018). The relatively late formation of the zircons has been attributed to a LV colossal impact near 4480 Ma that melted a part of the martian crust (Bouvier et al. 2018).

1.4.4 Aftermath of a giant impact

A Ceres-sized impactor that collided during the pre-Noachian eon (4500 – 4100 Ma) should profoundly affect the early surface environment of Mars. Objects with diameter >1000 km are expected to be differentiated (Stevenson 1981), with a metal core and a silicate mantle. Genda et al. (2017a) showed that, under certain conditions, a dense (∼80 – 90 bar) hydrogen atmosphere can be generated after a differentiated lunar-sized object collided with Earth during late accretion. Depending on the Solar extreme ultraviolet (EUV) models, this post-impact atmosphere may have persisted on Earth for ∼100 – 200 Myr. The impactor's iron core materials are flung into geocentric orbit upon impact,

and then sheared and fragmented into smaller drops, which later descended back onto the terrestrial surface as mm-scale metallic hail. Hydrogen gas is generated through oxidation of falling metallic iron to the Earth either by the reaction with a global surface ocean or an oxidized Hadean mantle (Abe 1993; Genda & Abe 2005).

Provided that pre-Noachian Mars had adequate global surface water (or surface ice) at time of an LV colossal impact, a similar, but less massive collision (Brasser & Mojzsis 2017) ought to likewise yield a transient hydrogen-rich atmosphere. Hydrogen molecules collide frequently under high pressure ($\sim$2 bar) and hence possess transient dipole moments that induce infrared absorption (Pierrehumbert & Gaidos 2011). A hydrogen greenhouse on early Mars (Ramirez 2017; Ramirez & Kaltenegger 2017) could in principle provide an reducing atmospheric factory for organic chemistry (Urey 1952; Miller et al. 1953), such as RNA formation (Ferus et al. 2017), and maintain an early warm climate even if it was for a short time. This has obvious implications for the origin of life on Mars in the planet's first hundred million years.

1.5 Outline and the novelty point of the thesis

The aim of this thesis is to explore the first hundred million year of Mars' evolution: from its formation to the final accretion it received. In the next chapter, I will unveil a new method for studying Mars' and also other terrestrial planets' formation: combining the current dynamical models with isotopic data measured from chondrites and the martian meteorites.

This is the first comprehensive research to adopt the isotopic compositional

difference between Earth and Mars to constrain N-body planet formation models. We present results for more than 600 simulations in total of the Classical and the Grand Tack model, which is more than a factor of 10 higher than the above-mentioned studies on terrestrial planets' composition. Such a huge amount of simulations is required in order to carry out statistical analysis on the composition of the terrestrial planets because the terrestrial planets' formation is a chaotic process. A small change of the initial conditions can form a totally different system. While the previous studies (O'Brien et al. 2006; Rubie et al. 2015) cannot perform such kind of statistical analysis due to a low number of simulations (less than 10), these studies only focused on the composition of planets in each particular simulation. In addition to a much higher number of simulations, we also have a higher resolution for the simulations. In some simulations of our study, there are about 3000 planetesimals and embryos, which is a massive improvement compared to those earlier studies mentioned which usually contain less than 1500 particles in the disc. Some earlier studies do not even include planetesimals (Chambers 2001; Raymond et al. 2004). Also, our study is the first in adopting the oligarchic initial condition for the embryos (Kokubo & Ida 1998) in computing a planet's bulk composition in the both the Classical and the Grand Tack model. We specified chondrites as the building blocks of the terrestrial planets, while previous research did not explicitly assume any classes of meteorites as the building blocks, and instead only focused on water fraction, equilibrium condensation (the HSC chemistry model) or ignored composition altogether.

In Ch. 3, the consequence of a Late Veneer (LV) giant impact on Mars will be examined with hydrodynamic simulations following by analytical estimation on the generated hydrogen atmosphere (see Sect. 1.4). This is the first work

attempting to study the consequence of the martian LV giant impact, which includes how the HSEs are delivered to the martian mantle and what is the amount and the lifespan of the post-giant-impact hydrogen atmosphere on Mars. None of the previous studies attempted to answer these questions. We are not concerned about the originality of the method because applying the same Smoothed particle hydrodynamic (SPH) method as Genda et al. (2017a) is sufficient for us to answer the above questions as the first step of our study on the LV of Mars. Compared to Genda et al. (2017a), we improved the hydrogen atmosphere lifespan estimation by considering different stellar models (Tu et al. 2015) instead of only applying the radiation scaling law of Ribas et al. (2005) (see Sect. 3.6.1). We further discuss the escape of the hydrogen atmosphere with the xenon isotopic composition of the ancient martian atmosphere inferred from the martian meteorites (see Sect. 3.6.3), whereas Genda et al. (2017a) does not combine their simulation data to the documented atmospheric data from Earth. Coupling cosmochemical data with numerical data is the core idea of this thesis and it is important for understanding the early history of Mars. Certain experts in the cosmochemical and dynamical communities have encouraged me to continue this work because they believe this is the future to which the field is evolving.

Finally, the thesis will be concluded with discussion on the approximations, strengths and weaknesses of our study. We also suggest future improvements on studies related to Mars' formation and evolution (Ch. 4).

Chapter 2

Formation of Mars: coupling dynamical and cosmochemical results

2.1 Objective and outline of this chapter

Motivated by the isotopic data obtained from the terrestrial and martian samples, we want to gain a better understanding on why Mars is different from Earth (see Sect. 1.3 for the background). The aim of this chapter is to investigate the possibility of producing different Earth and Mars isotopic compositions with both the Classical and the Grand Tack model from the results of our N-body simulations (see Sect. 1.1 for discription of the each model). The setup of our simulations is described in Sect. 2.2. We first analyse the simulation results via comparison of the accretion zone of the Earth and Mars analogues in Sect. 2.3. Next, we estimate the average percentage of enstatite chondrite and ordinary chondrite incorporated into Earth and Mars by assuming the initial solid

disc is composed of only enstatite chondrite in the inner region and ordinary chondrite in the outer region; alternatively, we test a scenario wherein the disc is effectively mixed with planetesimals and embryos of random compositions (see Sect. 2.4). Finally, we calculate the expected isotopic composition of ^{17}O, ^{50}Ti, ^{54}Cr, ^{142}Nd, ^{64}Ni and ^{92}Mo in the martian mantle (Sect. 2.5) so as to examine how the orbital dynamics affects Mars' isotopic composition. Studies in this chapter are performed under collaboration with Prof. Ramon Brasser (Earth-Life Science Institude), Dr. Soko Matsumura (University of Dundee), Prof. Stephen Mojzsis (University of Colorado Boulder) and Prof. Shigeru Ida (Earth-Life Science Institude). Most of the results of this chapter have been published in Woo et al. (2018).

2.2 Simulation set up and previous work

To estimate the possibility of reproducing Mars with a composition that is different from Earth's, we analyse the data from a high number of N-body simulations for the Grand Tack and the Classical model. The simulations and data used to examine the Grand Tack model were previously discussed in Brasser et al. (2016a), and we refer the reader to that work. We first briefly summarise their initial conditions and the organisation of the simulations.

In Brasser et al. (2016a), the formation of terrestrial planets were studied in the Grand Tack scenario by focusing on the traditional dynamical perspectives, which are the final orbital architecture and the masses of the terrestrial planets. A tack location for Jupiter at both 1.5 AU and 2 AU was considered, where the tack location is the position at which Jupiter reversed its migration. Two types of initial conditions for planetestimals and embryos were adopted:

Table 2.1: Initial number of embryos per simulation of each subset of the simulations with equal-mass embryos. They are classified by different masses of embryos, $M_{\rm emb}$ and different mass ratio of embryos to planetesimals, $M_{\rm emb}$:$M_{\rm pl}$.

	$M_{\rm emb}$:$M_{\rm pl}$		
$M_{\rm emb}$	1:1	4:1	8:1
0.025 $M_\oplus$	86	159	211
0.05 $M_\oplus$	43	80	106
0.08 $M_\oplus$	27	50	66

the equal-mass case, and the oligarchic case (embryos resulting from the oligarchic growth of planetesimals). Brasser et al. (2016a) employed the initial condition of embryos and planetesimals from Jacobson & Morbidelli (2014) for the equal-mass case, in which embryos in the same simulation have the same initial masses. The initial embryo masses are either 0.025, 0.05 or 0.08 $M_\oplus$, where $M_\oplus$ is the mass of Earth. All the embryos were embedded in a disc of planetesimals. The total mass ratio of the embryos to planetesimals is either 1:1, 4:1, or 8:1. In total there are nine different subsets of initial condition for the equal-mass initial condition. They performed 16 simulations in each subset; in total 144 simulations for each tack location of Jupiter. Table 2.1 shows the initial number of embryos in these nine subsets. The number of embryos increases with the mass ratio of embryos to planetesimals but decreases with the masses of embryos. They kept the number of planetesimals at 2000. The initial densities of embryos and planetesimals are 3 g cm^{-3}.

In addition to forming terrestrial planets with equal-mass embryos, Brasser et al. (2016a) also ran simulations with the initial conditions that are computed from the traditional oligarchic growth of the planetesimals (Kokubo & Ida 1998). Kokubo & Ida (1998) found that the orbital repulsion between embryos keeps their mutual separation wider than about 5 $R_{\rm Hill}$ during the oligarchic growth of the planetesimals, where $R_{\rm Hill}$ is the mutual Hill radii of two adjacent embryos.

The oligarchic initial condition is more realistic compared to the equal mass initial condition because it is a result from the actual study of planetary embryo formation. Brasser et al. (2016a) applied the semi-analytical oligarchic approach of Chambers (2006). First, they calculated the total solid mass between 0.7 and 3 AU according to the minimum mass solar nebula $\Sigma_s = 7$ g cm^{-2}(a/1AU)$^{-3/2}$ (Weidenschilling 1977; Hayashi 1981). Second, they increased the solid density at the ice line by a factor of three following the study of Ogihara & Ida (2009). The ice line was assumed to be static at 2.7 AU. Third, they set the spacing between the embryos to 10 $R_{\rm Hill}$ based on the results of Kokubo & Ida (1998); although in our work we ran additional runs with 7 and 5 $R_{\rm Hill}$. The spacing was computed assuming that embryos had their isolation masses, $m_{\rm iso} = 2\pi ab\Sigma_s$, where a is the semi-major axis of embryo and b is the spacing between adjacent embryos (Chambers 2006). Here $m_{\rm iso}$ represents the largest mass of an embryo if it accretes all the solid mass within the annulus $2\pi ab$. The semi-major axis of embryo n is $a_n = a_{n-1}[1 + b(2m_{\rm iso}/3M_\odot)]$, which nearly follows a geometric sequence, where $M_\odot$ is the solar mass.

Other than calculating the spacing and the semi-major axis of embryos, the initial masses of embryos also needed to be computed. Following Chambers (2006), the mass of embryos increases up to their isolation mass as

$$m_{\rm p}(t) = m_{\rm iso}\tanh^3(t/\tau), \tag{2.1}$$

where τ is the growth timescale, which depends on the semi-major axis a of the embryo, embryo spacing b, solid surface density Σ_s and the radii of planetesimals that assembled into the embryo, and t is the age of the solid disc. Chambers (2006) assumed a planetesimal size of 10 km in calculating τ , which was also adopted by Brasser et al. (2016a). By substituting $t = 0.5$ Myr, 1 Myr, 2 Myr

Table 2.2: Initial number of embryos per simulation of each subset of the simulations with oligarchic embryos. They are classified by different ages of the solid disc and different spacing between adjacent embryos in units of mutual Hill radii, $R_{\rm Hill}$.

	Mutual Hill radii spacing		
Disc age (t)	10 $R_{\rm Hill}$	7 $R_{\rm Hill}$	5 $R_{\rm Hill}$
0.5 Myr	29	43	63
1 Myr	31	52	86
2 Myr	31	52	86
3 Myr	29	49	80

The total mass of solids is the same in each subset of simulation.

or 3 Myr into Eq. (2.1), they obtained four different subsets of initial condition for the oligarchic growth scenario. They performed 16 simulations for each t, 64 in total for each tack location of Jupiter with 10 $R_{\rm Hill}$ embryo spacing. We perform more simulations with 5 and 7 $R_{\rm Hill}$ embryo spacing (64 for each), but only for a tack location of Jupiter at 1.5 AU. Figure 2.1 shows the initial masses of the embryos as a function of their initial semi-major axes for the oligarchic initial condition. Different colours correspond to different ages of the solid disc. By comparing the squares with different colours, we observe that embryos with similar initial semi-major axes have larger masses if the solid disc is older. This is because embryos accrete more planetesimals within the disk if the solid disc exists for a longer time. The initial number of embryos is larger in the 1 Myr and 2 Myr disc (see Table 2.2). We also compare the initial number of embryos with different initial $R_{\rm Hill}$ separation in Fig. 2.1, but only for the 0.5 Myr disc. Comparing the red points with the same initial semi-major axes with different shapes, the mass of embryos is lower but the initial number of embryos is larger if they have smaller mutual separation (see Table 2.2).

The system consisting of gas giants, planetary embryos, and planetesimals was then simulated with the symplectic integrator package SyMBA (Duncan

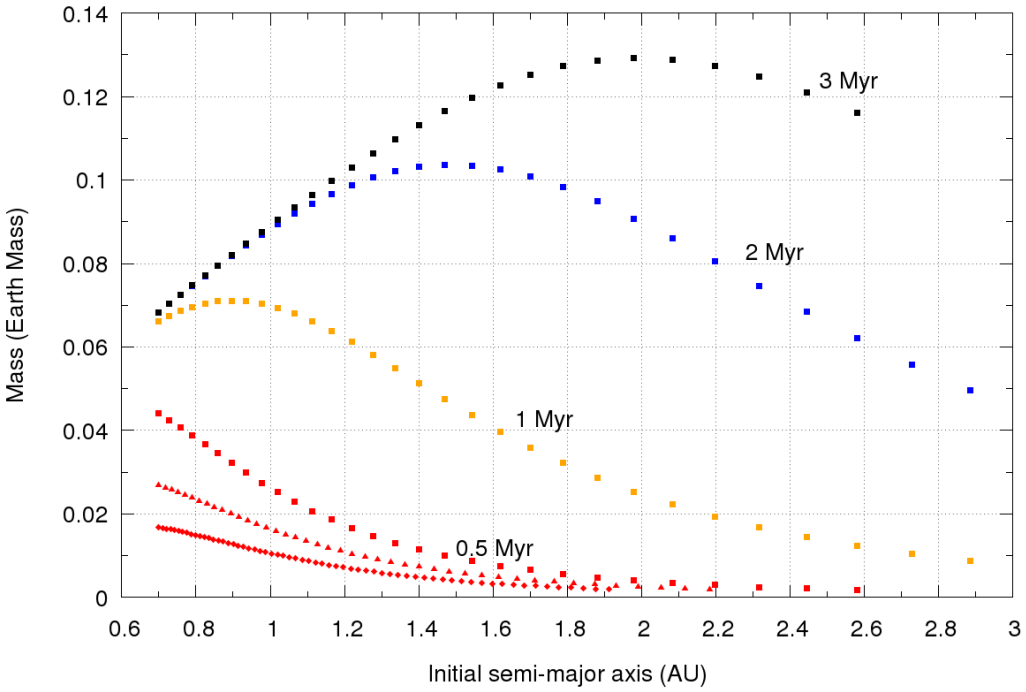

Figure 2.1: The initial masses of embryos against their initial semi-major axes for the oligarchic initial condition. The red points are embryos in a 0.5 Myr disc, orange points are in a 1 Myr disc, blue points are in a 2 Myr disc and black points are in a 3 Myr disc. Different point shapes represent different separation between adjacent embryos. Squares depict embryos separated by 10 $R_{\rm Hill}$ from each other, triangles are embryos with a spacing of 7 $R_{\rm Hill}$ and rhombuses are embryos with spacing of 5 $R_{\rm Hill}$. The comparison of different spacing between embryos is only plotted for the 0.5 Myr disc.

et al. 1998) for 150 Myr using a time step of 7.3 days (See Appendix A for the detail decription of SyMBA). The migration of Jupiter and Saturn was mimicked through the fictitious forces (Walsh et al. 2011). The gas disc developed by Bitsch et al. (2015) was adopted, which is different from the one adopted by Walsh et al. (2011) and has a higher surface gas density. The initial gas surface density profile scales as $\Sigma(r) \propto r^{-1/2}$ and the temperature profile is $T(r) \propto r^{-6/7}$, where r is the radial distance to the Sun. Both gas surface density and temperature decay until 5 Myr after the start of simulation, after which the disk is artificially photo-evaporated away with the e-folding time 100 kyr (Bitsch et al. 2014). The existing gas disc caused type-I migration and tidal damping of the eccentricities of the planetary embryos. The planetesimals are affected by the gas drag, for which Brasser et al. (2016a) assumed each planetesimal had a radius of 50 km.

We also study the Classical model, but only for the oligarchic initial condition (10 $R_{\rm Hill}$ and 5 $R_{\rm Hill}$ between adjacent embryos) due to limited computational resources. In other words, we used the same oligarchic initial condition as the Grand Tack model but placed Jupiter and Saturn on their current orbits. Also, the Classical model does not have a gas disc. The time step and the total simulation time for each simulation in the Classical model is the same as the Grand Tack model (150 Myr). We test the Classical model with 10 $R_{\rm Hill}$ and 5 $R_{\rm Hill}$ mutual spacing between embryos.

2.3 Comparison of accretion zones between Earth and Mars

In this section, we study the bulk composition difference between Earth and Mars by computing the accretion zone of planets formed after performing simulations of planet formation for 150 Myr. We first define the accretion zone of each planet.

2.3.1 Definition of accretion zone

We calculate the composition of the planets that formed in the current region of the terrestrial planets. Assuming the disc follows a simple relation between isotopic ratios and distance to the Sun (see Sect. 1.3), the bulk composition of each planet can be roughly quantified by tracking the initial heliocentric distance of the material (either embryos or planetesimals) accreted into each planet. Therefore, the mass-weighted mean initial semi-major axis of incorporated materials,

$$a_{\rm mwmi} = \frac{\sum_i^N m_i a_i}{\sum_i^N m_i}, \tag{2.2}$$

was calculated for each terrestrial planet analogue. Here m_i and a_i are the mass and initial semi-major axis of the accreted object i, and N is the total number of embryos and planetesimals incorporated into the planet (Kaib & Cowan 2015; Brasser et al. 2017; Fischer et al. 2018). Planets with similar $a_{\rm mwmi}$ should have a similar bulk composition. The weighted standard deviations of $a_{\rm mwmi}$ are computed as,

$$\sigma_{\rm w} = \sqrt{\frac{\sum_i^N m_i (a_i - a_{\rm mwmi})^2}{\frac{(N-1)}{N} \sum_i^N m_i}}. \tag{2.3}$$

$a_{\rm mwmi} \pm \sigma_{\rm w}$ indicates the accretion zone of a planet analogue, which is the main region of the disc that the planet analogue sampled; $\sigma_{\rm w}$ is defined as zero if the planet did not accrete any planetesimal or embryo. In other words, $a_{\rm mwmi}$ provides us with the average formation distance and $\sigma_{\rm w}$ with the planet's typical feeding zone.

2.3.2 Classical model: Oligarchic initial condition

Figure 2.2 depicts the $a_{\rm mwmi}$ of Venus analogues (orange), Earth analogues (blue) and Mars analogues (red) as a function of their final semi-major axes for the oligarchic initial condition of the Classical model with Jupiter and Saturn on their current orbits. The results of initial embryos with spacing of 10 $R_{\rm Hill}$ and 5 $R_{\rm Hill}$ spacing, as well as different disc ages t are combined here. Venus, Earth, and Mars analogues are defined as having masses and semi-major axes within the ranges (0.4 $M_\oplus < m_p <$ 1.2 $M_\oplus$, 0.55 AU $< a <$ 0.85 AU), (0.5 $M_\oplus < m_p <$ 1.5 $M_\oplus$, 0.85 AU $< a <$ 1.15 AU) and (0.05 $M_\oplus < m_p <$ 0.15 $M_\oplus$, 1.3 AU $< a <$ 1.7 AU) (Brasser et al. 2016a). The error bars are $\pm\ \sigma_w$, which represent the accretion zone of each planet (see Sect. 2.3.1).

We find that most of the Earth (blue) and Venus (orange) analogues have 1 AU $< a_{\rm mwmi} <$ 1.5 AU and their error bars share a similar range in Fig. 2.2, which implies that their accretion zones, and therefore their bulk compositions, are likely to be similar. There is a possibly weak trend of planets with larger final semi-major axes having larger $a_{\rm mwmi}$. A similar but stronger trend has been observed in the simulations performed by Kaib & Cowan (2015) for the Classical

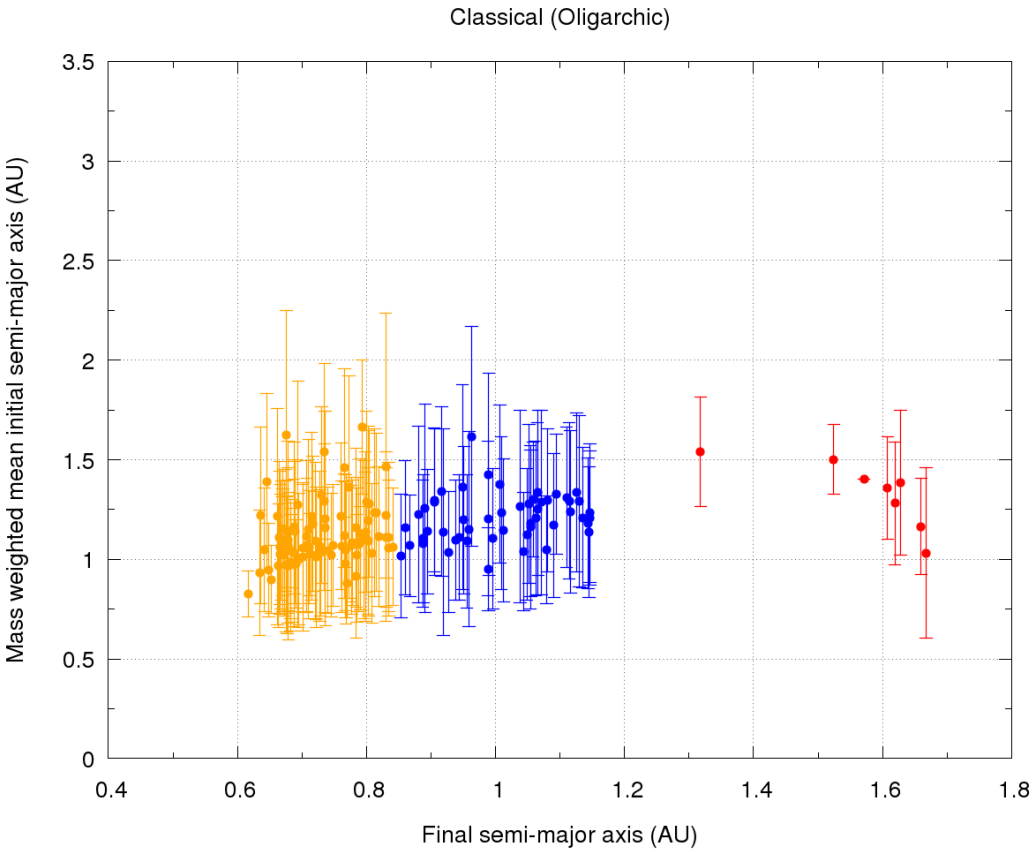

Figure 2.2: Mass-weighted mean initial semi-major axis (a_{mwmi}) of material accreted into each Venus analogue (orange), Earth analogue (blue) and Mars analogue (red) as a function of their final semi-major axis for the oligarchic initial condition of the Classical model. We combine the results of 10 and 5 R_{Hill} and different ages of the solid disc (either t = 0.5, 1, 2 or 3 Myr) within this plot.

model. One possible reason is that the inner edge of our initial solid disc was truncated at 0.7 AU, while that of Kaib & Cowans disc had an inner edge at 0.5 AU. If the initial solid disk is extended to a region closer to the Sun, the Venus analogues should accrete more material that originated from the inner-most region of the disc. Therefore, most of the Venus analogues would sample the disc closer to the Sun than the Earth analogues do and generate a more obvious linear trend between $a_{\rm mwmi}$ and the final semi-major axis. Comparing Earth (blue) with Mars (red) in Fig. 2.2 leads us to a similar conclusion, since six out of eight of the Mars analogues have 1 AU $< a_{\rm mwmi} <$ 1.5 AU and the error bars of all the red and blue points share a similar range. Therefore, the Classical model predicts a similar bulk composition between Venus, Earth, and Mars. That is to say, the Classical model inadequately explains the bulk composition difference between Earth and Mars if we are able to form Mars with its current mass. If this restriction is ignored, it is possible to form a distinct Earth and Mars (See Sect. 2.4).

Table 2.3 lists the outcomes statistics for all sets of simulations performed in this study. The number of Venus and Earth analogues we obtained from the Classical model is similar to the oligarchic simulation of the Grand Tack model. The formation probabilities for Venus and Earth analogues in the Classical model are also similar with the Grand Tack model, with Venus having a higher formation probability ($\sim$0.2 - 0.3) than Earth ($\sim$0.1). The situation is different for Mars. We find only 8 planets in total locating at 1.3 to 1.7 AU fall within a satisfactory mass range for Mars within the Classical model. This is far fewer than those obtained from the Grand Tack simulations. Mars' formation probability in the Classical model ($<$0.02) is much lower than in the Grand Tack model ($\sim$0.05 to 0.10). The reason is that most of the planets formed near

Table 2.3: The total number of planets and terrestrial planet analogues formed in each set of simulations. The numbers in the blankets represent the formation probability of each planet, which is the total number of the planet analogue over the total number of planets. Planets are the remaining objects at the end of simulation other than the gas giants that have masses $> 0.01\ M_{\oplus}$. The definition of Venus, Earth and Mars analogues are defined in Sect. 2.3.2.

Simulation set	No. of simulations	Planets	Venus analogues	Earth analogues	Mars analogues
Grand Tack					
Equal mass embryos	144	635	151	62	59
Tack at 1.5 AU			(0.24)	(0.10)	(0.09)
Grand Tack					
Equal mass embryos	144	685	121	90	32
Tack at 2 AU			(0.18)	(0.13)	(0.05)
Grand Tack					
Oligarchic 10 $R_{\rm Hill}$	64	210	70	22	17
Tack at 1.5 AU			(0.33)	(0.10)	(0.08)
Grand Tack					
Oligarchic 10 $R_{\rm Hill}$	64	273	57	37	14
Tack at 2 AU			(0.21)	(0.14)	(0.05)
Grand Tack					
Oligarchic 7 $R_{\rm Hill}$	64	231	59	27	18
Tack at 1.5 AU			(0.26)	(0.12)	(0.08)
Grand Tack					
Oligarchic 5 $R_{\rm Hill}$	64	250	59	22	19
Tack at 1.5 AU			(0.24)	(0.09)	(0.08)
Classical					
Oligarchic 10 $R_{\rm Hill}$	64	225	50	22	4
			(0.22)	(0.10)	(0.02)
Classical					
Oligarchic 5 $R_{\rm Hill}$	64	253	45	30	4
			(0.18)	(0.12)	(0.02)

Please refer to Sect. 2.2 for the classification of the simulation groups.

Mars' current position have masses larger than the value that we defined for Mars analogues ($> 0.15\ M_{\oplus}$). Since Jupiter and Saturn did not migrate inward and clear the region of the current Mars and the asteroid belt, the solid density in between 1 to 2 AU is generally high enough to form a planet with about the half of Earth's mass. The average mass of the planets within $1.3 < a < 1.7$ AU in the Classical's simulations is $0.45 \pm 0.29\ M_{\oplus}$, which is more than four times the mass of Mars. As previously mentioned in Section 1.1, the biggest problem of the Classical model is that it forms a Mars that is too massive (e.g. Chambers 2001; Raymond et al. 2009).

2.3.3 Grand Tack: Oligarchic initial condition

Figure 2.3 resembles Fig. 2.2, but depicts the results from the Grand Tack simulations with oligarchic initial conditions. The results of the tack at 1.5 AU and 2 AU of Jupiter, as well as different adjacent embryo spacing and disc ages, are all plotted in Fig. 2.3. Similar to Fig. 2.2, most of the Venus and Earth analogues have $a_{\rm mwmi}$ between 1 and 1.5 AU. A few of them have $a_{\rm mwmi}$ smaller than 1 AU; these planets sample the innermost portion of the disc. Statistics of the Mars analogues suggest that their bulk composition is likely to be similar to both Earth and Venus since only ∼13% of the Mars analogues within the oligarchic simulations have $a_{\rm mwmi} > 1.5$ AU, and their error bars in Fig. 2.3 mostly share the same range with the Venus and the Earth analogues. Only two Mars analogues in our output have $a_{\rm mwmi} > 2$ AU. We return to this type of Mars analogue below (Sect. 2.3.4). According to the oligarchic Grand Tack simulations, the bulk compositions of Venus, Earth and Mars are likely to be similar.

It is worth pointing out that about one-quarter of the Mars analogues have

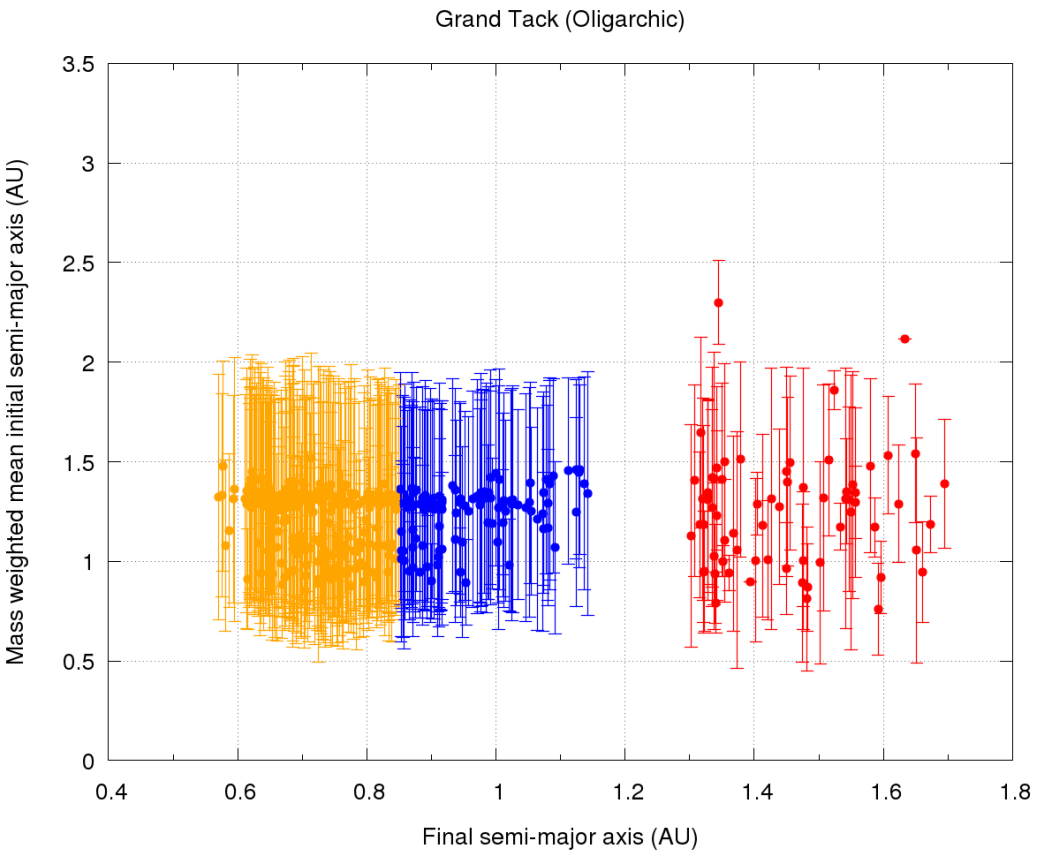

Figure 2.3: As in Fig. 2.2, but for the Grand Tack model with oligarchic initial condition. The results of Jupiter tacked at 1.5 AU or 2 AU, as well as different initial spacing between adjacent embryos (either 10, 7 or 5 $R_{\rm Hill}$) and different ages of the solid disc (either t = 0.5, 1, 2 or 3 Myr) are combined.

$a_{\rm mwmi} \leq 1$ AU. This fraction is even higher than the fraction of the Earth analogues with $a_{\rm mwmi} \leq 1$ AU. Therefore, the oligarchic Grand Tack simulation results show that it is possible for Mars to be formed in the innermost region of the protoplanetary disc and then scattered to its current location. This was also suggested by Hansen (2009) and Fitoussi et al. (2016) and might be taken as a natural explanation for the formation of Mars; that is if we do not consider its isotopic compositional difference from Earth (Brasser et al. 2017).

Reducing the spacing of embryos (from 10 $R_{\rm Hill}$ to either 7 $R_{\rm Hill}$ or 5 $R_{\rm Hill}$) produces different sets of initial condition with a lower average individual embryo mass and a higher initial number of embryos (See Fig. 2.1 and Table 2.2). Table 2.3 shows the statistics of 5 and 7 $R_{\rm Hill}$ spacing for the oligarchic Grand Tack simulations. The statistics of both 5 and 7 $R_{\rm Hill}$ spacing are similar to that of 10 $R_{\rm Hill}$, which indicates that the final results are not strongly dependent on the initial separation of the embryos.

2.3.4 Grand Tack: Equal mass initial condition

Figure 2.4 is similar to Fig. 2.3, but shows the result of the equal-mass initial condition of the Grand Tack model where Jupiter tacked at either 1.5 AU or 2 AU. This plot resembles the previously published Figs. 2 and 8 of Brasser et al. (2017), but we highlight the terrestrial planet analogues in our plot.

Similar to the oligarchic initial condition, we find that nearly all of our Venus, Earth, and Mars analogues have error bars that share a similar range of uncertainty. As such, most of the terrestrial planet analogues can be seen to have sampled a similar region of the disc. The value $a_{\rm mwmi}$ needs to be $>$ 2 AU if the error bars of the Mars analogues are not in the same range as all of the Venus and Earth analogues. The Mars analogues with $a_{\rm mwmi} > 2$ AU

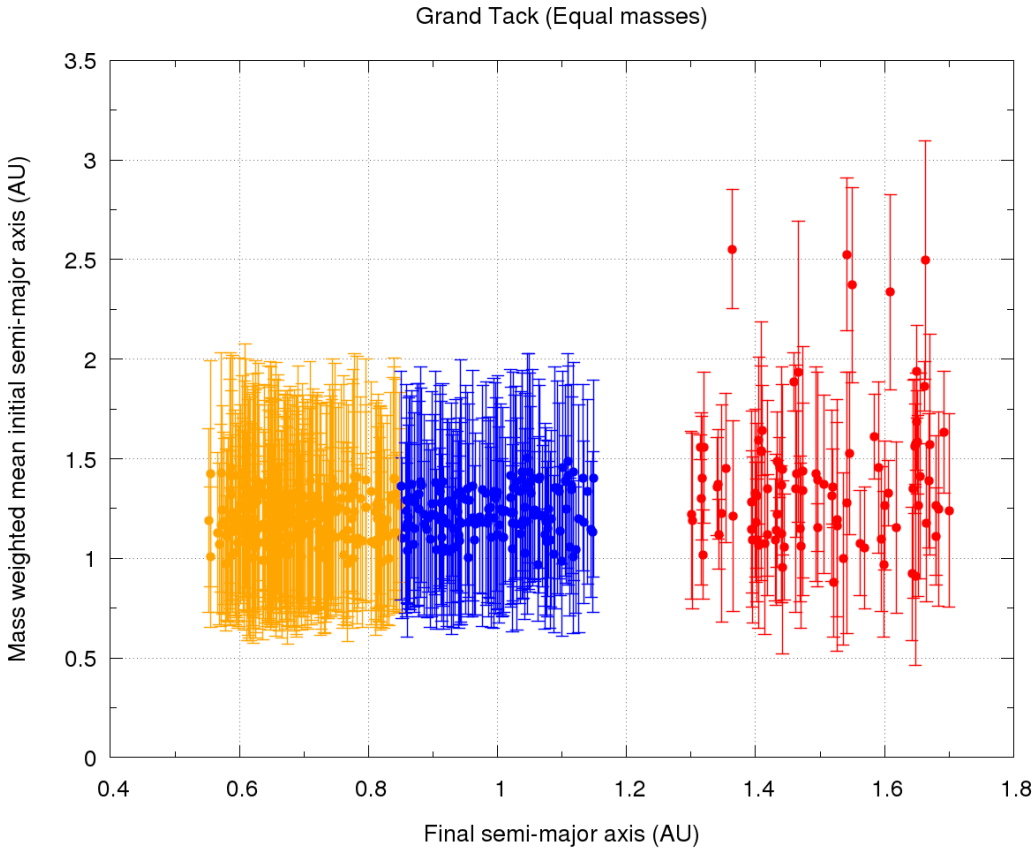

Figure 2.4: As in Fig. 2.3 but for the equal-mass initial condition. This plot is similar to Figs. 2 and 8 in Brasser et al. (2017), but we only show the Venus (orange), Earth (blue) and Mars (red) analogues.

are the ones that we are searching for because those Mars analogues would have a very different accretion zone with the Venus and Earth analogues. They formed in the outer region of the disc and accreted material mainly from there. Then Jupiter migrated outwards and hence scattered them close to the current location of Mars. This did not occur for Earth since we do not find any Earth analogue with $a_{\rm mwmi} > 2$ AU. There are seven of the Mars analogues (less than 5%) with $a_{\rm mwmi} > 2$ AU in total in the Grand Tack simulations (including all the simulations with equal mass and oligarchic initial condition). We find none of them in the Classical simulations.

The full distribution of the initial semi-major axis of the solid materials incorporated into Venus, Earth and Mars analogues is presented in Fig 2.5. We relaxed the constraint by not considering the mass of Mars analogues for the Classical model. As expected, Venus accreted the highest weight percentage ($\sim$50%) of its materials from the inner most region of the disc (<1 AU). Both Earth and Mars accreted more than 60% of their masses from the 1 to 2 AU region. This agrees with the accretion zones analysis since Earth's and Mars' accretion zone are mostly overlap regardless of the formation model. The mass contributed from the region further than 2 AU is limited (<5%) for all planets in the Classical model due to limited mixing. This >2 AU material increases to $\sim$10% for Mars in the Grand Tack model, mainly because of Jupiter's migration pushing the materials further than 2 AU to form an annulus in the region of the inner Solar system.

We obtained 635 planets in total when the tack location was at 1.5 AU and 685 planets when the tack location was at 2 AU, which greatly exceeds the results from the oligarchic initial condition (See Table 2.3). The main reason for this is that we have more simulations per set when using the equal-mass initial condition. We only performed 64 simulations per set for the oligarchic initial condition, whereas we had 144 simulations per set for the equal-mass initial condition. The oligarchic initial condition, however, also yields fewer planets per simulation. This is because the initial number of embryos in the oligarchic case is usually fewer than the equal-mass case (comparing the numbers between Table 2.1 and 2.2). We would expect that putting more embryos at the beginning of the simulation would help to form more planets at the end. Yet, this is not the case when we consider the formation of the Mars analogues. Instead, we find that increasing the number of embryos does not help to produce

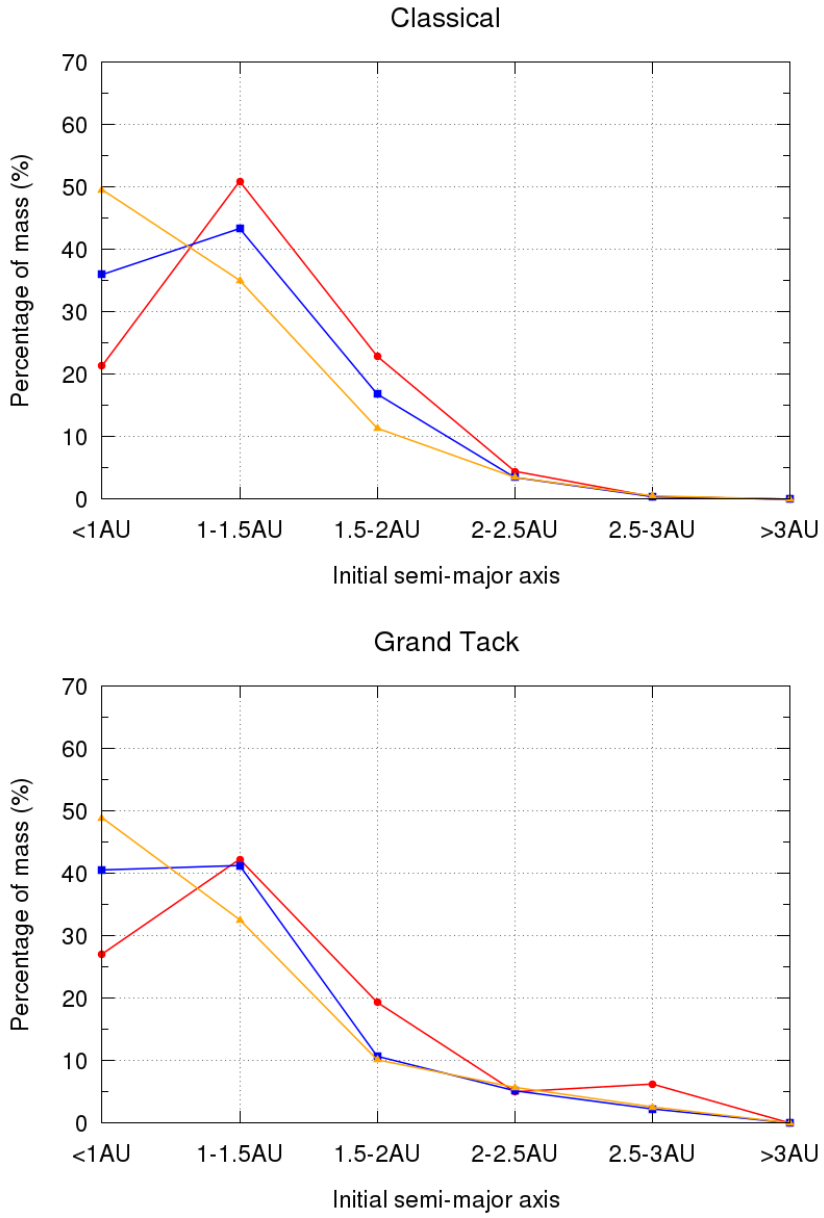

Figure 2.5: Distribution of the initial semi-major axis of all materials incorporated into Venus (orange triangles), Earth (blue squares) and Mars (red points). We relaxed the constraint of the Mars analogues by not considering the mass in the Classical model, which is different from Fig. 2.2. Data for the Grand Tack model are only taken from the equal mass initial conditions.

more Mars analogues. Figure 2.6 shows the total number of Mars analogues in each subset of simulations with equal mass initial condition against the initial number of embryos per simulation (see Table 2.1 for the initial number of embryo adopted for each subset with equal-mass embryos). We have 9 subsets and therefore 9 different initial numbers of embryos: from 27 to 211 embryos. Each subset consists of 32 simulations, in which 16 are simulations with Jupiter's tack location at 1.5 AU and the other 16 are simulations with Jupiter's tack location at 2 AU. We do not observe any systematic increase in the total number of Mars analogues formed with the initial number of embryos. Even if we start the simulations with more than 200 embryos, the total number of Mars analogues generated is less than the simulations with only about 50 embryos. Therefore, there is no correlation between the initial number of embryos and the final number of Mars analogues, which violates our earlier prediction that more embryos at the beginning of simulations would help forming more Mars analogues. We have not been able to find an adequate reason for this behaviour; further study is needed.

2.3.5 Summary of accretion zone analysis

Here we have examined the possibility of forming Earth and Mars with different accretion zones and therefore different bulk compositions in the Classical and the Grand Tack models. We find that simulations in the Classical model fail to form any of the Mars analogues with an accretion zone completely distinct from the Earth analogues ($a_{\rm mwmi} > 2$ AU) when we only consider Mars analogues close to its current mass. Therefore, the Classical model has trouble reproducing the compositional difference between Earth and Mars. It may not be valid, however, to make such a conclusion since we only have eight Mars analogues in

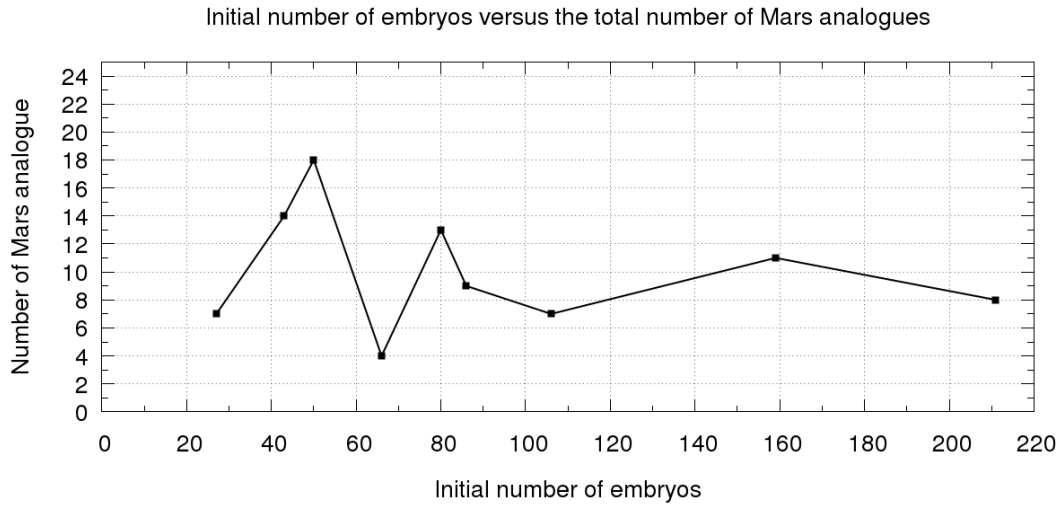

Figure 2.6: The total number of Mars analogues in each subset of simulations as a function of the initial number of embryos per simulation (see Table 2.1) of the Grand Tack model with equal-mass initial condition. The results from simulations with Jupiter's tack location at 1.5 AU and 2 AU are combined.

the Classical model due to fewer numbers of simulations, and its low probability of forming Mars with its current mass. Therefore, we carry out another study comparing the bulk composition of Earth and Mars, presented in the following section (see Sect. 2.4). The Grand Tack model has a slightly higher success rate in producing a compositionally different Earth and Mars because we obtain seven Mars analogues ($< 5\%$) with accretion zones that are wholly distinct from that of the Earth analogues, although statistically the Grand Tack model has a much higher probability to form Earth and Mars with a similar accretion zone. Both the Classical and the Grand Tack models have difficulty forming Earth and Mars with quite different accretion zones that then lead to different bulk compositions.

2.4 Chondrite fractions to make Earth and Mars

In the previous section, we show that it is extremely difficult to form Earth and Mars with totally different accretion zones in both the Classical model and the Grand Tack model. However, forming Earth and Mars with their documented bulk composition may not require them to have a completely distinct feeding zone. In order to further test the two planet formation models, we calculate the bulk composition of Earth and Mars from the output of our N-body simulations, with particular assumption to the initial solid disc.

2.4.1 Disc with a discontinuity in composition

We first assume that the solid disc was initially composed of only enstatite chondrite and ordinary chondrite. We do not consider carbonaceous chondrite in this study since it only takes up a very low percentage of Earth and Mars bulk composition (see Section 1.3). As mentioned in Sect. 1.2 and 1.3, it has been suggested – but not universally accepted – that the solid disc originally had a heliocentric composition gradient consisting of dry, reduced enstatite chondrite close to the Sun, moderately volatile-rich and oxidised ordinary chondrite in the region of the asteroid belt, and highly oxidised and volatile-rich carbonaceous chondrites beyond (Morbidelli et al. 2012; Rubie et al. 2015; Render et al. 2017; Fischer-Gödde & Kleine 2017) (Fig. 1.3) mirroring the heliocentric distribution of asteroid groups (Gradie & Tedesco 1982; DeMeo & Carry 2014). Due to their different water fractions, a plausible reason for the transition from enstatite chondrite to ordinary chondrite is snow line: enstatite chondrite formed within the snow line and ordinary chondrite formed outside the snow line (Desch et al. 2018). However, if this were true then we would also expect the

ordinary chondrites to have as much water as carbonaceous chondrites. One reason that could explain the relatively lower water content of ordinary chondrites is the emergence of Jupiter blocking icy materials from entering the inner Solar System (Morbidelli et al. 2016), where the ordinary chondrites formed.

Although recent studies provide an estimate for the initial location boundary between enstatite and ordinary chondrite (Morbidelli et al. 2012; Fischer-Gödde & Kleine 2017; O'Brien et al. 2018), there is still debate on the exact location for the disc to change its composition. We define this transition location as the break location of the disc. Asteroid 21 Lutetia, which is considered to be a candidate source of the enstatite chondrites (Vernazza et al. 2009; Coradini et al. 2011) is currently located at $\sim$2.4 AU. However, it is possible – and consistent with our Grand Tack simulations – that it formed in the inner Solar System and was subsequently scattered by either emerging protoplanets or by the migration of Jupiter (Vernazza et al. 2011). Therefore, the break location of the disc may be closer to the Sun.

In what follows we employ the simplest two-mode model. We therefore take this break location as a free parameter and assume that it ranges from 1 to 2 AU, with 0.1 AU intervals (i.e. if the break location of the disc is at 1.5 AU, all the planetesimals and embryos initially located within 1.5 AU are made of enstatite chondrite, and those initially located further than 1.5 AU are made of ordinary chondrite). We then make use of the simulation results in Sect. 2.2 to calculate the average percentage of enstatite and ordinary chondrite incorporated into the Earth and Mars analogues for each break location.

Figure 2.7 shows the average percentage of enstatite chondrite (red) and ordinary chondrite (blue) incorporated into the Earth and Mars analogues with different break locations of the disc for both models. We only examine data from

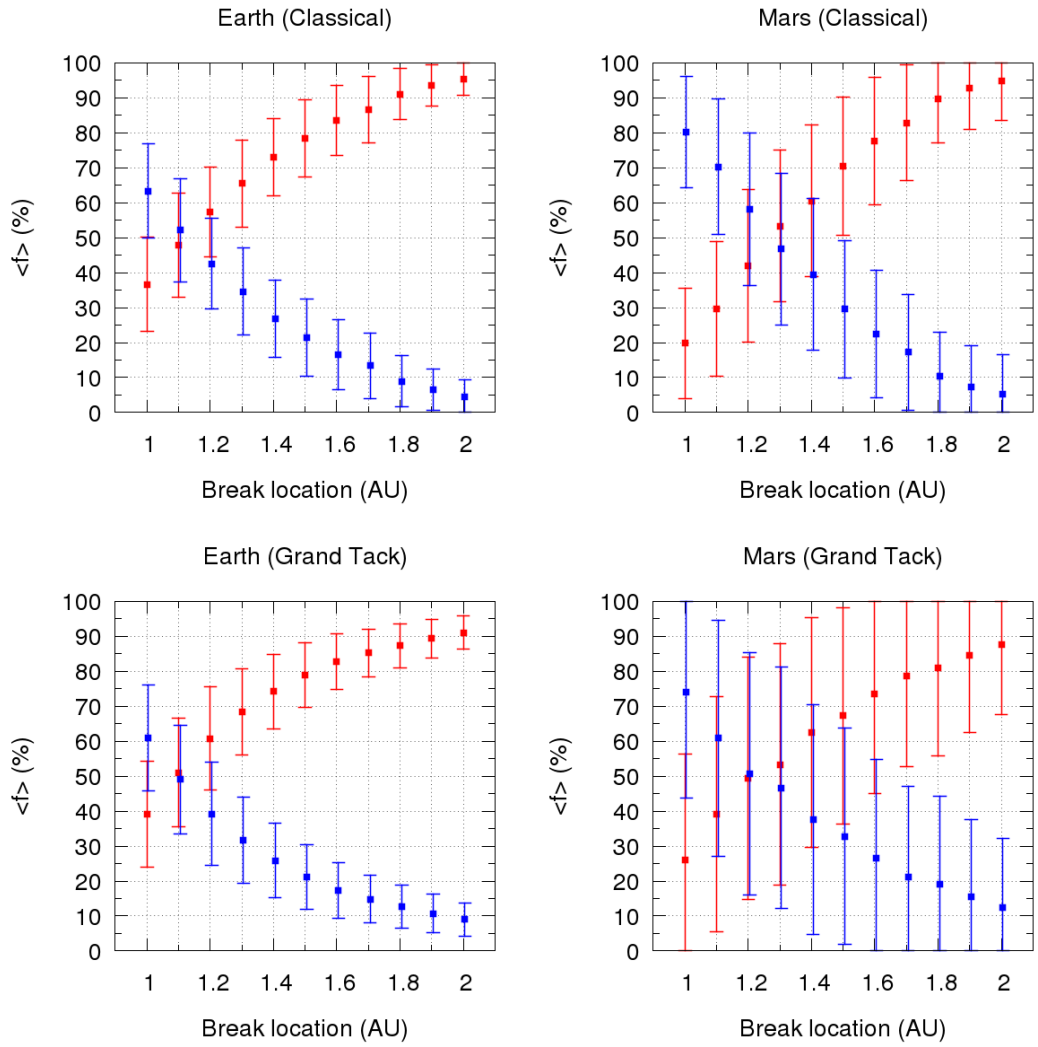

Figure 2.7: The average percentage contribution of enstatite chondrite (red) and ordinary chondrite (blue) to the bulk compositions of Earth and Mars. Data are plotted as a function of the distance where the initial solid disc changes its composition from enstatite chondrite to ordinary chondrite, which is defined as the break location of the disc. The error bars are $\pm 1\sigma$. The two upper panels depict the average composition of Earth and Mars, respectively, in the Classical model simulations. The two lower panels show the results from Grand Tack simulations with equal-mass initial condition, which is similar to Fig. 7 of Brasser et al. (2017).

the simulations with the equal-mass initial condition for the Grand Tack model because the oligarchic initial condition provides similar results in the accretion zone analysis (see Sect. 2.3). We relax the constraints for the Classical model on the Mars analogues by not considering their masses. This ensure that we have enough data for Mars. With a more distant break location, both Earth and Mars consist mainly of enstatite chondrite since the disc consists of more enstatite chondrite. The break location, however, cannot exceed 1.8 AU, otherwise the bulk composition of both Earth and Mars would consist of about 90% enstatite chondrite, which would make them too similar to each other and would also be inconsistent with Mars' suggested bulk composition (Sanloup et al. 1999; Tang & Dauphas 2014; Brasser et al. 2018). Therefore, the key here is whether or not a particular break location exists at which we can reproduce the measured isotopic composition for both Earth and Mars simultaneously. Brasser et al. (2018) reported a best-fit composition of $68\%^{+0}_{-39}$ enstatite chondrite plus $32\%^{+35}_{-0}$ ordinary chondrite for Mars, whereas in previous studies Mars is suggested to be 45% enstatite chondrite and 55% ordinary chondrite, according to Sanloup et al. (1999) and Tang & Dauphas (2014), which is close to 50:50 enstatite to ordinary chondrite ratio. The break location in between 1.1 to 1.5 AU for both models can satisfy the average bulk composition of Mars in Fig. 2.7. Combining this with the most recent results for Earth ($\sim$70% enstatite chondrite and $\sim$25% ordinary chondrite, Dauphas (2017)) leads us to conclude that the break location of the disc should be at 1.3 AU to 1.4 AU in both the Classical and the Grand Tack models.

It is important to note, however, that even if the *average* mean composition of Mars analogues is close to 50:50 when the break location is at 1.3 AU, this result does not simply imply that most of the Mars analogues have such

a composition. The error bars of Mars in Figure 2.7 represent deviations of about ±20% to 30% from the mean values, which suggest that we are dealing with averaging over two extreme cases that happen to meet in the middle. To understand the origin of the large scatter, we plot the cumulative distribution functions (CDFs) of the fraction of enstatite chondrite in the Mars analogues and determine the fraction of them that fall close to the 50:50 mark. Figure 2.8 shows the result of this analysis, where the break location is at 1.3 AU. The left panel shows Mars analogues from the Grand Tack model with equal-mass initial condition, and the right panel plots the CDF for Mars analogues from the Classical model with the oligarchic initial condition. According to Fig. 2.7, the *average* mean composition of Mars in both models is close to 50:50. In the Grand Tack, however, only ∼20% of them fall in the range wherein they possess 29% to 68% enstatite chondrite by mass (Brasser et al. 2018), whereas ∼65% of them do so in the Classical model. Therefore, the Grand Tack model does not work better than the Classical model in producing Mars' documented composition if we neglect the massive Mars problem of the Classical model.

To better understand the origin of Mars' roughly 50:50 composition, we tracked its accretion history. By randomly picking 6 Mars analogues from the Grand Tack simulations and 5 from the Classical simulations, we find that in order to reproduce Mars' suggested composition, 9 out of 11 involve collision between two embryos of different initial composition. Figure 2.9 shows an example of the mass and semi-major axis evolution of a Mars analogue from the Grand Tack simulation. The blue squares represent the initial semi-major axis of the planetesimals and embryos and the time they collided with the Mars analogue. Their sizes are scaled by their masses. In this case, the Mars analogue starts at ∼1.5 AU and is therefore an embryo composed of ordinary chondrite because

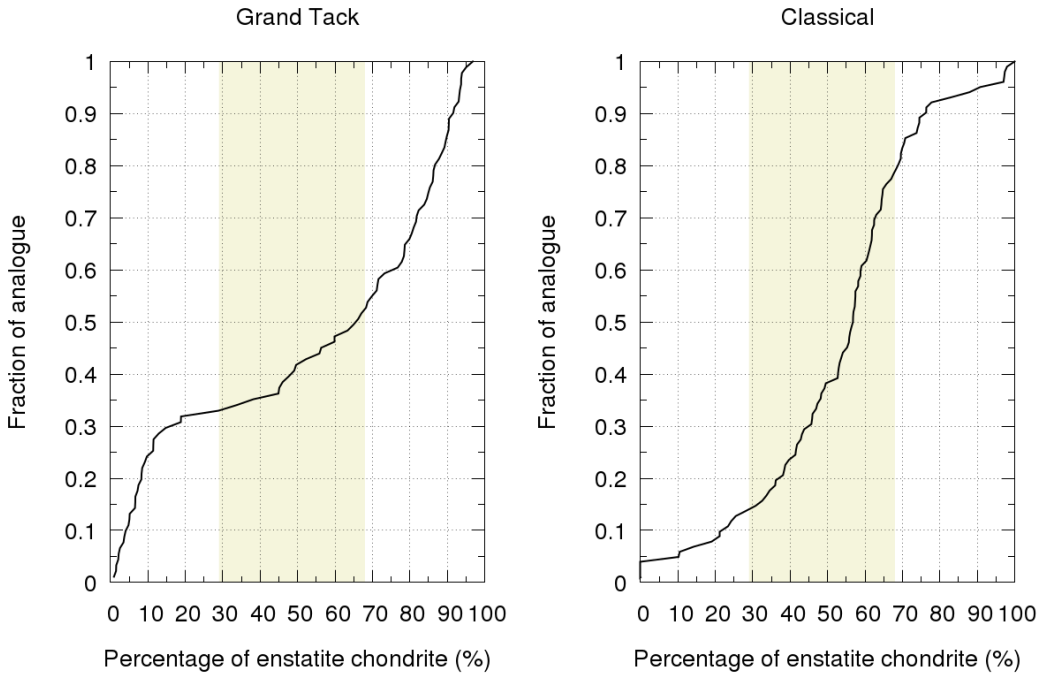

Figure 2.8: The cumulative distribution function of the Mars analogues' final composition (percentage of enstatite chondrite incorporated into each planet) when the break location of the disc is 1.3 AU. The left panel shows results from the Grand Tack simulations with initial equal-mass embryos and the right panel is results from the Classical simulations with initial oligarchic embryos. The beige regions indicate the documented composition of Mars, which is 29 to 68% enstatite chondrite (Brasser et al. 2018).

the break location is at 1.3 AU. It stays near its initial location throughout its whole evolution. Its mass contributed by planetesimals made of enstatite chondrite is comparable to those made of ordinary chondrite: a total of seven of the planetesimals originated from a region further than the break location (squares above the horizontal dotted line at 1.3 AU) and five of the planetesimals started in the inner disc (squares below the horizontal dotted line at 1.3 AU), but they are not enough to increase its mass to the current value. Instead, the major reason for its 50:50 composition is a collision in the simulation at 5.7 Myr with another embryo whose composition is enstatite chondrite. This collision, doubling the mass of the Mars analogue, is represented by a large square at $\sim$1 AU in the lower panel of Fig. 2.9. This particular case agrees with the prediction by Brasser et al. (2017) that Mars formed in a distant region and is therefore initially mainly composed of ordinary chondrite. As pointed out in that work, Mars was then scattered into the inner disc by Jupiter's migration and possibly collided with an embryo mostly made of enstatite chondrite from the inner disc. This scenario naturally explains the isotopic compositional difference between Earth and Mars. Although collisions in N-body simulations occur at random, a colossal impact at 5.7 Myr is entirely consistent with Mars' formation timescale Dauphas & Pourmand (2011).

2.4.2 Completely mixed disc

Our conclusion in Section 2.4.1 is based on the assumption that the initial solid disc is locally homogeneous during the main accretion phase of the planet. Planetesimals in the inner disc are mainly composed of enstatite chondrite and those in the outer disc are mainly composed of ordinary chondrite. The possibility of having a heterogeneous disc during planet formation – that planetesimals in the

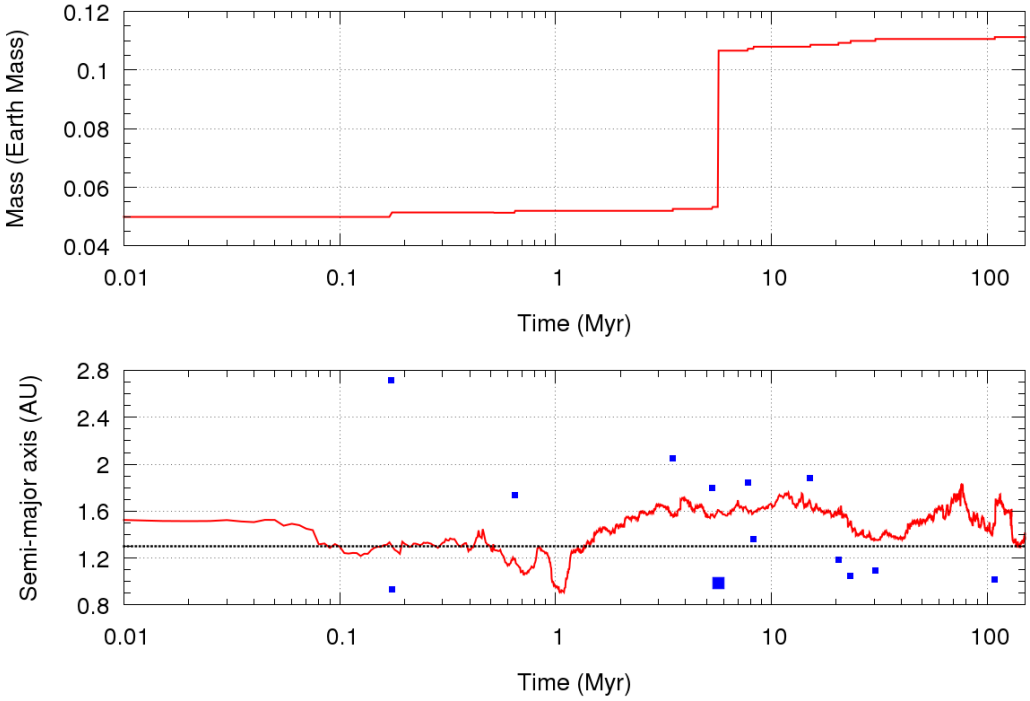

Figure 2.9: The evolution of mass and semi-major axis (red solid lines), respectively, of a Mars analogue with a final 50:50 (50% enstatite chondrite and 50% ordinary chondrite) composition in the Grand Tack simulation with initial equal mass embryos. The blue squares in the lower panel represent the initial semi-major axes and the collision time with the Mars analogue of the planetesimals (smaller squares) and embryos (larger square). The black dotted horizontal line at 1.3 AU in the lower panel is the break location of the initial disc.

same locations of the disc can have wildly different bulk compositions – cannot be entirely ruled out. Thus, could it be possible that the disc was completely mixed and each planetesimal had a random composition when the accretion of planetesimals began?

Here we only analyse data from the Grand Tack simulations with the equal mass initial condition and a tack location of Jupiter at 1.5 AU, and with 10 $R_{\rm Hill}$ initial spacing between embryos for the Classical model (see Sect. 2.2 for simulations' set up). In order to mimic a fully mixed disc in a particular subset of simulations we first assign each planetesimal and embryo a random composition – consisting of a certain percentage of enstatite and ordinary chondrite – by inputting a random number seed. The initial composition of the disc in all runs from the same subset would be made the same by inputting the same number seed. We employ a simple Monte Carlo approach wherein in total we input 11 different number seeds in order to obtain 11 different initial compositions of the disc for that particular subset (see Sect. 2.2 for the classification of subset). We apply the same method to all subsets so as to obtain a vast number of statistics for the final composition of Earth and Mars. Finally, we plot the final composition of all the Earth and Mars analogues from the simulation results in Section 2.2 as CDFs.

Figure 2.10 shows the CDFs for the percentage of enstatite chondrite in the Earth (the two left panels) and the Mars analogues (the two right panels) for both the Classical model (the two upper panels) and the Grand Tack model (the two lower panels). We combine the results from 9 subsets into 3, based on different initial masses of embryos (which are either 0.025, 0.05 or 0.08 $M_{\oplus}$) for the Grand Tack model. The total range of the CDFs increases with initial embryos' masses for both the Earth and Mars analogues because the mass fraction

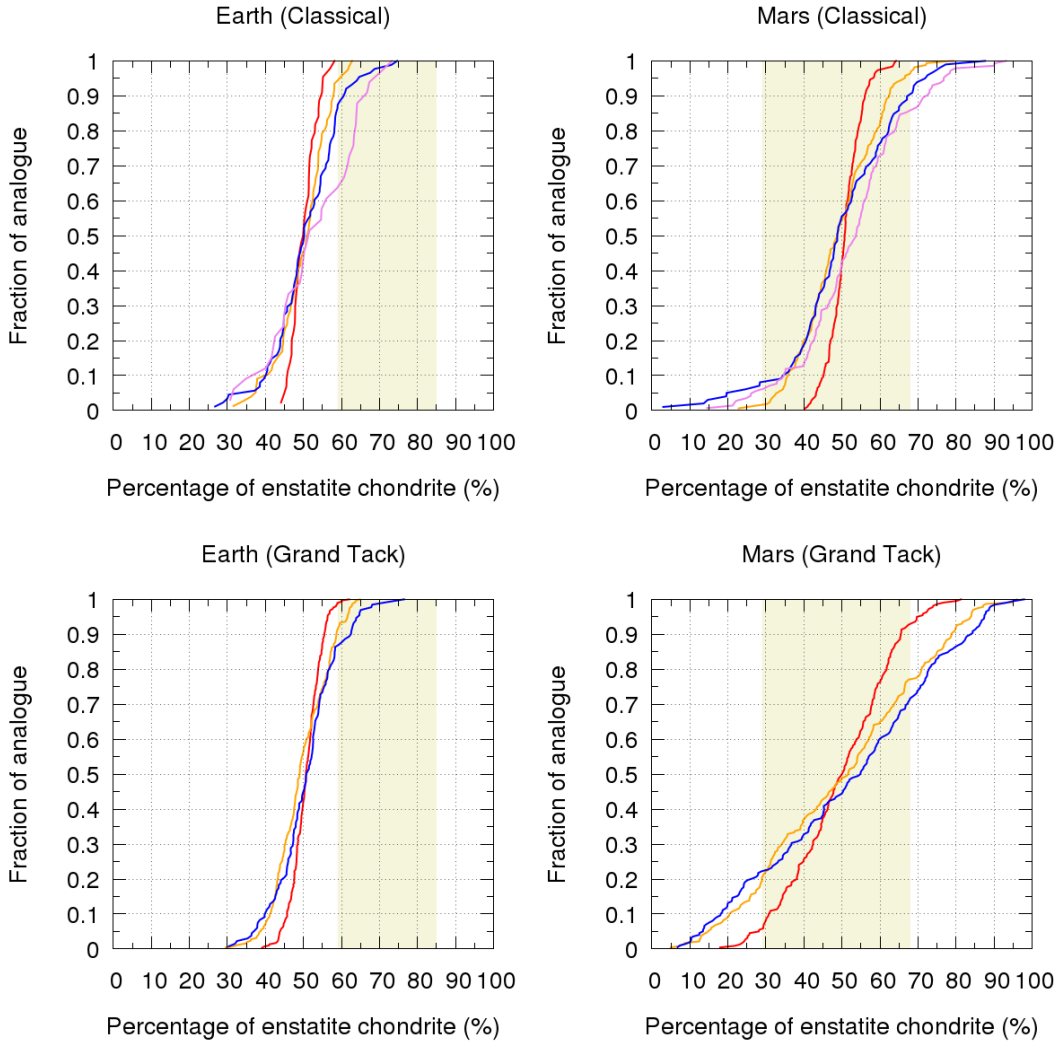

Figure 2.10: The cumulative distribution function for the Earth and Mars analogues' final composition (percentage of enstatite chondrite incorporated into each planet) in a completely mixed disc. The two upper panels show the results from the Classical model with oligarchic initial condition and 10 $R_{\rm Hill}$ initial spacing between embryos. The red, orange, blue and purple lines correspond to the results from 0.5 Myr, 1 Myr, 2 Myr and 3 Myr solid disc, respectively. The two lower panels depict statistics from the simulations of the Grand Tack model with a tack location of 1.5 AU for Jupiter and the equal mass initial condition. The red, orange and blue lines represent results from embryos with initial masses 0.025 $M_{\oplus}$, 0.05 $M_{\oplus}$ and 0.08 $M_{\oplus}$, respectively. The beige regions indicate the documented composition of Earth or Mars, which is 59% to 85% and 29 to 68% enstatite chondrite, respectively (Brasser et al. 2018).

contributed by an embryo is larger for each planet if the embryo has a larger initial mass. In that case, the composition of the planet is highly dependent on the initial composition of the embryos, which is random. The same reason explains why Mars analogues' CDFs have a larger spread than Earth analogues'. We obtain a reasonable fraction of Mars analogues ($> 50\%$ in every subsets) in the Grand Tack model with 29% to 68% of enstatite chondrite. More than 95% of the Earth analogues are composed of less than 70% of enstatite chondrite. This, however, does not match the values derived from recent isotopic studies (Dauphas et al. 2014; Dauphas 2017; Fischer-Gödde & Kleine 2017). Even if we include the uncertainty of the Earth's bulk composition as computed in Brasser et al. (2018) ($71\%^{+14}_{-12}$ of enstatite chondrite), there is only one subset (initial masses of embryos = 0.08 $M_{\oplus}$) in which we have $> 10\%$ chance to obtain the documented composition of Earth.

Results from the Classical model are classified according to the initial disk age (which is either $t = 0.5$, 1, 2 or 3 Myr). As in Section 2.4.1, we relax the constraints on the Mars analogues for the Classical model by only considering their final location but not their final masses. The results we obtained are similar to the Grand Tack model. Although we have a decent probability of getting Mars with 29% to 68% enstatite chondrite (>70% in every subsets), more than 95% of the Earth analogues possess a final composition of less than 70% enstatite chondrite in each group of the simulation. Even though there is one subset ($t = 3$ Myr) in which we have $\sim$35% chance to get Earth with 59% to 85% enstatite chondrite (Brasser et al. 2018), we only have $\leq 10\%$ to do so in the other subsets.

Based on our results, we show that the solid disc is unlikely to be completely mixed when the accretion of planetesimals began in both formation models

because the chance of getting Earth with a high enough percentage of enstatite chondrite is too low (less than 5% in both models). Statisticaly, the completely mixed disc can be ruled out in 2σ level.

2.5 Using dynamics to produce the isotopic composition of Mars

Although the Grand Tack model is not an ideal model to explain the composition of Mars, its success in explaining the mass-distance distribution of the inner Solar System should not be overlooked. Besides, if Mars formed in a distant region, it had to rely on the migration of Jupiter to scatter it to its current location. Therefore, we focus on studying the Grand Tack model instead of the Classical model in this section.

In the previous section, we computed the bulk composition of Mars from a mixture of both enstatite and ordinary chondrite. Even though this mixture agrees with the published results of Brasser et al. (2018), such compositions are computed from the measurements of isotopic anomalies in Mars' mantle. Therefore a comparison between our computed composition of Mars from the dynamical simulations with available martian isotopic anomalies is warranted. Here we are interested not only in the predicted average values of the isotopic composition of Mars that result from the dynamical simulations, but also their uncertainties, and, furthermore, whether these uncertainties are comparable to the measured uncertainties, which may allow for additional insight regarding Mars' origin. Therefore, we proceed to calculate Mars' expected isotopic composition as follows.

The isotopic anomaly is defined here as the deviation of the isotopic composition of a nuclide with respect to the terrestrial standard value. To obtain the correct isotopic composition for both Earth and Mars, the break location of the disc should be around 1.3 AU (see Fig. 2.7). We did not include carbonaceous chondrite in Sect. 2.4 because it only takes up a tiny portion of Earth and Mars according to a few isotopic studies (Sanloup et al. 1999; Warren 2011; Dauphas et al. 2014; Dauphas 2017; Brasser et al. 2018). When calculating the isotopic anomaly, however, the tiny contribution of carbonaceous chondrite may be enough in some cases to cause significant alteration in the value. To address this, we re-estimate the composition of Mars' analogues in this section by assuming the solids initially located further than 3 AU (Jupiter's initial location in the Grand Tack model) are made of carbonaceous chondrite (specifically CO and CV). We multiply the mass of each planetesimal further than 3 AU by ten since we have a relatively low-mass outer disc in the simulations. The isotopic composition of an element in Mars' mantle $\varepsilon_{\rm Mars}$ can be calculated by

$$\varepsilon_{\rm Mars} = \frac{\sum_i f_i c_i \varepsilon_i}{\sum_i c_i \varepsilon_i}, \tag{2.4}$$

where f_i is the percentage of chondrite type i in Mars (i is either enstatite, ordinary, or carbonaceous chondrite), c_i is the concentration of the element in chondrite type i and ε_i is the isotopic composition of the element in chondrite type i (Dauphas 2017). The mean composition of Mars computed from the Grand Tack N-body simulations ($\pm 1\sigma$) is $53\%^{+34}_{-34}$ enstatite chondrite, $47\%^{+35}_{-35}$ ordinary chondrite and $0.2\%^{+4.7}_{-0.2}$ carbonaceous chondrite if the break location of the disc is at 1.3 AU (see Fig. 2.7). The large uncertainties in $\varepsilon_{\rm Mars}$ are the result of the great potential for variety in Mars' dynamical history (i.e. uncertainities in f_i), and in the uncertainities in ε_i for each chondritic source.

Therefore, a Monte Carlo method is adopted to calculate $\varepsilon_{\mathrm{Mars}}$ for each element. We pick the f_i from our dynamcial simulations and ε_i from measured values listed in Dauphas (2017). We use the Box-Mueller transform to approximate a standard normal distribution and then calculate the corresponding $\varepsilon_{\mathrm{Mars}}$ from this distribution. We repeat this 60000 times and obtain a list of values for $\varepsilon_{\mathrm{Mars}}$ of an element. The mean and the 2σ standard deviation of $\varepsilon_{\mathrm{Mars}}$ of each elements is then calculated with this list of values. Our work is different from Brasser et al. (2018) since we adopt the composition of Mars from our dynamical simulation, whereas the results of Brasser et al. (2018) are based on a Monte Carlo Mixing model using the measured isotopic values of the chondrites and Mars as input.

Table 2.4 shows the average $\varepsilon_{\mathrm{Mars}}$ and the 2σ uncertainty of each element. We compare the values that we calculated and those measured in different studies and summarised by Dauphas (2017). The measured value for μ^{142}Nd is the mean value of enriched shergottites in Kruijer et al. (2017). We adopt the same computed value as Brasser et al. (2018) for ε^{64}Ni, where they rely on existing ε^{62}Ni isotope data for Mars and the correlation between ε^{64}Ni and ε^{62}Ni (Tang & Dauphas 2014) because the ε^{64}Ni of the martian mantle has not been measured precisely. We observe that all the elements fit within the 2σ uncertainties of the measured values. For most elements, the computed isotopic uncertainties resulting from dynamics are comparable to the measured values. Oxygen (O), Titanium (Ti), and Neodymium (Nd) are lithophile elements and therefore would remain in the mantle since throughtout accretion (Dauphas 2017). Chromium is moderately siderophile (e.g. Righter & Chabot 2011). A portion of accreted Cr in the mantle sank into the core during the formation of Mars. This may alter the $\varepsilon_{\mathrm{Mars}}$ that we calculated from the full accretion of

Table 2.4: Comparison between the calculated and the average measured isotopic composition ($\varepsilon_{\mathrm{Mars}}$) from Dauphas (2017) for Δ^{17}O, ε^{50}Ti, ε^{54}Cr and ε^{92}Mo, Kruijer et al. (2017) for μ^{142}Nd and Brasser et al. (2018) for ε^{64}Ni of Mars mantle. The isotopic anomaly of these elements is calculated from a break location of the disc at 1.3 AU in the Grand Tack model. Carbonaceous chondrite is also included in the calculation (see the text Sect. 2.5 for details). The uncertainties of the calculated values and the average measured values are 2σ.

	Δ^{17}O	$\pm$	ε^{50}Ti	$\pm$	ε^{54}Cr	$\pm$
Calculated	0.43	0.33	-0.37	0.21	-0.14	0.13
Measured	0.27	0.03	-0.54	0.17	-0.19	0.04
	μ^{142}Nd	$\pm$	ε^{64}Ni	$\pm$	ε^{92}Mo	$\pm$
Calculated	-12.5	2.6	-0.07	0.11	0.63	0.21
Measured	-16	8	0.10	0.28	0.20	0.53

Mars. Nevertheless, the portion of Cr that sank into the core during Earth's formation is much lower than other moderately siderophile (e.g. Ni and Mo) (Dauphas 2017). For simplicity, we treat Cr behaviour in Mars in a similar manner to that in Earth.

We adopt a different method in calculating the $\varepsilon_{\mathrm{Mars}}$ for ^{64}Ni and ^{92}Mo. Both Ni and Mo are moderately siderophile elements and behave more like siderophiles than Cr. It is probable that a significant portion of accreted Ni and Mo sank into the core throughout the accretion of Mars. Dauphas (2017) showed that nearly all the Ni and Mo accreted in the first stage of Earth's accretion should have sunk into the core. The first stage of Earth's accretion is defined as the first 60% of Earth's accretion in terms of mass because previous models suggested that material accreted by Earth changed from more reduced to more oxidised at about 60% accretion (Rubie et al. 2015). It is expected that Ni and Mo should behave similarly in Mars. For Ni and Mo, we ignore

all accretion during the first ∼60% of Mars' accretion. This requires a higher resolution of the late-stage accretion data for each Mars analogue, which our simulations lack. Therefore, we can only pick the data from simulations with smaller initial embryo mass (0.025 $M_{\oplus}$) since these have the highest initial number of embryos. The average percentage of enstatite, ordinary chondrite, and carbonaceous chondrite is calculated for 20 Mars analogues from their last ∼40% of accretion. The $\varepsilon_{\rm Mars}$ value of ^{64}Ni and ^{92}Mo are calculated with the same Monte Carlo method described above (Eq. (2.4)), but with the f_i obtained from the last ∼40% of accretion. The mean bulk composition ($\pm 1\sigma$) from N-body simulations for the last ∼40% of Mars' accretion when the break location of the disk is at 1.3 AU is $41\%^{+23}_{-23}$ enstatite chondrite, $58\%^{+24}_{-24}$ ordinary chondrite, and $0.8\%^{+3.6}_{-0.8}$ carbonaceous chondrite. Table 2.4 shows that the calculated values match with the measured values for both Ni and Mo.

To summarise, it is possible to reproduce the isotopic composition of the martian mantle for six isotopes from our simulations with the Grand Tack model. The uncertainties of the martian isotopic composition calculated from the N-body simulations for 4 out of 6 elements are of the same order of magnitude as the measured data. This is caused mainly by the great variety of Mars' dynamical evolution in our N-body simulations. Therefore, to better constrain the outcome, more high-resolution simulations are needed. We also encourage improved measurements of the isotopic composition of martian meteorites to lower the measured uncertainties (see Ch. 4 for further discussion).

2.6 Conclusions

The isotopic anomalies in several elements suggests that the bulk compositions of Earth and Mars are different. Assuming they both accreted mainly chondritic material, Earth should have inherited mainly enstatite chondrite (∼70%) (Dauphas 2017; Brasser et al. 2018) and Mars is likely to have accreted more ordinary chondrite (32% to 67%) (Brasser et al. 2018) than Earth. This provides further support to the conclusion that the region where Mars accreted most of its mass was different from that of Earth, and was likely to have been more distant (Brasser et al. 2017). We first examine the possibility of forming Earth and Mars with different accretion zones in two different terrestrial planet formation models: the Grand Tack model (Walsh et al. 2011) and the Classical model (e.g. Chambers 2001)(Sect. 2.3). By tracing the initial positions of the planetesimals and embryos assembled into each planet, an accretion zone comparison can be made between the Earth and Mars analogues after performing a large number of N-body simulations. Our initial conditions are either embryos with equal masses or with masses that were computed from the traditional oligarchic growth of the planetesimals (Kokubo & Ida 1998). We find that there are seven Mars analogues with $a_{\rm mwmi} > 2$ AU in the Grand Tack simulations. These are Mars analogues that have a completely different accretion zone and hence likely different bulk composition from all the Earth analogues. However, they only contribute $< 5\%$ of the total Mars analogues. We discovered no Mars analogues with $a_{\rm mwmi} > 2$ AU in the Classical model when we considered the massive Mars problem generally observed in the Classical model's simulations. Both the Classical and Grand Tack have difficulty in forming Earth and Mars with completely different accretion zones. We also find that the final number of Mars analogues we obtain from the simulations is independent of the initial

number of embryos, which violates our original expectation that more initial embryos yield more Mars analogues.

We then estimated the average percentage of enstatite chondrite and ordinary chondrite incorporated into Earth and Mars based on the N-body simulation results (Sect. 2.4). At first we assumed that the solid disc is made entirely of enstatite and ordinary chondrite, with enstatite chondrite residing in the inner region and ordinary chondrite in the outer region. The break location of the disc, at which the disc changes from enstatite chondrite to ordinary chondrite, is set as a free parameter from 1 to 2 AU with 0.1 AU intervals (Sect. 2.4.1). Our results show that the break location must be close to 1.3 AU for both models to possess mean compositions of Earth and Mars close to the documented ones. At this break location, the Classical model yields more Mars analogues close to Mars' documented composition than the Grand Tack model if we neglect the problem of excessive mass of Mars in the Classical model. This composition requires an early collision between two embryos of different composition that merge together to form Mars, which agrees with the distant Mars formation scenario (Brasser et al. 2017). We also test the case with a completely mixed disc by assuming random initial composition for each planetesimal and embryo in the disc. Although we obtain a decent probability of getting Mars with documented composition, the probability of getting Earth's $\sim$70% enstatite chondrite is $<$ 10% in most cases (Sect. 2.4.2). Therefore, we conclude that the disc is unlikely to have been completely mixed during the late stage of planet formation.

In the previous section, we calculated the isotopic composition from our simulation results for four elements that trace the full accretion history of Mars (^{17}O, ^{50}Ti, ^{54}Cr and ^{142}Nd) and two elements that trace only the late accretion (about the last 40 wt%) of Mars (^{64}Ni and ^{92}Mo) in the case of the break location

of the disc at 1.3 AU, in which Mars is ∼50% enstatite chondrite and ∼50% ordinary chondrite. The Grand Tack model matches the measured values within their uncertainties for all elements. Nevertheless, at the present time we cannot confine the dynamical pathway of Mars by matching the calculated isotopic composition to the measured values since their uncertainties are comparable to each other. Future improvements on numerical and isotopic data are required in order to solve the origin of Mars (see Ch. 4 for further discussion).

Chapter 3

Implication of the Late Veneer Colossal impact on Mars

3.1 Objectives and outline of this chapter

In order to understand how the Late Veneer (LV) colossal impact delivers highly siderophile elements (HSEs) into the martian mantle and whether a hydrogen atmosphere could be formed after the LV giant impact, we performed hydrodynamic simulations to study the effect of this impact, under the assumption that either an early hydrosphere or cryosphere existed on the early Mars (see Sect. 1.4 for the background). In the next section, we first describe the method and the initial conditions we adopted for the hydrodynamic simulations between Mars and a Ceres-sized impactor. The collision outcomes of the hydrodynamic simulations are presented in Sect. 3.3. In Sect. 3.4 , the size of the impactor's iron fragments after giant impact are estimated from the simulation results and an analytical method. Following the reaction between iron fragments and the

surface water reservoir on the early Mars, the amount and life time of the reaction product - hydrogen - is calculated in Sect. 3.5. In Sect. 3.6, We discuss the possible factors affecting the life time of a hydrogen atmosphere and the meteoritic evidence we have for an early atmospheric escape event on Mars. We conclude the findings in the last section of this chapter. Studies in this chapter are performed under collaboration with Prof. Hidenori Genda (Earth-Life Science Institute), Prof. Ramon Brasser (Earth-Life Science Institute) and Prof. Stephen Mojzsis (University of Colorado Boulder). Most of the corresponding results are accepted to publish in Icarus.

3.2 Method

We adopt the smoothed particle hydrodynamics (SPH) method (e.g. Monaghan 1992) to simulate the LV giant impact. SPH is a flexible Lagrangian approach for solving hydrodynamic equations. The basic idea of the SPH method is to divide a system into many numbers of particles (SPH particles) and each particle interact with its neighbour particles through pressure gradient force and mutual gravity. Our numerical code is identical to that used in Genda et al. (2012, 2015, 2017a). Please refer to Appendix B for the detail of the code.

Here we briefly describe the initial conditions of our SPH simulations. We consider a $\sim$1000 km diameter impactor striking Mars at different impact angles, θ, and impact velocities, $v_{\rm imp}$. We propose that this object be named *Nerio*. She was Mars' consort, an ancient war goddess, and the personification of courage. She was the partner of Mars in ancient cult practices. Relative to the horizontal reference frame, 8 simulations were performed with $\theta = 0^{\rm o}$ (a head-on collision), $30^{\rm o}$, $35^{\rm o}$, $40^{\rm o}$, $45^{\rm o}$ (statistically most-likely; Shoemaker (1962)), $50^{\rm o}$, $55^{\rm o}$ and

60°. We set $v_{\rm imp} = 10$ km/s ($\sim$2 $v_{\rm esc}$, where $v_{\rm esc} \sim 5$ km/s is the surface escape velocity of Mars) which is the mean value obtained from N-body simulations of leftover planetesimals from terrestrial planet formation (Brasser et al. 2016b). We also perform three additional simulations with $v_{\rm imp} = 7$ km/s ($\sim$1.4 $v_{\rm esc}$), 13 km/s ($\sim$2.6 $v_{\rm esc}$) and 16 km/s ($\sim$3.2 $v_{\rm esc}$), but restrict these to $\theta = 45°$. The mass of the target (Mars) is set to 6.4×10^{23} kg and the impactor (Nerio) is $\sim$0.3 wt% of Mars (2.0×10^{20} kg). The number of SPH particles used for the target and impact are 3 million and 9600 particles, respectively. Both objects are assumed to be completely differentiated: they have a chondritic initial composition with a 30 wt% iron core and a 70 wt% silicate mantle.

Based on the relative abundances of the highly siderophile elements (HSEs) as measured in terrestrial mantle-derived rocks, Earth's LV augmentation is suggested to consist of mainly enstatite chondritic material (Fischer-Gödde & Kleine 2017). Current isotopic studies coupled with dynamical analysis performed to study the origin of Mars provide no meaningful limitation on the composition of its LV impactor (Brasser et al. 2018). Hence, we follow the approach of Genda et al. (2017a) and consider a bulk composition of enstatite chondrite with 30 wt% of its mass as reduced iron sequestered in its core (Wasson & Kallemeyn 1988). We ignore the spin effect for pre-impact objects. The surface velocity of a Nerio-scale spinning impactor and target Mars is much lower than the impact velocity (Genda et al. 2017a; Canup 2008). The initial internal energy is assumed to be 1×10^5 J/kg (Genda et al. 2017a), and we calculate vibrations of the impactor and target until the particle velocity becomes slower than 100 m/s; this value is much lower than the impact velocity. We subsequently use these relaxed bodies for impact simulation. The calculated diameter of the gravitationally relaxed impactor is 1040 km. We performed the

impact simulations over a period of 10^5 sec, or about 28 hours.

3.3 Collision Outcome

Snapshots of our SPH simulations for a collision between a Nerio-sized impactor and Mars are shown in Fig. 3.1. The collision results are broadly similar to those reported in Genda et al. (2017a), where a colossal impact was considered between Earth and a 3000 km diameter object with $\sim$0.01 $M_\oplus$. Fig. 3.1(a) shows the time series of snapshots for the most likely case of $v_{\rm imp}$ = 10 km/s ($\sim$2 $v_{\rm esc}$) and $\theta = 45^{\rm o}$. After the initial collision with Mars, the impactor undergoes elongation due to the mechanical tearing of both its core and mantle; a significant amount of the impactor's material is ejected into martian orbit from the collision site. A minority fraction of the ejected materials gain enough kinetic energy during the collision to escape from Mars' gravity. The majority of the ejecta re-accrete back to Mars and blanket its entire surface, with the highest portion being re-accreted onto the surface close to the collision site. A portion of the ejected impactor's materials are shocked after impact and then further fragment into smaller pieces from pressure release. Iron core material of the impactor experiencing fragmentation is shown as yellow particles in Fig. 3.1. This material pollutes the mantle of Mars with HSEs by re-accreting back onto the whole surface of Mars.

Fig. 3.2 depicts the number of fragmented impactor's iron particles that are finally embedded in the martian mantle after 5.58 hr as a function of longitude for an impact angle of $\theta = 45^{\rm o}$ and $v_{\rm imp}$ = 10 km/s. We note that the distribution of fragments is global but non-uniform, with fragments concentrated near the expected impact side (from $-50^{\rm o}$ to $50^{\rm o}$ from the negative y-axis). Our

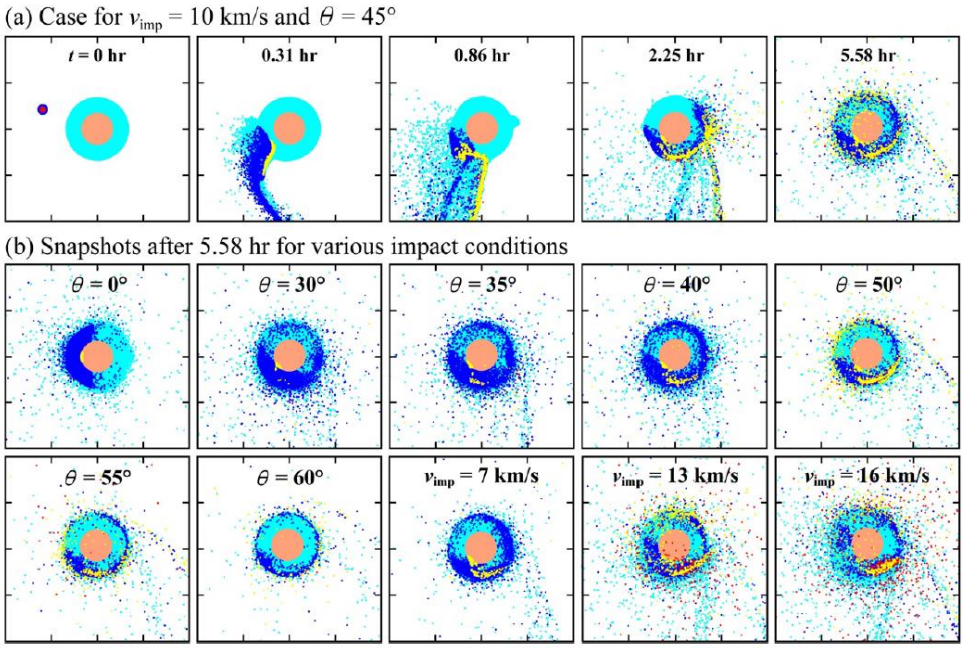

Figure 3.1: A Snapshots of a collision of a Nerio-scale impactor (∼0.3% of Mars' mass) onto the early Mars. (a) The time series of snapshots for the case of the impact velocity, $v_{\rm imp}$ = 10 km/s (∼2 $v_{\rm esc}$, where $v_{\rm esc}$ is the surface escape velocity of Mars) and the impact angle, θ = 45°. (b) Snapshots after 5.58 hr for various θ ranging from 0° to 60° with $v_{\rm imp}$ = 10 km/s, and variorus $v_{\rm imp}$ ranging from 7 km/s to 16 km/s with θ = 45°. Mantle and core materials for the impactor are coloured blue and red, respectively, and those for Mars are light blue and orange. Impactor's core materials that have experienced fragmentation are coloured yellow (See the text in Sect. 3.3 for details). The snapshots are NOT cross sections, but all SPH particles are layered on top of one another in the order of martian mantle, impactor's mantle, martian core, impactor's core (red and then yellow), so that iron particles are clearly seen. The interval of tics in each snapshot is 5000 km (1.47 martian radii).

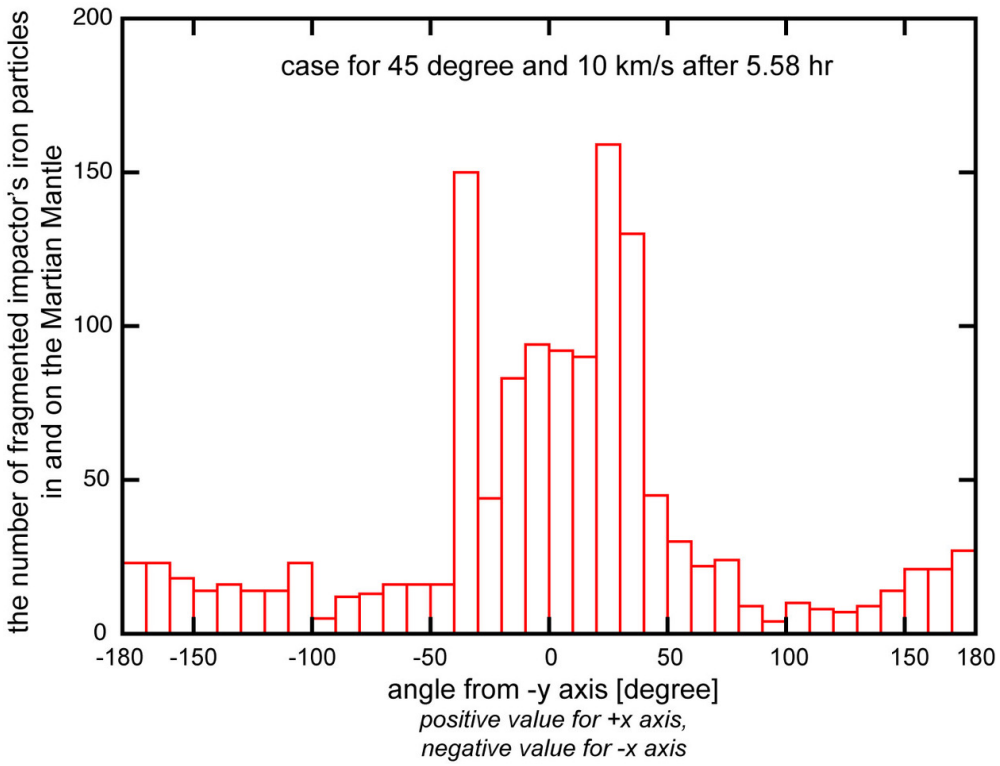

Figure 3.2: The number of fragmented impactor's iron particles in and on the martian mantle at different longitude from the negative y axis for impact angle, $\theta = 45^{\circ}$ and impact velocity, $v_{\rm imp} = 10$ km/s ($\sim 2\ v_{\rm esc}$) after 5.58 hr. The centre of the axes is at the centre of Mars. The distribution of fragments are global but concentrated from -50° to 50°, which is the impact side.

results are similar to Marchi et al. (2018), which shows that material from large planetesimals ($\geq$ 1500 km) is concentrated within localized domains of Earth's mantle after colliding with Earth during the post-Moon formation period. This could explain the observed ε^{182}W isotopic anomalies in terrestrial rocks due to incomplete mixing (Willbold et al. 2015). On billion-year timescales the distribution of HSEs could possibly be homogenised by martian mantle convection although oxygen isotopic heterogeneity has been observed from the martian meteorites (Agee et al. 2013).

Snapshots of our impact simulations with other values of θ and $v_{\rm imp}$ are given in Fig. 3.1(b). The collision outcome strongly resembles Genda et al. (2017a) for the case of the Earth's collision with its LV impactor *Moneta* and so we limit the results to 5.58 hr from the start of the simulations. In the $\theta = 0^{\rm o}$ scenario (head-on collision), the core of the impactor merges with the martian core rapidly and nearly all of the impactor's mantle material is confined – initially – to one hemisphere of Mars' mantle. Fragmentation of the impactor's iron core material is relatively difficult in head-on collisions since no SPH particles from that region are ejected to experience pressure release. The efficiency of HSEs delivery is very low because almost none of the impactor's core material remains in the martian mantle. Nearly all of the impactor's iron materials sink to the core of Mars.

Collision outcomes of $\theta = 30^{\rm o}$, $35^{\rm o}$ and $40^{\rm o}$ are similar to one another. We find that most of the impactor's mantle ($> 70\%$) and all core materials are gravitationally bound to Mars when $\theta < 40^{\rm o}$. Compared to the nominal $\theta = 45^{\rm o}$ case, we observe that far fewer tracer particles for the fragmented impactor's core (yellow) in our SPH code exist in the martian mantle. Therefore, the delivery of HSEs is not efficient when $\theta \leq 40^{\rm o}$. More fragmented impactor

core particles (yellow) exist in the martian mantle when the $\theta = 50^{o}$ compared to the other lower θ cases. The total number of the bound impactor's SPH particles (the total number of blue, red and yellow SPH particles in the martian mantle) is, however, lower in the $\theta = 50^{o}$ scenario. An increase of θ up to 55^{o} and 60^{o} yields even fewer bound impactor's materials. This is because the collision becomes nearly hit-and-run. Therefore the impactor only grazes the martian surface when θ is high. Hence a higher portion of the impactor's materials escapes from Mars permanently. Therefore, when $\theta > 50^{o}$ the collision is basically a hit-and-run with the impactor's core and mantle strewn beyond Mars into the mid-Solar system.

The relation between the amount of impactor's materials bound to Mars and θ is provided in Fig. 3.3. The left panel depicts the mass fraction of the impactor's rocky mantle that became bound to Mars after collisions as a function of θ; the right panel depicts the same for the impactor's iron core. The trend of decreasing mass fraction of the bound impactor's materials with increasing θ is clear. Moreover, for the same θ, the mass fraction of the bound impactor's iron core is usually higher than that of the bound impactor's mantle. Since the iron core is enveloped by the mantle, it is therefore more difficult for the iron core to escape Mars' gravity (e.g. Genda et al. 2017a). The shaded regions in the right panel of Fig. 3.3 represent iron core materials of the impactor that (1) experience fragmentation and (2) are eventaully embedded in the martian mantle (both criteria have to be fulfilled); these materials are represented by the yellow particles staying in the martian mantle or floating near the martian surface in Fig. 3.1. The shaded region increases with θ because a higher fraction of shocked iron core materials are ejected and then undergo pressure release when θ is larger. The maximum mass of bound fragments is reached at $\theta =$

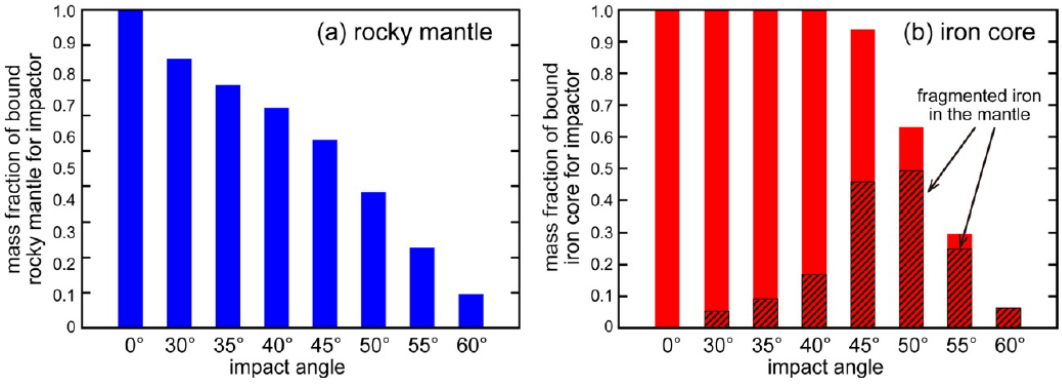

Figure 3.3: Mass fraction of impactor's materials that are gravitationally bound to Mars after collisions as a function of impact angle, θ. The impact velocity, $v_{\rm imp}$, is the same for all θ (10 km/s, $\sim$2 $v_{\rm esc}$). The left panel pertains to the impactor's silicate mantle material, while the right panel is for the iron core. Some of the impactor's core materials that are gravitationally bound to Mars experience pressure release after the shock, which leads to fragmentation (See the text in Sect. 3.3 and 3.4 for details). Shaded region represents the mass fraction of fragmented impactor's iron materials that do not merge into the martian core, but are available for suspension in the martian mantle.

50°. Also, a higher fraction of fragmented iron of the impactor sink to the core instead of staying in the martian mantle when θ is smaller. The shaded region subsequently decreases with θ from $\theta = 50°$ to 60° because most of the fragmented iron core of the impactor escapes from the system instead of becoming embedded in the martian mantle. We do not discuss the fate of the non-fragmented impactor's iron because at most $\sim$3% of the impactor's core particles stay in the martian mantle as non-fragmented iron for each θ case. Hence, non-fragmented iron would not contribute much to the delivery of HSEs into the martian mantle and the subsequent formation of a hydrogen atmosphere (see Sect 3.5).

We also perform additional simulations with different $v_{\rm imp}$ (but only for $\theta = 45°$); their snapshots are shown in Fig. 3.1(b). The total number of

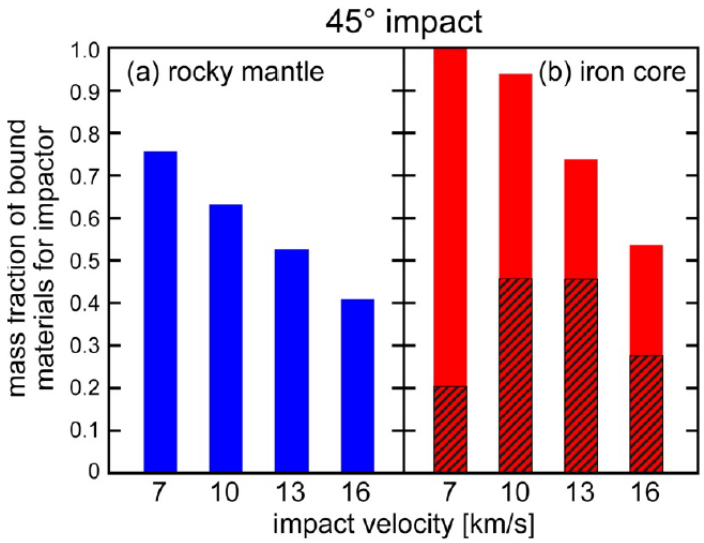

Figure 3.4: Same as Fig. 3.3, but the dependence of the impact velocity, $v_{\rm imp}$, is shown. The impact angle, θ, is fixed to be 45°.

the impactor's SPH particles (blue, red and yellow) that are embedded in the martian mantle decreases with increasing $v_{\rm imp}$. Fig. 3.4 shows this further when we investigate the mass fraction of bound materials for the impactors' mantle and iron core as a function of $v_{\rm imp}$. Results in the left panel are explained by the impactor's materials having a higher kinetic energy when $v_{\rm imp}$ is higher and are thus more likely to escape Mars' gravity. We also found that the fragmented impactor core (yellow particles) exists with the highest abundance when $v_{\rm imp}$ = 10 km/s or 13 km/s: nearly half of the fragmented impactor's iron core finally ends up suspended in the martian mantle when $v_{\rm imp}$ = 10 km/s or 13 km/s (Fig. 3.4). This fraction drops to $< 30\%$ when v

In summary, in the impact geometry that is statistically most likely (θ = 40° – 50° and $v_{\rm imp}$ = 10 – 13 km/s), our simulations inject a substantial amount of fragmented iron (∼50% of the impactor's iron core) into the mantle of Mars. The efficiency of HSEs' delivery to the martian mantle dramatically decreases

when $\theta \leq 40^{o}$ since less than 20% of the impactor's iron core materials are fragmented and finally suspended in the martian mantle. Similar to the low θ case, high θ cases ($\theta \geq 55^{o}$) also do not favor HSEs delivery since most of the impactor's core materials ($> 70\%$) escape from the system after the giant impact.

3.4 Fragments' size estimation after the colossal impact

In the common oblique collision ($\theta \sim 45^{o}$) scenario, the shock wave generated during the collision passes through the impactor's iron core and hence creates a high peak pressure ($\sim$100 GPa) within it; this high peak pressure, however, is below the pressure for shock-induced incipient melting ($\sim$220 GPa) and complete melting ($\sim$260 GPa) for cold iron (Melosh 1989). However, we note that some studies propose that such small cores could exist for a Nerio-like object and can remain molten up to $\sim$100 Myr after the formation of the Calciumaluminium-rich inclusion (e.g. Neumann et al. 2014), which is the first solid to condense in the solar nebular (Bouvier & Wadhwa 2010). At the very least, the impactor's core should be in a hot solid state, in which case re-melting of the iron core by shock passage ($\sim$100 GPa) is expected. Hence, we assume here that the impactor's core is liquid just after the impact. The molten iron core can thus be pulled apart into an elongated shape and ejected from the near-surface region of target Mars under the dynamical physical conditions we find in our model. After ejection into open space, the iron core material expands due to its high residual internal pressure. This state induces shear stress on the molten core material and results in its fragmentation.

Due to the computationally intensive nature of the high resolution simulations required to directly analyse the fragmentation process, we instead traced the time-dependent evolution of pressure for all SPH particles in our simulations. The expansion of core material from residual internal pressure drops from shock-induced pressure (∼100 GPa) to extremely low pressure (∼0 GPa). We assume that fragmentation occurs when the pressure of a shocked SPH particle decreases down to 0.1 MPa (1 bar) during the pressure release process (see Genda et al. 2017a). Our tracked SPH particles of the impactor's core that suffer pressure release are shown as yellow in Fig. 3.1; their mass fractions that are eventually embedded in the martian mantle are indicated by shaded regions in Fig. 3.3(b) and 3.4(b) (see the previous section).

The size of the iron fragments, however, cannot be directly computed from the SPH simulations due to limitations of our model resolution and computational feasibility. The dimensions of a single SPH particle is expected to far exceed that of the iron fragments. We thus estimate the fragment size by considering the balance between the surface tension of liquid iron, σ, and the local kinetic energy ($1/2\ mv^2$) induced by the local shear velocity $v = \dot{\varepsilon}d$, where $\dot{\varepsilon}$ is the strain rate, which describes the rate of deformation of the expanding molten iron blob (see Appendix C for the method of calculating the strain rate), and d is the typical size of molten droplets at fragmentation. The size of the molten iron droplets ejected by an impact is

$$d = (\frac{40\sigma}{\rho\dot{\varepsilon}^2})^{1/3} \tag{3.1}$$

(Melosh & Vickery 1991), in which $\rho = 7000$ kg/m^3 is the density of the iron droplets while $\sigma = 2$ N/m for liquid iron (Keene 1993). The $\dot{\varepsilon}$ tensor for each SPH particles can be computed in the SPH code by the method described in

Appendix C.

Fig. 3.5 shows the distribution of the strain rate, $\dot{\varepsilon}$, for the impactor's core material at the time of fragmentation. The calculated strain rate is ∼0.001 – 0.03 s^{-1}, which is consistent with the value estimated by the following simple physical consideration: $\dot{\varepsilon} \sim v_{\rm imp}/D_{\rm imp} = 0.01$ s^{-1} (Melosh & Vickery 1991), where $v_{\rm imp} = 10$ km/s and $D_{\rm imp} = 1040$ km, which is the impactor's diameter in our simulation. The size of the iron fragments can be estimated from Eq. (3.1), which is shown in Fig. 3.5. The peak of the green curve indicates that most of the fragments have a size of ∼14 m when $\theta = 30^{\rm o}$. Increasing θ to 45° and 60° results in an even smaller fragment size. The peak of the red curve ($\theta = 45^{\rm o}$) and the blue curve ($\theta = 60^{\rm o}$) are ∼10 m and ∼6 m, respectively. Since the impactor suffers a greater extent of elongation with a larger θ collision, the iron core material of the impactor experiences a faster change in strain. Although with larger θ the mass fraction of the impactor's iron core that re-accretes onto Mars is lower, the fragment size is generally smaller.

Taking the results of the statistically most likely case ($\theta = 45^{\rm o}$), we conclude that the typical fragment size of the impactor's iron core is about 10 m after the giant impact, which is similar to the fragment size from the disrupted core of a lunar-sized impactor during its collision with Earth (Genda et al. 2017a).

We need to emphasize that these 10 m iron fragments are not their final size when they settle on Mars' surface because they experience further fragmentation when these 10 m iron fragments re-accrete back to the martian surface. Iron fragments smaller than cm-size are ejected from the forming crater during re-accretion of the 10 m fragments (i.e. just after these 10 m iron fragments collided onto the martian surface). The typical size of ejected fragments can also be estimated from Eq. (3.1). Given a strain rate $\dot{\varepsilon} \sim v$

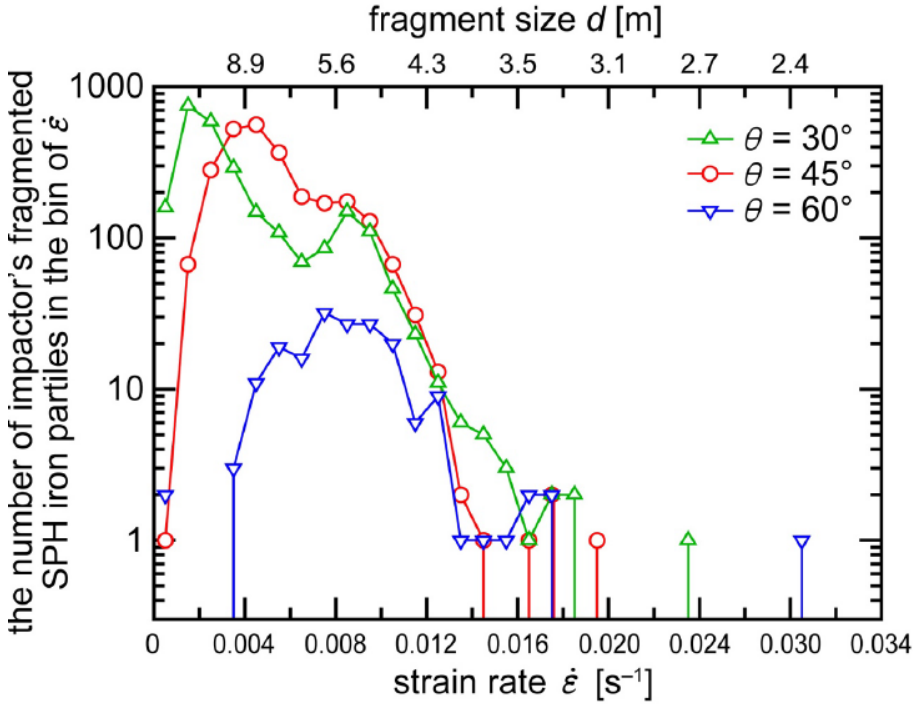

Figure 3.5: Distribution of the strain rate, $\dot{\varepsilon}$, for the impactor's core material at the time of fragmentation, right after the giant impact. The collisions for the impact angle, $\theta = 30^{\circ}$, 45° and 60° with the impact velocity, $v_{\rm imp} = 10$ km/s are plotted. The bin size of $\dot{\varepsilon}$ is 0.001. The fragment size, d, is estimated by the balance between the surface tension of the liquid iron, σ, and $\dot{\varepsilon}$ (see Eq. (3.1)).

3.5 Hydrogen as the byproduct of the colossal impact

If sufficient mm-sized iron fragments rain back onto the surface of Mars, a transient hydrogen atmosphere can potentially be generated by the reduction of water:

$$\mathrm{Fe} + \mathrm{H_2O} \rightarrow \mathrm{FeO} + \mathrm{H_2}. \tag{3.2}$$

This reaction should take place mostly between the mm-sized metallic hail and postulated global surface hydrosphere (or cryosphere) on pre-Noachian Mars, provided that the water of the terrestrial planets was predominantly delivered during the main accretion stage of the planets as opposed to the late veneer (e.g. Greenwood et al. 2018; Dauphas 2017). According to isotopic studies (Sanloup et al. 1999; Dauphas & Pourmand 2011; Brasser et al. 2018) together with dynamical simulations (Ch. 2; Woo et al. (2018)), Mars accreted a higher portion of ordinary chondrite-like material (∼50%) than Earth (<25%) as its building blocks. In contrast, Earth accreted mostly from enstatite chondrite-like sources (Javoy et al. 2010; Dauphas 2017; Brasser et al. 2018), which has a far lower water content (∼0.01 wt%) (Hutson & Ruzicka 2000) than ordinary chondrite (∼0.1 wt%) (McNaughton et al. 1981; Robert et al. 1977, 1979). Based on these analyses, we conclude that the higher portion of ordinary chondrite (Brasser et al. 2018; Woo et al. 2018) together with the low fraction of water-rich (5 – 10 wt%) carbonaceous chondrite (Kerridge 1985; Robert & Epstein 1982) delivered most of the martian water. The total estimated initial martian water budget from the coupled dynamical-cosmochemical modeling results of Brasser et al. (2018) and Woo et al. (2018) corresponds to ∼600 ppm, which is somewhat higher than Mars' current computed bulk water content of 300 ± 150

ppm (Taylor 2013). If most of the water in the martian mantle outgassed during magma ocean solidification and condensed within ∼0.1 Myr after the magma ocean solidification (Lebrun et al. 2013) at ca. 4547 Ma (Bouvier et al. 2018) then it might have created a global surface water reservoir on very early Mars equivalent to a ∼3 km thick ocean (or thicker ice sheet). Mapping of atmospheric water (H_2O) and its deuterated form (HDO) shows a high D/H ratio in the current martian atmosphere, which indicates Mars experienced substantial water loss since the pre-Noachian and hence an ancient water reservoir covering 20% of the martian surface at 4500 Ma (Villanueva et al. 2015). This is also supported by the fractionated xenon isotopes that exist in ancient martian meteorites, which indicates intense water loss possibly within the first few hundred million years of Mars' formation (Cassata (2017); see also Sect. 3.6.3). Plausibility arguments have been made for global surface water to have existed on Mars during the pre-Noachian (see Ramirez & Craddock (2018) for a recent perspective).

Assuming that all fragmented iron that finally ended up suspended in the martian mantle reacts with the postulated surface water reservoir, we calculate that ∼3 bars of hydrogen can be created by reducing $\sim 10^{20}$ kg of water (∼150 ppm) from $\sim 3 \times 10^{20}$ kg of iron materials from the impactor's core. Such a pre-Noachian hydrogen atmosphere is dense enough to act as a greenhouse gas and temporarily increase the surface temperature of the planet above the freezing point of water (Pierrehumbert & Gaidos 2011). We also find that this process yields 10^{21} kg FeO, which accounts for ∼0.14 wt% of the martian mantle's FeO content (the current content of FeO is ∼18 wt% of the martian mantle) measured by Mars' orbiters and rovers, as well as that measured from the martian meteorites (Taylor (2013), and references therein). Thus far, there

are no obvious physical or chemical reasons to preclude the formation of such an atmosphere on very early Mars, except that such an atmosphere should have been short-lived.

The more intense extreme ultraviolet (EUV) of the young sun (Ribas et al. 2010) leads to the rapid decline of the surface pressure of the hydrogen atmosphere through the process of hydrodynamic escape (Hamano et al. 2013; Genda et al. 2017b). The escape flux of hydrogen can be estimated by,

$$\phi_{\mathrm{H_2}} = \frac{\varepsilon_{\mathrm{eff}} f_{\mathrm{EUV}}(t) R}{4GMm_{\mathrm{H_2}}} \Big[\mathrm{m^{-2}s^{-1}}\Big] \tag{3.3}$$

(Watson et al. 1981), where $\phi_{\mathrm{H_2}}$ is the escape flux of $\mathrm{H_2}$, G is the gravitational constant, R is the planetary radius, M is the planetary mass, $m_{\mathrm{H_2}}$ is the molecular mass of $\mathrm{H_2}$, $f_{\mathrm{EUV}}(t)$ is the EUV energy flux received by Mars and $\varepsilon_{\mathrm{eff}}$ is the escape efficiency, which represents how large a proportion of the received EUV energy is available for escaping $\mathrm{H_2}$ molecules. We adopt $\varepsilon_{\mathrm{eff}} = 0.3$ (Sekiya et al. 1980; Genda et al. 2017b) and use the scaling laws of the solar EUV energy flux of Ribas et al. (2005), which is

$$f_{\mathrm{EUV}}(t) = 0.03\Big(\frac{t}{10^9\mathrm{yr}}\Big)^{-1}\Big[\mathrm{Wm^{-2}}\Big], \tag{3.4}$$

where t is the age of the Sun. Since the original f_{EUV} in Ribas et al. (2005) is expressed for the flux received by Earth, we include a factor $(1\ \mathrm{AU}/1.5\ \mathrm{AU})^2$ in Eq. (3.4) to account for the flux received by Mars.

As mentioned in Section 1.4, the LV impact on Mars was likely to have occurred no later than 4.48 Ga (Bouvier et al. 2018), which is ∼80 Myr after the Sun's birth. Thus, we adopt $t = 0.08$ Gyr as the starting time of the giant impact. We should mention that the f_{EUV} scaling law of Ribas et al. (2005) was

derived according to Solar-like stars that are at least 100 Myr old. The time of the hypothetical LV giant impact occurred when the Sun was only 80 Myr old, which is not within the age range considered in Ribas et al. (2005). Nonetheless, the Sun was likely to be in the main sequence stage of its evolution some 50 Myr after its formation (e.g. Siess et al. 2000). Extrapolating the scaling law to $t <$ 100 Myr matches the predicted EUV flux of the Sun in between 50 to 100 Myr after birth (Pizzolato et al. 2003). Therefore, it is valid to adopt the scaling law in Eq. (3.4) when computing the life time of the hydrogen atmosphere. Integrating Eq. (3.3) with the time profile of Eq. (3.4) provides us with the finishing time of the hydrodynamic escape and hence a postulated lifetime of the hydrogen atmosphere. From this we estimate the hydrogen atmosphere persists no more than 3 Myr, which is nearly two orders of magnitude shorter than what has been proposed via core disruption of a lunar-sized impactor in collision with Earth ($\sim$100 Myr; Genda et al. (2017a)).

3.6 Discussion

3.6.1 Factors affecting the lifetime of the hydrogen atmosphere

Several assumptions are at play that can profoundly affect the lifetime estimates of the impact-generated hydrogen atmosphere. The most important of these is the assumed Solar EUV flux. We make use of the EUV flux scaling law deduced by Ribas et al. (2005)). They only examine seven main sequence G-type stars (including the Sun) to compute the scaling laws of stellar fluxes at different wavelengths. Yet, stellar rotational evolution is one of the principal factors that determine its radiative output (Johnstone et al. 2015; Tu et al.

2015). Stars in young clusters (< 500 Myr) have a wide range of rotational rates (Soderblom et al. 1993). According to the EUV flux evolution model of Tu et al. (2015), the EUV flux evolution of stars with different initial rotation periods diverge between the ages of 30 to 1000 Myr. The Tu et al. model takes a broad observation sample into account: they use data from eight young stellar clusters with ages from 30 Myr to 620 Myr. A Solar mass star with a fast initial rotation rate (initial period < 1 day) generates ∼10 times more EUV flux than a slow rotator (initial period comparable to the current Sun's). About 70% of the Solar mass stars studied by Johnstone et al. (2015) belong to this class of slow rotators. Therefore, if the young Sun initially had a low spin rate, its EUV flux intensity would only be about 20 times higher than its current value, instead of about a hundred times higher according to the scaling laws of Ribas et al. (2005). The corresponding survival timescale of a hydrogen atmosphere on Mars could thus be about five times longer (∼10 to 12 Myr) under a weaker EUV flux, but is difficult to extend the life time to 20 Myr.

Another factor affecting the lifetime of the hydrogen atmosphere is the abundance of CO_2 in the martian atmosphere prior the LV impact. Our calculation with Eq. (3.3) and (3.4) does not include other gases that may exist before the LV giant impact. While assuming that a global surface ocean exists on Mars during the first tens millions of years of Mars' history, keeping the average global surface temperature of Mars above the freezing point requires about 1 – 5 bars of CO_2 (Kasting 1991; Forget & Pierrehumbert 1997). If sufficient CO_2 existed before the Late Veneer impact, its 15 μm band infrared emission is the major cooling process in the lower thermosphere of Mars (Gordiets et al. 1982; Lammer et al. 2006) and hence the escape efficiency, $\varepsilon_{\rm eff}$ in Eq. (3.3),

decreases. The solidification of the magma ocean outgasses volatiles and cumulatively yields as much as ∼100 bars of atmosphere composed of H_2O and CO_2 (Elkins-Tanton 2008). According to the hydrodynamical model of Erkaev et al. (2014) retaining this thick initial atmosphere is problematic because it can completely escape within 10 Myr due to the strong EUV of the young Sun; not to mention that ∼100 bars of volatiles in the ancient martian atmosphere is likely an over-estimate. Impact erosion during the first ten million years of Mars' formation (e.g. Melosh & Vickery 1989; Schlichting et al. 2015) is another plausible factor mitigating an initial thick CO_2 atmosphere in the pre-Noachian. Regardless, there is abundant evidence of volcanic activity on Mars that has the potential to re-supply the escaped CO_2 and help offset the loss of a thick atmosphere over geologic time (Michalski et al. (2018), and references therein). It is still unclear precisely when the volcanic activity of Mars began. The Tharsis bulge, which is the largest volcanic complex on Mars, is thought to have initiated its formation during the Noachian epoch (Anderson et al. 2001; Werner 2009). Similar tectonic evidence is lacking for the pre-Noachian epoch because of the postulated LV giant impact or other bombardment events. Colossal impact(s) possibly triggered crustal re-melting and therefore may have erased the corresponding earliest volcanic features on Mars.

3.6.2 Comparison of the Late Veneer giant impact of Earth and Mars

We showed that Mars probably suffered a LV giant impact with a Nerio-sclae impactor (∼1000 km across) and formed transient hydrogen atmosphere for less than 20 Myr. Earth, on the other hand have also been suggested to experienced a LV colossal impact with a lunar size object at its final stage of formation

(Brasser et al. 2016b) and formed a much thicker hydrogen atmosphere (∼90 bar) with much longer survival time (>100 Myr) (Genda et al. 2017a). The major reason for this discrepancy in the survival time scale of hydrogen is that the mass of the iron core of a Nerio-scale impactor is a mere ∼3% of that of a lunar-sized impactor and a mere 0.3 wt% of Mars' mass whereas Moneta is ∼ 1 wt% compared to Earth. The mass of the hydrogen atmosphere, and thus its lifetime, is directly proportional to the total mass of the impactor's iron core reacting with the global surface water on each planet. Mass of Earth is also about 10 times of the mass of Mars. It is more difficult for hydrogen to escape from the surface of Earth than from Mars. The hydrodynamic escape flux for the same amount of hydrogen on Earth is only half of that on Mars according to Eq. (3.3).

According to the U-Pb dating of martian zircons, the proposed timing of the martian LV giant impact is at 4.48 Ga (Bouvier et al. 2018), which is 80 to 90 Myr after the formation of the solar system. This age is much later than the proposed core formation time for Mars, which is less than 10 Myr after the birth of the solar system (Dauphas & Pourmand 2011; Tang & Dauphas 2014) and the inferred Lu-Hf age of the first martian crust at 4547 Ma (Bouvier et al. 2018). One possibility to explain such large time differences in the age of LV and core-formation is that Mars stopped accreting most of its mass early because it was scattered into the empty outer region which is depleted in mass by the migrating Jupiter (Hansen 2009; Walsh et al. 2011; Brasser et al. 2017) in the Grand Tack model. Bouvier et al. (2018) shows that the crust formation of Mars should have been completed within 20 Myr of the Solar system's formation. After the formation of its primodrial crust, Mars could have entered an accretionary lull period until it suffered the LV giant impact at 4.48 Ga. This scenario also

explains why Mars does not fully grow into an Earth-sized planet.

The last major differentiation event on Earth is 4.45-4.48 (Allègre et al. 2008), and the Pb-Pb resetting ages of the Earth consistently show ages of 4.48 Ga (Albarede & Juteau 1984). Such late differentiation is inconsistent with Hf-W dating of the Earth's core formation (Kleine et al. 2009), so the only viable explanation is this resetting caused by a large impact at around 4.48 Ga. It cannot have been the Moon-forming event because the Moon's minimum age is 4.51 ± 0.01 Ga (Barboni et al. 2017; cf. Connelly & Bizzarro 2016), and it is not expected that the Earth had another differentiation event some 30 Myr after the Moon-forming impact.

It is interesting that the timing of the LV giant impact on Earth and Mars coincide with each other at around 4.48 Ga. Mojzsis et al. (2019) attributes the similar timing of these LV impacts to the early giant planet instability (the Nice model, Gomes et al. 2005; Tsiganis et al. 2005; Morbidelli et al. 2005); in that period the giant planets migrated, resulting in an increase of their eccentricities when crossing their mean-motion resonances. This led to the whole outer Solar system become unstable and thus injected a huge amount of Kuiper belt material (Gomes et al. 2005) into the inner region of the Solar system. The asteroid belt could also be destablized by this instability (Morbidelli et al. 2010). While it is originally thought that the giant planet instability triggered an increase in cometary bombardment rate in the inner solar system at ∼3.95 Ga (the Late Heavy Bombardment, LHB), recent studies suggested that the giant planet instability was not delayed by 600 Myr after the formation of the Solar system. Instead, it should have occurred within the first 100 Myr so as to explain the survival of the Jupiter Trojan binary asteroids (Nesvornỳ et al. 2018). The original 3.95 Ga of the LHB is suggested based on the lunar samples returned

by the Apollo missions, which shows impact resetting ages of $^{40-39}$Ar, U-Pb and Rb-Sr ages that seem to cluster around 3.95 Ga (Turner et al. 1973; Tera et al. 1974). However, the crater chronologies of neither the Moon, Mercury nor Mars show evidence of such a LHB event (Werner 2014). The clustering age at 3.95 Ga of the Apollo samples has been suggested to be contaminated by the ejecta of the Imbrium basin (e.g. Schaeffer & Husain 1974; Shearer & Borg 2006; Spudis et al. 2011). Hence, such an increase in impact flux of the inner Solar system, that was possibly caused by the giant impact instability, may not occur at 3.95 Ga. Boehnke & Harrison (2016) also show that the Ar-Ar ages of the Apollo samples are consistent with both a spike and monotonic decay of impact flux, so that the debate of whether a LHB exist needs to be settled with more roust chronometers. By combining geochronological data from more of the inner Solar system samples we have, Mojzsis et al. (2019) argue that the onset of giant planet instability should be no later than 4.48 Ga since there is an absent of whole-scale crustal reset ages after 4.45 Ga from Earth, Moon, Mars, Vesta and various chondritic and achondritic parent bodies; the similar timing of the LV giant impact on Earth and Mars could possibly be due to such instability occurred at 4.48 Ga.

3.6.3 Evidences of the early hydrodynamic escape on Mars

If the hydrodynamic escape caused by impact-generated hydrogen did occur in the past, it probably imprinted isotopic signature(s) in the martian atmosphere since lighter isotopes tend to escape more easily than heavier isotopes, thus increasing the ratio of heavy-to-light isotope ratio. As mentioned in Sect. 3.5,

the high D/H ratio of the martian atmosphere (Villanueva et al. 2015; Hallis 2017) is potential evidence of hydrodynamic escape having occured in the past. Apart from that, the rapid escape of hydrogen may drag along atmospheric xenon (if there is a thin atmosphere with, e.g. < 1 bar during LV) and causes isotopic fractionation of xenon; resulting in the depletion of light xenon isotopes relative to heavy ones. Such evidence is preserved in the ancient martian meteorites. By measuring the xenon isotopes in two ancient martian meteorites, ALH 84001 and NWA 7034, Cassata (2017) found that their heavy xenon isotope ratios $^{136}Xe/^{132}Xe$ are indistinguishable from those in the modern martian atmosphere. Both ALH 84001 and NWA 7034 formed between 4.1 and 4.4 Ga (Cassata et al. 2010; Bellucci et al. 2015; Nemchin et al. 2014) and their $^{129}Xe/^{132}Xe$ ratios are similar to each other but lower than modern martian atmospheric Xe. $^{129}Xe/^{132}Xe$ increases with time, likely due to magmatic outgassing of mantle rocks enriched in ^{129}Xe, which is a decay produce of ^{129}I (half life = 15.7 Myr). These gas components in both meteorites are trapped in the meteorites during their formation and therefore represents the ancient martian atmosphere before 4.1 Ga (Cassata 2017). The overall results suggest that Mars experienced hydrodynamic escape only for the first few hundred millions years after formation. In contrast, xenon isotopic fractionation on Earth lasted for almost 2.5 Gyr (Pujol et al. 2011; Avice et al. 2018).

As discussed, the timing of the LV is likely to be 4.48 Ga, which matches the time atmospheric escape occured as concluded from Cassata (2017). Therefore, we also examine whether or not the hydrogen escape flux generated by the LV giant impact is sufficient to drag xenon. We estimate the "crossover mass", $m_{\rm c}$, which represents the maximum mass of an atom or molecule that can be

dragged along with the escaping hydrogen (Hunten et al. 1987; Pepin 1997).

$$m_{\rm c} = m_{\rm H_2} + \frac{kT\phi_{\rm H_2}}{bgX_{\rm H_2}}, \tag{3.5}$$

where k is the Boltzmann's constant, T is the atmospheric temperature, g is the gravitational acceleration, b is the diffusion parameter of ^{130}Xe in hydrogen molecule and $X_{\rm H_2}$ is the mole fraction of hydrogen. Adopting T = 200 K (equilibrium temperature of Mars at that time, Erkaev et al. (2014)), $b = 2.7 \times 10^{17} T^{0.712}$ cm^{-1} s^{-1} (Mason & Marrero 1970; Zahnle & Kasting 1986) and $X_{\rm H_2}$ = 1, we find that the minimum flux that is required to drag xenon is 3.38 $\times$ 10^{17} m^{-2}s^{-1}. The initial hydrogen escape flux $\phi_{\rm H_2}$ resulting from the LV giant impact, however, is only 1.82 $\times$ 10^{17} m^{-2}s^{-1} (based on the EUV flux scaling law of Ribas et al. (2005)), which is not enough to drag neutral xenon.

Our previous estimation of the hydrogen escape flux and crossover mass do not account for photo-dissociation of molecules, ionisation of atoms and the coupling effect between ions and the dipole magnetic field of the planet. Indeed, under strong EUV flux, H_2 can be photo-dissociated to H atom and both H and Xe can be ionised. The ionisation energy of Xe is 12.1 eV ($\lambda \sim 102$ nm), which is lower than that of H (13.6 eV, $\lambda \sim 91$ nm) (Zahnle et al. 2019). If Mars produced a strong magnetic field early in its life time (Acuna et al. 1998), H^+ ion could drag away Xe^+ ion and escape together along the open B-field lines of Mars as polar wind (Zahnle 2015; Zahnle et al. 2019). The corresponding hydrogen escape flux required to drag Xe^+ is $\sim$10 times lower than that required to drag neutral Xe (Zahnle 2015) because of the strong Coulomb interaction between ions. Therefore, it may still be possible to explain the early xenon isotopic fractionation by the escape of the hydrogen atmosphere generated by the LV giant impact. Further work is warranted to study the early isotopic fractionation

of xenon on Mars and the early atmospheric evolution of the planet (see Ch. 4 for suggestion of future work).

3.7 Conclusions

We performed SPH simulations to study the consequence of a Late Veneer colossal impact between Mars and Nerio, a ∼1000 km diameter impactor that delivered part of the martian Late Veneer. We found that about half of the impactor's core materials undergo fragmentation and become bound to Mars' mantle after impact in the collision scenario that is statistically most likely ($v_{\rm imp}$ = 10 km/s and $\theta = 45^{\rm o}$). These iron fragments are able to enrich the martian mantle with highly siderophile elements. The typical size of one of the fragments is ∼10 m after the first collision. These fragments are further torn into mm-sized iron blobs during re-accretion onto Mars. Assuming that global surface water existed in either ice or liquid form during the Late Veneer, the re-accreted mm-sized iron blobs reacted with the surface water reservoir and created ∼3 bars of hydrogen, which is thick enough to act as a greenhouse gas. According to the traditional EUV flux's scaling law (Ribas et al. 2005), this hydrogen atmosphere is expected to have completely escaped within 3 Myr, which makes it difficult for it to have had a significant effect on the surface environment of Mars for a long enough time. However, making assumptions with a slower rotating young Sun with weaker Solar EUV radiation and an initial thick carbon dioxide atmosphere would significantly extend the lifetime of the hydrogen atmosphere to more than 10 Myr, but not 20 Myr. This is much shorter than the one formed after the Late Veneer giant impact on Earth (> 100 Myr, Genda et al. 2017a), which suggests that Mars probably did not have an long-living post-impact biosphere after the

giant impact. We also found that the escape of the hydrogen atmosphere is strong enough to drag ionised xenon but not neutral xenon. Since xenon can be easily ionised, hydrogen escape due to the Late Veneer impact may be able to explain the early xenon isotopic fractionation (before 4.1 Ga) recorded by the ancient martian meteorites (Cassata 2017). Given the greenhouse nature of hydrogen gas and its implication for biopoesis on early Hadean Earth (e.g. Urey 1952; Miller et al. 1953; Ferus et al. 2017), we call for further study on the possible generation of an early hydrogen atmosphere and its effect on pre-Noachian Mars (see the next section).

Chapter 4

Future prospects of studies related to the origin and the evolution of Mars

In this chapter, based on the results we obtained in Ch. 2 and 3, we discuss the approximations, strengths and weaknesses of our study and suggest some future improvements required with simulation methods and isotopic data in solving the mysteries of the formation and the evolution of Mars. Suggestions for future studies will also be made.

4.1 Combining N-body simulations with isotopic data

In Ch. 2, we coupled the results of N-body simulations and cosmochemical data to test the possibility of forming Earth and Mars with their documented

bulk composition simultaneously, with Mars having a higher fraction of ordinary chondrite-like material than Earth (Sanloup et al. 1999; Tang & Dauphas 2014; Brasser et al. 2018). Our initial conditions involve embryos with ∼0.01 to 0.1 $M_{\oplus}$, which are thousands of km in size. In many cases, the masses and the final bulk composition of Mars analogues are dominated by only a few embryos, whose composition depends on their initial locations in the disc with a break location (Sect. 2.4.1). This problem leads to a huge uncertainty in the bulk composition of Mars (±20% to 30%) (see Fig. 2.7). It is difficult to make a precise conclusion on the formation and early dynamical path of Mars due to the huge uncertainty of the computed composition for Mars. Increasing the resolution of the simulation is a solution. We could start the simulations with smaller embryos ($< 0.01 M_{\oplus}$) or even only planetesimals (∼10 to 10^2 km in size). However, this would increase the total number of particles in the simulations and greatly increase simulation time (close to a year for each simulation using N-body code SyMBA!). Therefore, we either have to wait for improvement of CPU performance in the future, which only appears to occur in CPU core count rather than raw clock speed, or use another N-body code. The symplectic N-body code GENGA (Grimm & Stadel 2014), which allows simulations performed with many more particles (∼10,000 compared to about a few thousands at most for SyMBA) on the GPU within a reasonable time. By using the new GPU-based N-body code or a faster CPU, more simulations can be performed with other planet formation models, such as the *empty asteroid belt* model (Izidoro et al. 2014) in which the primordial asteroid belt and the region around Mars' current orbits are nearly empty because of the radial drift and subsequent pile up of solids in the pressure bump within 1 AU (Drażkowska

et al. 2016; Raymond & Izidoro 2017); the *pebble accretion* model with sub-meter pebbles that were generated mainly in the outer Solar System (Ida et al. 2016) or throughout the disc (Levison et al. 2015) and accreted to planetesimals and embryos to form planets; the *early giant planet instability* model in which the giant planet triggered an orbital instability within 10 Myr after the gas disc dispersed (Clement et al. 2018). All these models have yet to be examined in forming the documented bulk composition of Earth and Mars.

The huge uncertainty problem is not only limited to the bulk and isotopic composition of Mars computed from simulation results, but also the isotopic anomalies measured from the martian meteorites. At the end of Ch. 2, we mentioned that the uncertainties of the measured isotopic composition of Mars for some elements are comparable to their corresponding computed values from simulations. Table 2.4 lists the comparisons between them. Apart from Δ^{17}O and ε^{54}Cr, all the uncertainties of the measured isotopic composition are of the same order of magnitude as the calculated values. This indicates that we need an improvement of isotopic data of Mars, in particular Ni and Mo. Achieving this require efforts from cosmochemists to develop new experimental techniques for measuring isotopic composition. As mentioned in Sect. 2.5, Ni and Mo are regarded as moderately siderophile elements, which means that part of them sink to the martian core with iron during the core formation of Mars. The moderately siderophile elements that delivered late tend to be more likely to remain in the mantle than those were delivered early. More accurate measurements of Ni and Mo from the martian meteorites provides information on the composition of the later stage (about the final 20 to 40wt%, Rubie et al. (2015); Dauphas (2017)) building blocks of Mars.

Our results from Ch. 2 are based on the N-body simulations performed with

SyMBA. The biggest advantage of using SyMBA is that it is a well-tested and well-used N-body code to study planet formation that integrates the gravitational equations of motion in a symplectic manner using clever potential splitting (Duncan et al. 1998). It assumes perfect accretion when collision occurs. This assumption has been proven to have only a limited effect on the final dynamical structure (e.g orbital semi major axis and average planetary mass, Kokubo & Genda 2010; Quintana et al. 2016) of the system. If assuming perfect accretion does not have a significant effect on the final average mass of the system, it should not affect the computed final average composition of the planet. However, using SyMBA limited our resolution for long simulations because of severe limitations in CPU power of the clusters and because the symplectic method requires a fixed time step that is set by the distance of the closest planetesimal to the Sun. As such, we typically need to calculate 10^{10} steps for the whole simulation, or sometimes more, which requires several months on the cluster. As pointed out above, our limited number of planetesimals causes big uncertainties in the computed bulk composition of Mars. Increased simulation resolution is the best way to solve the problem.

A major assumption that went into this work pertains to the initial conditions, which consists of planetary embryos and planetesimals (Kokubo & Ida 1998). At this stage there is some debate within the community regarding the validity of these initial conditions. At present a more detailed model using collisional fragmentation (Walsh & Levison 2019) does not appear to yield initial conditions very different from the oligarchic model that we have adopted. As such, our initial conditions are valid at this time, and future study is needed to validate or disprove this claim.

We assumed chondrites as the building blocks of the terrestrial planets in

this study. In truth, we do not know the identity of the planets' building blocks. Our assumption only based on the meteorites that fall on Earth. However, these meteorites may not represent the whole population of the starting material of planets. Some isotopic studies have suggested that there is a hidden reservoir of the inner Solar system's material, which does not exist in our current meteoritic collection (Render et al. 2017). This indicates that we need more meteorites or samples from asteroids in order to solve the problem. Sample return missions, similar to the currently operating JAXA's *Hayabusa2* and NASA's *OSIRIS-REx* missions, can help extending our samples' collection and also our understanding on the primitive Solar system material.

Unifying the dynamics with cosmochemistry is a major new step forward that allows us to incorporate new constraints and thus better derive what the formation process of the inner planets could have been. Several international groups are now beginning to undertake the very same approach.

4.2 HSEs' data of Mars and future LV related simulations

In order to form a complete picture of the Mars' formation and evolution history, we require isotopic data of not only lithophile and moderately siderophile elements, but also the highly siderophile elements (HSEs). HSEs have to be delivered by Late Veneer (LV) accretion (about the final 0.8wt%) (see Sect. 1.4; Day et al. (2016)). The results from a Monte Carlo mixing model of Brasser et al. (2018) fail to constrain the composition of the martian LV accretion (i.e. we still do not know whether the material contributed to the LV of Mars is enstatite, ordinary or carbonaceous-like chondritic material). The reason is that

we currently do not have any measured isotopic anomaly of HSEs (e.g Ru) in martian meteorite. These elements are difficult to measure because of their extremely low abundance in the silicate phase (i.e. crust and mantle) and the limited samples of the martian meteorites. The nature of the LV accretion of Mars is important for our study in Ch. 3 because of the difference in abundance of reduced iron in enstatite chondrite and ordinary chondrite. Enstatie chondrite has a higher fraction of reduced iron (Wasson & Kallemeyn 1988), which can react with the surface water on Mars to generate hydrogen. We assumed the Late Veneer impactor is enstatite chondrite in Ch. 3. If LV accretion of Mars is mainly an ordinary chondritic impactor, a thinner hydrogen atmosphere with a shorter life time would have formed. Therefore, to gain a better understanding of LV accretion and hence further consider the LV giant impact as a trigger of the birth of life, we should either search for more samples from Mars or developing new techniques in measuring the isotopic anomalies of HSEs in limited amount of the martian meteorites. Future martian moon's sample return mission of JAXA's MMX (Martian Moons eXploration), aiming to launch in the early 2020s, could help. If the LV giant impact is the cause of forming the martian moons, their bulk and isotopic composition would be mixture of Mars' and the impactor (Hyodo et al. 2017). Therefore, the nature of a LV impactor can be inferred from the isotopic composition of the martian moons and Mars.

We concluded that a short-lived hydrogen atmosphere could have formed on Mars after the LV giant impact. Our estimation on a pure hydrogen atmosphere's life time on Mars (3 to 12 Myr, see Sect. 3.5) is based on a simple analytical equation (Watson et al. 1981). A more detailed study on this temporary but scientifically instructive H_2 envelope is warranted in the future. Studies

of the hydrodynamic escape on the early Mars with a 1-D hydrodynamic atmospheric model is an ideal method. The model should include the assumption of different solar EUV flux and the mixing ratio of hydrogen in background gases, such as CO_2 and N_2. It is worth to mentioning again that the key to studying Mars' and the early Solar System's evolution is making use of the martian meteorites. They provide not only the isotopic composition of the martian silicate mantle, but also hints of its ancient atmosphere. Therefore, the results of the hydrodynamic escape should be compared to the ancient martian atmospheric isotopic data, for instance D/H ratio and xenon isotopes. A recent study on the atmospheric escape during Archean Earth has been conducted by Zahnle et al. (2019). They make use of a 1-D diffusion-limited hydrodynamic model to examine the condition in which the hydrodynamic escape flux was strong enough to mass fractionate xenon. A similar method could be adopted to investigate that hydrodynamic escape on Mars.

In Ch. 3, we adopted the Smoothed-particle hydrodynamics (SPH) method and assumed both the impactor and the target were composed of many smaller SPH particles (hundred km across) interacting with each other with pressure gradient force and mutual gravity (See Appendix B). Particle number was once again limited by the available computing power. The advantage of this SPH method is that the system is stable in large deformation and it is easy to study the distribution of one material (iron) within the another material (silicate). However, the scale of the SPH particle (km size) is large compared to the fragment size (cm to mm size). We can only calculate the large scale strain rate with the SPH code and ignore the small scale effects, such as turbulence and viscosity, in calculating the fragment size. In the future, we would like to include these effects in calculating the fragment size, even though we do not

expect this would change our conclusion. We can also study the giant impact by adopting Eulerian, grid-based method with adaptive mesh refinement (AMR-CTH, Crawford et al. 2006) to confirm the accuracy of our SPH results.

4.3 Final summary

To conclude, I demonstrate that by combining numerical simulations' results (N-body and SPH simulation) with cosmochemical data from martian meteorites, improvement of both numerical simulation methods and the quality of isotopic data are required to constraint the formation and early evolution of Mars. The history of the early Solar System and hence the origin of life can only be figured out by interdisciplinary studies – combining the efforts from planetary dynamists, hydrodynamists, cosmochemists and biochemists.

Appendix A

Introduction to SyMBA

SyMBA is a second-order symplectic integrator for the gravitational N-body problem (Duncan et al. 1998). Symplectic integrators are designed for the numerical solution of the Hamiltonian equation,

$$\dot{\boldsymbol{p}} = -\frac{\partial H}{\partial \boldsymbol{q}} \quad \text{and} \quad \dot{\boldsymbol{q}} = \frac{\partial H}{\partial \boldsymbol{p}} \tag{A.1}$$

where $\boldsymbol{q}$ represents the position coordinates, $\boldsymbol{p}$ denotes the momentum coordinates and H is the Hamiltonian of the system.

A.1 MVS method

SyMBA is developed based on the mixed variable symplectic (MVS) methods proposed by Wisdom & Holman (1991). In the MVS method, the Hamiltonian (i.e. total energy) of an N-body system is expressed as

$$H = H_{\rm Kep} + H_{\rm int} \tag{A.2}$$

where $H_{\rm Kep}$ is the part of the Hamiltonian that describes the Keplerian motion of the bodies around the central object (the Sun in this study) and $H_{\rm int}$ is the part that describes the perturbation of the bodies (planetary embryos and planets) on one another. Wisdom & Holman (1991) wrote

$$H_{\rm Kep} = \sum_{i=1}^{n} \left(\frac{|\boldsymbol{p}'|^2}{2m_i{}'} - \frac{Gm_i m_0}{r_i{}'} \right), \tag{A.3}$$

and

$$H_{\rm int} = \sum_{i=1}^{n} \left(\frac{Gm_i m_0}{r_i{}'} - \frac{Gm_i m_0}{r_{i0}} \right) - \sum_{i=1}^{n-1} \sum_{j=i+1}^{n} \frac{Gm_i m_j}{r_{ij}} \tag{A.4}$$

where m_0 and m_i are the mass of the Sun and body i, respectively, r_{i0} is the distance between body i and the Sun and the primed variable refers to the Jacobi coordinates. Based on Eq. (A.2), (A.3) and (A.4), the second-order MVS integrator can be expressed as

$$E_{\rm Kep}\left(\frac{\tau}{2}\right) E_{\rm int}(\tau) E_{\rm Kep}\left(\frac{\tau}{2}\right), \tag{A.5}$$

where $E_i(\tau)$ denotes the evolution operator under H_i for a time step τ. Eq. (A.5) can be understood as follows: (1) a second-order MVS integrator first evolves all bodies along their Kepler orbits for time $\tau/2$, (2) then a kick is applied to the momentum of each particle due to the Hamiltonian of mutual perturbation $H_{\rm int}$, which is a function of $\boldsymbol{q_i}$ only, and (3) all the bodies evolve along their new Kepler orbits again for time $\tau/2$. The advantage of adopting this leapfrog integration is that the energy error of the system is bounded.

However, the MVS method requires fixed time step τ and is only useful when there are no close encounters between objects since $H_{\rm int}$ would grow too large when close encounters between objects occur. Thus, Duncan et al. (1998)

developed SyMBA to solve the problem of close encounters between objects by introducing the multiple time step approach.

A.2 Multiple time step symplectic methods

In the multiple time step approach, Duncan et al. (1998) first considered a two-body Kepler problem (i.e. the Sun and a planet) and placed a series of shells (with radius $R_1 > R_2 > ....$) around the Sun, associating a smaller time step with a smaller shell. When the planet approaches the Sun and crosses these shells, the time step of the integration decreases, hence allowing a higher resolution simulation during the planet's perihelion passage.

During close encounters between the Sun and the planet, the traditional "T + V" Hamiltonian is considered, which is

$$H = H_T + H_V, \tag{A.6}$$

where H_T and H_V are the orbital kinetic and potential energy of the planet, respectively. Since the potential energy of the planet depends on its position from the Sun (1/r), H_V can be decomposed into $\sum_k V_k$. Therefore, the Hamiltonian is written as

$$H = H_T + \sum_{k}^{\infty} V_k. \tag{A.7}$$

With the Hamiltonian in Eq. (A.7), Duncan et al. (1998) modified the second-order symplectic integrator in Eq. (A.5) into

$$\begin{aligned} E_{\sum_0}(\tau_0) &\approx E_0\left(\frac{\tau_0}{2}\right)E_{\sum_1}(\tau_0)E_0\left(\frac{\tau_0}{2}\right) \\ &\approx E_0\left(\frac{\tau_0}{2}\right)\left[E_1\left(\frac{\tau_1}{2}\right)E_{\sum_2}(\tau_1)E_1\left(\frac{\tau_1}{2}\right)\right]^M E_0\left(\frac{\tau_0}{2}\right) \\ &\vdots \end{aligned} \tag{A.8}$$

where $E_i(\tau)$ and $E_{\sum_i}(\tau)$ denote the evolution of the planet orbit under V_i and $H_T + \sum_{k=i}^{\infty} V_k$, respectively for a time step τ. The first line of Eq. (A.8) is identical to the second-order scheme described by Eq. (A.5), in which the planet orbit is evolved with V_0 as the outer half-steps. The central operator $E_{\sum_1}(\tau_0)$ is then further divided into operators with smaller time steps. At each level i of the recursion, the evolution under $E_{\sum_i}(\tau_{i-1})$ is approximated by M second-order steps of length τ_i with E_i as the outer half-steps, where $M = \tau_i/\tau_{i+1}$ is an integer and a constant. The recursion of the central operator continues until $E_{\sum_{n+1}}$ is reduced to $E_T(\tau_n)$, where E_T is the evolution under H_T.

This method can be extended to calculate more bodies. For the gravitational N-body problem, the potential Hamiltonian H_V can be written as

$$H_V = -\sum_{i=0}^{n-1}\sum_{j=i+1}^{n}\frac{Gm_im_j}{r_{ij}} = \sum_{i=0}^{n-1}\sum_{j=i+1}^{n} V_{ij}. \tag{A.9}$$

Dividing each term by the technique discussed above so that

$$H_V = \sum_{i=0}^{n-1}\sum_{j=i+1}^{n}\sum_{k=0}^{\infty} V_{ijk}. \tag{A.10}$$

Eq. (A.10) handles each force pair independently. Thus, during close encounters

the mutual gravitational force between that pair and only that pair is sampled on a shorter time step.

Developed through a combination of the MVS method (Sect. A.1) and the the multiple time step method (current section), SyMBA retains the advantage of the speed of the MVS method when the bodies are well separated; it can also handle close encounters by switching to the multiple time step technique.

Appendix B

Smoothed-particle hydrodynamics

Smoothed-particle hydrodynamics (SPH) method (e.g. Monaghan 1992) is a flexible Lagrangian method of solving hydrodynamics equation. The basic idea of the SPH method is to divide a system (in our case a target and an impactor) into many numbers of particles (SPH particles) and each particle interact with its neighbour particles through pressure gradient force and mutual gravity.

The equation of motion for the ith SPH particles is given by

$$\frac{d\mathbf{v}_i}{dt} = -\sum_{j}^{\text{neighbour}} \mathcal{F}_{ij} - \sum_{j}^{\text{all}} \mathcal{G}_{ij} \tag{B.1}$$

(Genda et al. 2012), where $\mathbf{v}_i$ is the velocity of the ith SPH particle, t is the time, and $\mathcal{F}_{ij}$ and $\mathcal{G}_{ij}$ are the pressure gradient and mutual gravity terms between the ith and jth particles, respectively. The pressure gradient term is expressed

as

$$\mathcal{F}_{ij} = m_j\big(\frac{P_i}{\rho_i^2} + \frac{P_j}{\rho_j^2} + \Pi_{ij}\big)\nabla_i W(r_{ij}, h_{ij}), \tag{B.2}$$

where m_j, P_j and ρ_j are the mass, pressure and density of the jth particle, respectively, Π_{ij} is the artificial viscosity, W is the kernel function, r_{ij} is the distance between the ith and jth particles, and h_{ij} is the average smoothing length of the ith and jth particles.

We adopt a Von Neumann-Richtmyer-type viscosity with parameters of $\alpha_{\rm vis}$ = 1.5 and $\beta_{\rm vis}$ = 3.0, as described in Sect. 4 of Monaghan (1992). The kernel function W in Eq. (B.2) is the function representing the interaction between neighboring particles i and j with characteristic radius equals to the average smoothing length h_{ij}. This means that particle j becomes "effective" in adding pressure on particle i when particle j enter the "kernel" of particle i. We use the spherically symmetric spline kernel function proposed by Monaghan & Lattanzio (1985):

$$W(r,h) = \frac{1}{\pi h^3}\begin{cases} 1 - \frac{3}{2}\big(\frac{r}{h}\big)^2 + \frac{3}{4}\big(\frac{r}{h}\big)^3, & 0 \le \frac{r}{h} < 1, \\ \frac{1}{4}\big(2 - \frac{r}{h}\big)^3, & 1 \le \frac{r}{h} < 2, \\ 0, & 2 \le \frac{r}{h}. \end{cases} \tag{B.3}$$

This function satisfies $\int W(r,h)dr = 1$ and equals zero when $r \ge 2h$. h is a variable for each SPH particle with time, and determined to satisfy the condition that the number of neighouring particles, $N_{\rm nei}$ within $2h$ to be close to 64 ($N_{\rm nei}$ = 64 $\pm$ 2) in our code.

The mutual gravity term in Eq. (B.1) can be written as

$$\mathcal{G}_{ij} = G\sum_j \hat{m}_j \frac{\mathbf{r}_i - \mathbf{r}_j}{r_{ij}^3}, \tag{B.4}$$

where G is the gravitational constant and $\hat{m}$ is defined by

$$m_j = \int_0^{r_{ij}} 4\pi r^2 m_j W(r, h_{ij}) dr, \tag{B.5}$$

which is the effective mass of the jth particle toward the ith particle. This equation gives $\hat{m}_j = m_j$ when $r_{ij} \geq 2h_j$.

Appendix C

Strain rate tensor

Right after a giant impact, shock wave is generated and passes through the impactor's iron core. This results in melting of impactor's iron materials and ejection of these materials from the martian surface. After ejection into open space, the iron core materials expand due to their high residual internal pressure. This induces local kinetic energy, $1/2mv^2$, in the expanding iron materials. Here, $v = \dot{\varepsilon}d$ is the local shear velocity, in which $\dot{\varepsilon}$ is the strain rate and d is the typical size of the molten droplets ejected by an impact (i.e. size of fragments).

$\dot{\varepsilon}$ describes the deformation rate of the expanding iron melt. We calculate $\dot{\varepsilon}$ at the position x through:

$$\dot{\varepsilon}^{\alpha\beta} = \frac{1}{2}\left(\frac{\partial v^{\alpha}}{\partial x^{\beta}} + \frac{\partial v^{\beta}}{\partial x^{\alpha}}\right), \tag{C.1}$$

where the superscript α and β are the directions of the $x-$, $y-$ or $z-$ axis. In the SPH code, the strain rate of the expanding iron material can be calculated with the strain rate tensor. By summing up the contribution of the neighboring SPH particles, the strain rate tensor of the i-th SPH particle can be calculated

as

$$\dot{\varepsilon}^{\alpha\beta} = \frac{1}{2\rho_i} \sum_j m_j \big[(v_j^\alpha - v_i^\alpha) \frac{\partial W_{ij}}{\partial x_i^\beta} + (v_j^\beta - v_i^\beta) \frac{\partial W_{ij}}{\partial x_i^\alpha} \big] \tag{C.2}$$

(Benz & Asphaug 1994), where m is the mass of the SPH particle, ρ is the density and W is the kernel function defined in Eq. (B.3). The subscript j represent the number of neighboring SPH particles, which is set to 64 in our calculation. Eq. (C.2) is the strain rate tensor in one-dimension. By summarizing the strain rate tensor in all three dimensions, the effective strain rate $\dot{\varepsilon}$ of the ith SPH particle is

$$\dot{\varepsilon} = \big[\frac{1}{2} \sum_{\alpha\beta} \dot{\varepsilon}^{\alpha\beta} \big]^{1/2}. \tag{C.3}$$

Bibliography

Abe, Y. 1993, Lithos, 30, 223

Acuna, M., Connerney, J., Wasilewski, P. a., et al. 1998, Science, 279, 1676

Agee, C. B., Wilson, N. V., McCubbin, F. M., et al. 2013, Science, 339, 780

Agnor, C. B., Canup, R. M., & Levison, H. F. 1999, Icarus, 142, 219

Albarede, F. & Juteau, M. 1984, Geochimica et Cosmochimica Acta, 48, 207

Allègre, C. J., Manhès, G., & Göpel, C. 2008, Earth and Planetary Science Letters, 267, 386

Anderson, R. C., Dohm, J. M., Golombek, M. P., et al. 2001, Journal of Geophysical Research: Planets, 106, 20563

Andrews-Hanna, J. C., Zuber, M. T., & Banerdt, W. B. 2008, Nature, 453, 1212

Avice, G., Marty, B., Burgess, R., et al. 2018, Geochimica et Cosmochimica Acta, 232, 82

Badro, J., Brodholt, J. P., Piet, H., Siebert, J., & Ryerson, F. J. 2015, Proceedings of the National Academy of Sciences, 112, 12310

Barboni, M., Boehnke, P., Keller, B., et al. 2017, Science advances, 3, e1602365

Becker, H., Horan, M., Walker, R., et al. 2006, Geochimica et Cosmochimica Acta, 70, 4528

Bellucci, J., Nemchin, A., Whitehouse, M., et al. 2015, Earth and Planetary Science Letters, 410, 34

Benz, W. & Asphaug, E. 1994, Icarus, 107, 98

Bitsch, B., Johansen, A., Lambrechts, M., & Morbidelli, A. 2015, Astronomy & Astrophysics, 575, A28

Bitsch, B., Morbidelli, A., Lega, E., Kretke, K., & Crida, A. 2014, Astronomy & Astrophysics, 570, A75

Boehnke, P. & Harrison, T. M. 2016, Proceedings of the National Academy of Sciences, 113, 10802

Bond, J. C., Lauretta, D. S., & OBrien, D. P. 2010, Icarus, 205, 321

Borg, L. E., Brennecka, G. A., & Symes, S. J. 2016, Geochimica et Cosmochimica Acta, 175, 150

Bottke, W. F. & Andrews-Hanna, J. C. 2017, Nature Geoscience, 10, 344

Bottke, W. F., Walker, R. J., Day, J. M., Nesvorny, D., & Elkins-Tanton, L. 2010, science, 330, 1527

Bouvier, A. & Wadhwa, M. 2010, Nature geoscience, 3, 637

Bouvier, L. C., Costa, M. M., Connelly, J. N., et al. 2018, Nature, 558, 586

Brandon, A. D., Puchtel, I. S., Walker, R. J., et al. 2012, Geochimica et Cosmochimica Acta, 76, 206

Brasser, R., Dauphas, N., & Mojzsis, S. J. 2018, Geophysical Research Letter, 45, 5908

Brasser, R., Matsumura, S., Ida, S., Mojzsis, S., & Werner, S. 2016a, The Astrophysical Journal, 821, 75

Brasser, R. & Mojzsis, S. 2017, Geophysical Research Letters, 44, 5978

Brasser, R., Mojzsis, S., Matsumura, S., & Ida, S. 2017, Earth and Planetary Science Letters, 468, 85

Brasser, R., Mojzsis, S., Werner, S., Matsumura, S., & Ida, S. 2016b, Earth and Planetary Science Letters, 455, 85

Brennecka, G. A., Borg, L. E., & Wadhwa, M. 2013, Proceedings of the National Academy of Sciences, 110, 17241

Burkhardt, C., Kleine, T., Dauphas, N., & Wieler, R. 2012, Earth and Planetary Science Letters, 357, 298

Canup, R. M. 2008, Icarus, 196, 518

Carlson, R. W., Brasser, R., Yin, Q.-Z., Fischer-Gödde, M., & Qin, L. 2018, Space Science Reviews, 214, 121

Cassata, W. S. 2017, Earth and Planetary Science Letters, 479, 322

Cassata, W. S., Shuster, D. L., Renne, P. R., & Weiss, B. P. 2010, Geochimica et Cosmochimica Acta, 74, 6900

Chambers, J. 2001, Icarus, 152, 205

Chambers, J. 2006, Icarus, 180, 496

Chou, C.-L. 1978, in Lunar and Planetary Science Conference Proceedings, Vol. 9

Citron, R. I., Genda, H., & Ida, S. 2015, Icarus, 252, 334

Clayton, D. D. 1977, Icarus, 32, 255

Clement, M. S., Kaib, N. A., Raymond, S. N., & Walsh, K. J. 2018, Icarus, 311, 340

Connelly, J. & Bizzarro, M. 2016, Earth and Planetary Science Letters, 452, 36

Coradini, A., Capaccioni, F., Erard, S., et al. 2011, Science, 334, 492

Craddock, R. A. 2011, Icarus, 211, 1150

Crawford, D., Taylor, P., Bell, R., & Hertel, E. 2006, Russian Journal of Physical Chemistry B, 25, 72

Dauphas, N. 2017, Nature, 541, 521

Dauphas, N., Chen, J. H., Zhang, J., et al. 2014, Earth and Planetary Science Letters, 407, 96

Dauphas, N. & Pourmand, A. 2011, Nature, 473, 489

Day, J. M., Brandon, A. D., & Walker, R. J. 2016, Reviews in Mineralogy and Geochemistry, 81, 161

Day, J. M., Pearson, D. G., & Taylor, L. A. 2007, Science, 315, 217

Day, J. M., Tait, K. T., Udry, A., et al. 2018, Nature communications, 9, 4799

Day, J. M. & Walker, R. J. 2015, Earth and Planetary Science Letters, 423, 114

Debaille, V., Brandon, A., Yin, Q.-Z., & Jacobsen, B. 2007, Nature, 450, 525

DeMeo, F. & Carry, B. 2014, Nature, 505, 629

Desch, S. J., Kalyaan, A., & Alexander, C. M. 2018, The Astrophysical Journal Supplement Series, 238, 11

Drażkowska, J., Alibert, Y., & Moore, B. 2016, Astronomy & Astrophysics, 594, A105

Duncan, M. J., Levison, H. F., & Lee, M. H. 1998, The Astronomical Journal, 116, 2067

Elkins-Tanton, L. T. 2008, Earth and Planetary Science Letters, 271, 181

Elser, S., Meyer, M. R., & Moore, B. 2012, Icarus, 221, 859

Erkaev, N., Lammer, H., Elkins-Tanton, L., et al. 2014, Planetary and space science, 98, 106

Ferus, M., Pietrucci, F., Saitta, A. M., et al. 2017, Proceedings of the National Academy of Sciences, 114, 4306

Fischer, R. A., Nimmo, F., & O'Brien, D. P. 2018, Earth and Planetary Science Letters, 482, 105

Fischer-Gödde, M. & Kleine, T. 2017, Nature, 541, 525

Fitoussi, C., Bourdon, B., & Wang, X. 2016, Earth and Planetary Science Letters, 434, 151

Forget, F. & Pierrehumbert, R. T. 1997, Science, 278, 1273

Franchi, I., Wright, I., Sexton, A., & Pillinger, C. 1999, Meteoritics & Planetary Science, 34, 657

Frank, E. A., Maier, W. D., & Mojzsis, S. J. 2016, Contributions to Mineralogy and Petrology, 171, 29

Genda, H. & Abe, Y. 2005, Nature, 433, 842

Genda, H., Brasser, R., & Mojzsis, S. 2017a, Earth and Planetary Science Letters, 480, 25

Genda, H., Fujita, T., Kobayashi, H., Tanaka, H., & Abe, Y. 2015, Icarus, 262, 58

Genda, H., Iizuka, T., Sasaki, T., Ueno, Y., & Ikoma, M. 2017b, Earth and Planetary Science Letters, 470, 87

Genda, H., Kokubo, E., & Ida, S. 2012, The Astrophysical Journal, 744, 137

Gomes, R., Levison, H. F., Tsiganis, K., & Morbidelli, A. 2005, Nature, 435, 466

Gordiets, B., Kulikov, Y. N., Markov, M., & Marov, M. Y. 1982, Journal of Geophysical Research: Space Physics, 87, 4504

Gradie, J. & Tedesco, E. 1982, Science, 216, 1405

Greenwood, R. C., Barrat, J.-A., Miller, M. F., et al. 2018, Science advances, 4, eaao5928

Grimm, S. L. & Stadel, J. G. 2014, The Astrophysical Journal, 796, 23

Halliday, A. N. 2013, Geochimica et Cosmochimica Acta, 105, 146

Hallis, L. 2017, Philosophical Transactions of the Royal Society A: Mathematical, Physical and Engineering Sciences, 375, 20150390

Hamano, K., Abe, Y., & Genda, H. 2013, Nature, 497, 607

Hansen, B. M. 2009, The Astrophysical Journal, 703, 1131

Hayashi, C. 1981, Progress of Theoretical Physics Supplement, 70, 35

Humayun, M., Nemchin, A., Zanda, B., et al. 2013, Nature, 503, 513

Hunten, D. M., Pepin, R. O., & Walker, J. C. 1987, Icarus, 69, 532

Hutson, M. & Ruzicka, A. 2000, Meteoritics & Planetary Science, 35, 601

Hyodo, R. & Genda, H. 2018, The Astrophysical Journal Letters, 856, L36

Hyodo, R., Genda, H., Charnoz, S., & Rosenblatt, P. 2017, The Astrophysical Journal, 845, 125

Ida, S. & Guillot, T. 2016, Astronomy & Astrophysics, 596, L3

Ida, S., Guillot, T., & Morbidelli, A. 2016, Astronomy & Astrophysics, 591, A72

Izidoro, A., Haghighipour, N., Winter, O., & Tsuchida, M. 2014, The Astrophysical Journal, 782, 31

Jacobson, S. A. & Morbidelli, A. 2014, Phil. Trans. R. Soc. A, 372, 20130174

Javoy, M., Kaminski, E., Guyot, F., et al. 2010, Earth and Planetary Science Letters, 293, 259

Johansen, A., Oishi, J. S., Mac Low, M.-M., et al. 2007, Nature, 448, 1022

Johnstone, C., Güdel, M., Brott, I., & Lüftinger, T. 2015, Astronomy & Astrophysics, 577, A28

Kaib, N. A. & Cowan, N. B. 2015, Icarus, 252, 161

Kasting, J. F. 1991, icarus, 94, 1

Keene, B. 1993, International Materials Reviews, 38, 157

Kerridge, J. F. 1985, Geochimica et Cosmochimica Acta, 49, 1707

Kimura, K., Lewis, R. S., & Anders, E. 1974, Geochimica et Cosmochimica Acta, 38, 683

Kleine, T., Touboul, M., Bourdon, B., et al. 2009, Geochimica et Cosmochimica Acta, 73, 5150

Kokubo, E. & Genda, H. 2010, The Astrophysical Journal Letters, 714, L21

Kokubo, E. & Ida, S. 1998, Icarus, 131, 171

Kruijer, T. S., Kleine, T., Borg, L. E., et al. 2017, Earth and Planetary Science Letters, 474, 345

Kruijer, T. S., Kleine, T., Fischer-Gödde, M., & Sprung, P. 2015, Nature, 520, 534

Lammer, H., Kulikov, Y. N., & Lichtenegger, H. I. 2006, Space Science Reviews, 122, 189

Lebrun, T., Massol, H., Chassefière, E., et al. 2013, Journal of Geophysical Research: Planets, 118, 1155

Levison, H. F., Kretke, K. A., & Duncan, M. J. 2015, Nature, 524, 322

Lin, D. & Papaloizou, J. 1986, The Astrophysical Journal, 309, 846

Lodders, K. 2000, in From Dust to Terrestrial Planets (Springer), 341–354

Lodders, K. & Fegley Jr, B. 1997, Icarus, 126, 373

Mann, U., Frost, D. J., Rubie, D. C., Becker, H., & Audétat, A. 2012, Geochimica et Cosmochimica Acta, 84, 593

Marchi, S., Canup, R., & Walker, R. 2018, Nature Geoscience, 11, 77

Marinova, M. M., Aharonson, O., & Asphaug, E. 2008, Nature, 453, 1216

Mason, E. & Marrero, T. 1970, in Advances in Atomic and Molecular Physics, Vol. 6 (Elsevier), 155–232

Masset, F. & Snellgrove, M. 2001, Monthly Notices of the Royal Astronomical Society, 320, L55

Matsumura, S., Brasser, R., & Ida, S. 2016, The Astrophysical Journal, 818, 15

McNaughton, N., Borthwick, J., Fallick, A., & Pillinger, C. 1981, Nature, 294, 639

Melosh, H. & Vickery, A. 1989, Nature, 338, 487

Melosh, H. & Vickery, A. 1991, Nature, 350, 494

Melosh, H. J. 1989, Research supported by NASA. New York, Oxford University Press (Oxford Monographs on Geology and Geophysics, No. 11), 1989, 253 p., 11

Michalski, J. R., Onstott, T. C., Mojzsis, S. J., et al. 2018, Nature Geoscience, 11, 21

Miller, S. L. et al. 1953, Science, 117, 528

Mittlefehldt, D. W., Clayton, R. N., Drake, M. J., & Righter, K. 2008, Reviews in Mineralogy and Geochemistry, 68, 399

Mojzsis, S. J., Brasser, R., Kelly, N. M., Abramov, O., & Werner, S. C. 2019, The Astrophysical Journal, in press

Monaghan, J. J. 1992, Annual review of astronomy and astrophysics, 30, 543

Monaghan, J. J. & Lattanzio, J. C. 1985, Astronomy and astrophysics, 149, 135

Morbidelli, A., Bitsch, B., Crida, A., et al. 2016, Icarus, 267, 368

Morbidelli, A., Brasser, R., Gomes, R., Levison, H. F., & Tsiganis, K. 2010, The Astronomical Journal, 140, 1391

Morbidelli, A., Levison, H. F., Tsiganis, K., & Gomes, R. 2005, Nature, 435, 462

Morbidelli, A., Lunine, J. I., O'Brien, D. P., Raymond, S. N., & Walsh, K. J. 2012, Annual Review of Earth and Planetary Sciences, 40, 251

Moriarty, J., Madhusudhan, N., & Fischer, D. 2014, The Astrophysical Journal, 787, 81

Morishima, R., Stadel, J., & Moore, B. 2010, Icarus, 207, 517

Murthy, V. R. 1991, Science, 253, 303

Nemchin, A., Humayun, M., Whitehouse, M., et al. 2014, Nature Geoscience, 7, 638

Nesvornỳ, D., Vokrouhlickỳ, D., Bottke, W. F., & Levison, H. F. 2018, Nature Astronomy, 2, 878

Neumann, W., Breuer, D., & Spohn, T. 2014, Earth and Planetary Science Letters, 395, 267

Nimmo, F., Hart, S., Korycansky, D., & Agnor, C. 2008, Nature, 453, 1220

O'Brien, D. P., Izidoro, A., Jacobson, S. A., Raymond, S. N., & Rubie, D. C. 2018, arXiv preprint arXiv:1801.05456

O'Brien, D. P., Morbidelli, A., & Levison, H. F. 2006, Icarus, 184, 39

Ogihara, M. & Ida, S. 2009, The Astrophysical Journal, 699, 824

O'Neill, H. S. C. 1991, Geochimica et Cosmochimica Acta, 55, 1159

Ouellette, N., Desch, S., & Hester, J. 2007, The Astrophysical Journal, 662, 1268

Pepin, R. O. 1997, Icarus, 126, 148

Pierrehumbert, R. & Gaidos, E. 2011, The Astrophysical Journal Letters, 734, L13

Pizzolato, N., Maggio, A., Micela, G., Sciortino, S., & Ventura, P. 2003, Astronomy & Astrophysics, 397, 147

Pujol, M., Marty, B., & Burgess, R. 2011, Earth and Planetary Science Letters, 308, 298

Qin, L. & Carlson, R. W. 2016, Geochemical Journal, 50, 43

Qin, L., Nittler, L. R., Alexander, C. O., et al. 2011, Geochimica et Cosmochimica Acta, 75, 629

Quintana, E. V., Barclay, T., Borucki, W. J., Rowe, J. F., & Chambers, J. E. 2016, The Astrophysical Journal, 821, 126

Ramirez, R. M. 2017, Icarus, 297, 71

Ramirez, R. M. & Craddock, R. A. 2018, Nature Geoscience, 11, 230

Ramirez, R. M. & Kaltenegger, L. 2017, The Astrophysical Journal Letters, 837, L4

Raymond, S. N. & Izidoro, A. 2017, Science advances, 3, e1701138

Raymond, S. N., OBrien, D. P., Morbidelli, A., & Kaib, N. A. 2009, Icarus, 203, 644

Raymond, S. N., Quinn, T., & Lunine, J. I. 2004, Icarus, 168, 1

Regelous, M., Elliott, T., & Coath, C. D. 2008, Earth and Planetary Science Letters, 272, 330

Render, J., Fischer-Gödde, M., Burkhardt, C., & Kleine, T. 2017, Geochem Perspect Lett, 3, 170

Ribas, I., De Mello, G. P., Ferreira, L., et al. 2010, The Astrophysical Journal, 714, 384

Ribas, I., Guinan, E. F., Güdel, M., & Audard, M. 2005, The Astrophysical Journal, 622, 680

Righter, K. & Chabot, N. L. 2011, Meteoritics & Planetary Science, 46, 157

Righter, K., Danielson, L., Pando, K., et al. 2015, Meteoritics & Planetary Science, 50, 604

Robert, F. & Epstein, S. 1982, Geochimica et Cosmochimica Acta, 46, 81

Robert, F., Merlivat, L., & Javoy, M. 1977, Meteoritics, 12, 349

Robert, F., Merlivat, L., & Javoy, M. 1979, Nature, 282, 785

Rosenblatt, P. & Charnoz, S. 2012, Icarus, 221, 806

Rosenblatt, P., Charnoz, S., Dunseath, K. M., et al. 2016, Nature Geoscience, 9, 581

Rubie, D. C., Jacobson, S. A., Morbidelli, A., et al. 2015, Icarus, 248, 89

Rubie, D. C., Laurenz, V., Jacobson, S. A., et al. 2016, Science, 353, 1141

Rubin, A. E., Warren, P. H., Greenwood, J. P., et al. 2000, Geology, 28, 1011

Sanloup, C., Jambon, A., & Gillet, P. 1999, Physics of the Earth and Planetary Interiors, 112, 43

Schaeffer, O. & Husain, L. 1974, in Lunar and Planetary Science Conference Proceedings, Vol. 5, 1541–1555

Schlichting, H. E., Sari, R., & Yalinewich, A. 2015, Icarus, 247, 81

Sekiya, M., Nakazawa, K., & Hayashi, C. 1980, Progress of Theoretical Physics, 64, 1968

Shearer, C. & Borg, L. 2006, Chemie der Erde-Geochemistry, 66, 163

Shoemaker, E. M. 1962, Physics and Astronomy of the Moon, 283

Siess, L., Dufour, E., & Forestini, M. 2000, Astronomy and Astrophysics, 358, 593

Sleep, N. H., Zahnle, K. J., Kasting, J. F., & Morowitz, H. J. 1989, Nature, 342, 139

Soderblom, D. R., Stauffer, J. R., MacGregor, K. B., & Jones, B. F. 1993, The Astrophysical Journal, 409, 624

Spudis, P. D., Wilhelms, D. E., & Robinson, M. S. 2011, Journal of Geophysical Research: Planets, 116

Stevenson, D. 1981, Science, 214, 611

Stolper, E., Baker, M., Newcombe, M., et al. 2013, science, 341, 1239463

Tait, K. T. & Day, J. M. 2018, Earth and Planetary Science Letters, 494, 99

Tang, H. & Dauphas, N. 2014, Earth and Planetary Science Letters, 390, 264

Taylor, G. J. 2013, Chemie der Erde-Geochemistry, 73, 401

Tera, F., Papanastassiou, D., & Wasserburg, G. 1974, Earth and Planetary Science Letters, 22, 1

Touboul, M., Puchtel, I. S., & Walker, R. J. 2015, Nature, 520, 530

Treiman, A. H., Gleason, J. D., & Bogard, D. D. 2000, Planetary and Space Science, 48, 1213

Trinquier, A., Birck, J.-L., & Allegre, C. J. 2007, The Astrophysical Journal, 655, 1179

Trinquier, A., Elliott, T., Ulfbeck, D., et al. 2009, Science, 324, 374

Tsiganis, K., Gomes, R., Morbidelli, A., & Levison, H. 2005, Nature, 435, 459

Tu, L., Johnstone, C. P., Güdel, M., & Lammer, H. 2015, Astronomy & Astrophysics, 577, L3

Turner, G., Cadogan, P., & Yonge, C. 1973, Nature, 242, 513

Urey, H. C. 1952, Proceedings of the National Academy of Sciences, 38, 351

Vernazza, P., Brunetto, R., Binzel, R., et al. 2009, Icarus, 202, 477

Vernazza, P., Lamy, P., Groussin, O., et al. 2011, Icarus, 216, 650

Villanueva, G., Mumma, M., Novak, R., et al. 2015, Science, 348, 218

Walker, R. J. 2009, Chemie der Erde-Geochemistry, 69, 101

Walsh, K. J. & Levison, H. F. 2019, Icarus, 329, 88

Walsh, K. J., Morbidelli, A., Raymond, S. N., O'brien, D. P., & Mandell, A. M. 2011, Nature, 475, 206

Wänke, H. & Dreibus, G. 1988, Phil. Trans. R. Soc. Lond. A, 325, 545

Wänke, H. & Dreibus, G. 1994, Phil. Trans. R. Soc. Lond. A, 349, 285

Warren, P. H. 2011, Earth and Planetary Science Letters, 311, 93

Wasson, J. T. & Kallemeyn, G. W. 1988, Phil. Trans. R. Soc. Lond. A, 325, 535

Watson, A. J., Donahue, T. M., & Walker, J. C. 1981, Icarus, 48, 150

Weidenschilling, S. 1977, Astrophysics and Space Science, 51, 153

Werner, S. C. 2009, Icarus, 201, 44

Werner, S. C. 2014, Earth and Planetary Science Letters, 400, 54

White, W. B., Johnson, S. M., & Dantzig, G. B. 1958, The Journal of Chemical Physics, 28, 751

Wilhelms, D. E. & Squyres, S. W. 1984, Nature, 309, 138

Willbold, M., Mojzsis, S., Chen, H.-W., & Elliott, T. 2015, Earth and Planetary Science Letters, 419, 168

Wisdom, J. & Holman, M. 1991, The Astronomical Journal, 102, 1528

Wittmann, A., Korotev, R. L., Jolliff, B. L., et al. 2015, Meteoritics & Planetary Science, 50, 326

Woo, J. M. Y., Brasser, R., Matsumura, S., Mojzsis, S. J., & Ida, S. 2018, Astronomy & Astrophysics, 617, A17

Zahnle, K. 2015, in Lunar and Planetary Science Conference, Vol. 46, 1549

Zahnle, K. J., Gacesa, M., & Catling, D. C. 2019, Geochimica et Cosmochimica Acta, 244, 56

Zahnle, K. J. & Kasting, J. F. 1986, Icarus, 68, 462